THEORETICAL STUDIES OF GERMANIUM NANOWIRES AND SINGLE-WALLED CARBON NANOTUBES

SK MAHASIN ALAM

2012

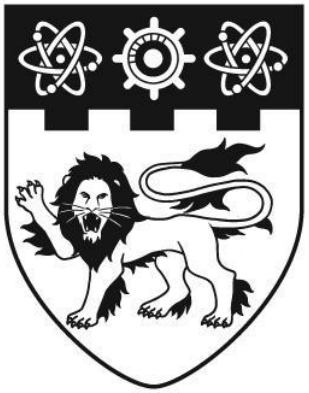

NANYANG TECHNOLOGICAL UNIVERSITY

THEORETICAL STUDIES OF GERMANIUM NANOWIRES AND SINGLE-WALLED CARBON NANOTUBES

SK MAHASIN ALAM

SCHOOL OF CHEMICAL AND BIOMEDICAL ENGINEERING

2012

THEORETICAL STUDIES OF GERMANIUM NANOWIRES AND SINGLE-WALLED CARBON NANOTUBES

SK MAHASIN ALAM

School of Chemical and Biomedical Engineering

A thesis submitted to the Nanyang Technological University in partial fulfillment of the requirement for the degree of

DOCTOR OF PHILOSOPHY

2012

Acknowledgements

I am highly indebted and like to express my gratitude to my supervisor Assistant Professor Lim Kok Hwa, School of Chemical and Biomedical Engineering, Nanyang Technological University, for giving me the opportunity to do my doctoral thesis in his research group. I am grateful for his constant active guidance, stimulating suggestions and endless encouragement throughout the course of my research.

I gratefully thank Dr. Xi Hong-Wei for his kind and encouraging interactive scientific discussions. I am grateful to Dr. Ng Man-Fai, Institute of High Performance Computing, for his helps, encouragements and interactive scientific discussions.

I thank the past and present research group members: Dr. Da Haixia, Tan Shiow Jin, Li Xiang and Sultana Bedoura for their support. I also thank my friends Dr. Shovanlal Gayen, Parthasarathi Panda, Anindya Basu, Souvik Basak and those not mentioned here for their moral support and encouragements.

I am grateful to School of Chemical and Biomedical Engineering, Nanyang Technological University and Institute of High Performance Computing for providing computational facilities. I am grateful too, to Nanyang Technological University for providing all the facilities and scholarship support.

A heartfelt gratitude goes to my parents, in-laws, nieces and nephews, brothers, sisters and other family members and relatives for their omnipresent love, trust and enthusiastic supports.

A very special thank to my wife Rebecca for her unconditional love, moral support, continuous encouragement, patience and understanding.

Abstract

In this thesis we study the electronic properties of OH passivated germanium nanowires (OH-GeNWs) using density functional theory (DFT) calculations to investigate the cause of experimentally observed electrical hysteresis in GeNWs. We reveal that water molecule is initially physisorbed on the GeNW surface which is a reversible adsorption and over time, water molecule would dissociate into OH· and H· radicals leading to irreversible adsorption and formation of OH-GeNWs. In addition, we also show that the amount of water adsorbed is a main factor that affects stability and electronic properties of GeNWs. Based on our study, we attribute the causes of electrical hysteresis observed in GeNWs to (a) different amount of water being adsorbed, (b) alignment of the OH groups on the surface of GeNWs; and (c) presence of trap state defects on the surface of the OH-GeNWs. Surface dangling bond (SDB) defect induced electronic and magnetic properties of GeNWs are also investigated using DFT method. We show that single SDB defected GeNWs remain semiconducting as its non-defected form while double or multiple SDB defects result either semiconducting or metallic, depending on the defects' locations on the surface. More importantly, we show that the electronic properties of surface defected GeNWs can also be fine-tuned by applying tensile and compressive strains. Upon the right loading, the surface defected GeNWs become half-metallic. In addition, surface defected GeNWs can be classify into: (1) GeNWs with zero magnetic moment are either metallic or semiconducting; (2) GeNWs with net magnetic moments equal to the number of SDBs are semiconducting with distinct spin-up and spin-down configurations; and (3) GeNWs with net magnetic moments significantly lower than the number of SDBs. We also found that defected GeNWs that fall under (3) are potentially half-metallic. Our results predict that half-metallic GeNWs can be obtained via engineering of the surface defects and the structures without the presence of impurity dopants. The interactions of different molecules/ radicals with single-walled carbon nanotubes (SWNTs) using DFT method are also investigated to obtain the fundamental understanding about the binding properties of molecules/ radicals and the mechanisms of separation of SWNTs which are essential for various applications of CNTs.

Table of Contents

CHAPTER 1. Introduction 1

1.1 Nanowires 2

1.2 Carbon Nanotubes 8

CHAPTER 2. Theory and Computational Details 11

2.1 Computational Details 12

2.2 Models 13

2.3 Electronic Band Structures 13

2.4 Effective Mass of Electrons 16

2.5 Density-of-State (DOS) 16

CHAPTER 3. Literature Review 18

3.1 Ge Based Nanowires 18

3.1.1 Synthesis of Ge Based Nanowires 18

3.1.2 Major Challenges/Existing Problems for Ge Nanowire Applications 22

3.1.3 Properties and Applications of Ge and Ge/Si NWs 25

3.1.3.1 Potential Applications of Ge Based Nanowires 26

3.1.4 Theoretical Studies on Ge Based Nanowires 30

3.1.4.1 Growth Mechanism 31

3.1.4.2 Structural Properties 31

3.1.4.3 Electronic Properties 34

3.1.4.4 Optical Properties 40

3.1.4.5 Magnetic Properties 41

3.1.4.6 Mechanical Properties 42

3.1.4.7 Phonon Transport and Thermal Conductivity 42

3.2 Carbon Nanotubes 45

3.2.1 Properties and Applications of CNTs 45

3.2.2 Separation of CNTs 46

3.2.3 Theoretical Studies on CNTs 46
3.2.3.1 Interaction of CNTs with Molecules 46
3.2.3.2 Interaction of CNTs with Atoms/ Radicals 47
3.2.3.3 Interaction of CNTs with Metals 47
3.2.3.4 Interaction of Diazonium salts with CNTs 48

CHAPTER 4.Theoretical Studies on Germaallenes 50
4.1. Computational Methods 51
4.2. Optimized Geometries of Germaallenes and their Cyclic Isomers and the NPA Analysis 52
4.2.1 Monogermaallenes 52
4.2.2 Digermaallenes 57
4.2.3 Trigermaallene 59
4.3. Hyperconjugation of Stable Germaallenes 62
4.4. Stability of Germaallenes 67

CHAPTER 5. Theoretical Studies on Germanium Nanowires 69
5.1 Water Induced Electrical Hysteresis in Germanium Nanowire 70
5.1.1 Models 71
5.1.2 Formation Mechanism of OH-GeNWs 72
5.1.3 Stability and Electronic Properties of OH-GeNWs 75
5.1.4 Electrical Hysteresis in OH-GeNWs 80
5.2 Stress Induced Half-Metallicity in Surface Defected Germanium Nanowire 86
5.2.1 Single & Multiples SDB Defects 87
5.2.2 Defect Generation Energies 89
5.2.3 SDBs Induced Magnetic Dipole Moments 92
5.2.4 SDBs Dependent Spin Configurations 93
5.2.5 Strain Effects Induced Half-Metallic GeNWs 97

CHAPTER 6. Interactions of Molecules/ Radicals with Single-Walled Carbon Nanotubes 104
6.1 Anthraquinone Adsorption on SWNTs 105

6.2 Bromine Adsorption on SWNTs 108
CHAPTER 7. Summary 112
REFERENCES 120
APPENDIX A **Supplementary Materials for Theoretical Studies on Germaallenes** 146
APPENDIX B **Supplementary Materials for Theoretical Studies on Germanium Nanowires** 161
LIST OF PUBLICATIONS 172

List of Abbreviations

AAO	Anodized aluminium oxide
AFM	Anti-ferromagnetic
Al_2O_3	Aluminum oxide
Ar	Argon
atm	atmosphere
Au	Gold
B3LYP	Becke's three-parameter hybrid function with the non-local correlation of Lee-Yang-Parr
BTE	Boltzmann transport equation
BZ	Brillouin Zone
C_2H_4	Ethylene
CB	Conduction-band
CBM	Conduction-band minimum
CCSD	Coupled-cluster singles and doubles
cm	Centimeter
CNT	Carbon nanotube
CVD	Chemical vapor deposition
DFT	Density functional theory
DNA	Deoxyribonucleic acid
DOS	Density-of-State
DMTB	Density matrix tight-binding
DPG	Diphenylgermane
EAQ	Ethylanthraquinone
EDA	Energy decomposition analysis
eV	Electron volt
Fe	Iron
FET	Field effect transistor
FL	Fermi level
FM	Ferromagnetic
Ge	Germanium

GaN	Gallium nitride
GeH_4	Germane
GeNW	Germanium Nanowire
GeO_2	Germanium dioxide
GGA	Generalized-Gradient Approximation
H_2	Hydrogen
HCl	Hydrogen chloride
HF	Hartree-Fock
HfO_2	Hafnium oxide
H_2O	Water
HK	Hohenberg-Kohn
HOMO	Highest occupied molecular orbital
IBS	Ion beam synthesis
In	Indium
InP	Indium phosphide
kg	Kilogram
KS	Kohn-Sham
kΩ	Kilo ohm
LAPW	Linearized augmented plane wave
LCAO	Linear combination of atomic orbital
LDA	Local density Approximation
LED	Light-emitting diode
Li	Lithium
LUMO	Lowest unoccupied molecular orbital
mA.h/g	Mili ampere hour per gram
MD	Molecular dynamics
MgBr	Magnesium bromide
ml	Milliliter
KLMC	Monte-Carlo simulation
mmol	Mili molar
Mn	Manganese
MOSFET	Metal-oxide-semiconductor field effect transistor
MP2	Second-order Møller–Plesset perturbation theory

MPa	Mega Pascal
MTF	Mesoporous thin films
MWNT	Multi-walled carbon nanotube
μA/V	Micro ampere per voltage
N_2	Nitrogen
nA	Nano ampere
NBO	Natural bond orbital
NEMPROM	Nanoelectromechanical programmable read-only memory
nm	Nano meter
NPA	Natural Population analysis
NW	Nanowire
PES	Potential energy surface
PMMA	Polymethylmathacrylate
Pt	Platinum
RAM	random access memory
ROM	Read-only memory
Sb	Antimony
SDB	Surface dangling bond
SFLS	Supercritical fluid-liquid-solid
Si	Silicon
Si_3N_4	Silicon nitride
SiNW	Silicon nanowire
SiO_2	Silicon dioxide
SWNT	Single-walled carbon nanotube
T	Temperature
TCMn	Tricarbonyl-(methylcyclopentadienyl) manganese
TEG	Tetraethylgermane
TiO_2	Titanium dioxide
TS	Transition state
VASP	Vienna *ab initio* Simulation Package
VB	Valence-band
VBM	Valence-band maximum
VLS	Vapor-liquid-solid

VSS	Vapor-solid-solid
WBI	Wiberg Bond Index
ZrO_2	Zirconium oxide

Chapter 1

Introduction

The modern electronic devices such as computer that are used for data processing, cell phones for communication purposes, and photovoltaic devices in the pursuit of green technology are some of the many appliances that are now common place in our life. The basis of these modern electronic devices is the integration of transistors, diodes and capacitors into circuit boards or chips. More transistors placed onto a computer processing chip, more operations can be run on it and thus the faster the chip is. Moore's law has been the

cornerstone of what the modern electronic world have been trying to achieve. The law postulates that the number of transistors that can be placed on an integrated circuit will double approximately every two years. Currently, the fastest chip produced by Intel and IBM reaches to an astonishing two billion integrated transistors. To sustain the trend of scaling beyond current transistors, the most important materials being considered are semiconducting nanowires (*1-2*) and carbon nanotubes (*3-5*).

1.1 Nanowires

Nanowire (NW) is defined as one dimensional structure having diameter in nano-scale level (10^{-9} meters) (*6*). It is also known as "quantum wire", due to their large quantum mechanical effects at these scales. They can be broadly classified as metallic, semiconducting, insulating and molecular nanowires (see Table 1.1). Nanowires are explored as new building blocks in electronics, photonics, biochemical and chemical sensors. The unique properties of such nanoscaled materials are one-dimensional with small diameters, large surface-to-volume ratio and relatively smooth surfaces.

Table 1.1 Classifications of Nanowires (NWs) (*7-12*).

Types	**Examples**
Metallic NW	Ni, Co, Au NWs
Semiconducting NW	Si, Ge, InP, GaAs NWs
Insulating NW	SiO_2, TiO_2 NWs
Molecular NW	Organic NW – DNA
	Inorganic NWs – $Mo_6S_{9-x}I_x$, $Li_2Mo_6Se_6$

Amongst the diverse types of these materials, the semiconducting nanowires have attracted much interest to the researchers as potential materials for applications in high performance electronics, dye-sensitized solar cells, label-free ultra sensitive sensors (chemical/ biological), nanophotonics (light emitting diodes, lasers, active waveguides, integrated electro-optic modulators) etc. Semiconductor (*13*) is a material with conductivities between 10^{4} and 10^{-10} $(\Omega\ \mathrm{cm})^{-1}$. Some common semiconductors are listed in Table 1.2. Semiconductor devices such as microprocessor, random access memory (RAM), read-only memory (ROM), Gunn diode, laser diode, light-emitting diode (LED), photocell, solar cell, field effect transistor are essential parts of modern electronics (computers, mobile phones, digital audio players, etc.). The properties, such as conductivity and charge carrier mobility, of semiconductors can easily be manipulated by adding of impurities, applying an electric field, exposing to light, or even by pressure and heat, which make semiconductors very useful for their applications.

The current commercially used semiconductors are silicon and germanium. Germanium, group 14 element, was widely used as early semiconductor material. It possesses similar properties like silicon in many aspects. Both Ge and Si have diamond crystal structure with very close lattice parameters. So, their electronic properties can be varied by same sort of dopants (*14*). The energy band structure of both the Ge and Si can roughly described by sp^3-hybridization (*14*). Ge has direct (0.8 eV) (*15*) and indirect band gap (0.66 eV) (*15-16*). The band structures of bulk Ge are shown in Figure 1.1 (E_g is the indirect band gap, E_X is the energy separation in X point, $E_{\Gamma 1}$ and $E_{\Gamma 2}$ are direct band gap, ΔE is energy separation and E_{SO} is the spin-orbital splitting energy). Its direct band gap can be used in a variety of far-infrared astronomical experiments, both airborne and space based (*15*). Some key electrical properties e.g., Bohr radius, band gap, electrons and holes mobility of Ge and Si are listed in Table 1.3. (Bohr radius is the radius of smallest orbit for electron. The band gap is the energy

difference between maximum of valence band and minimum of conduction band. This indicates the energy required to free an outer shell electron to free-state. When the maximum of valence band is just above the minimum of conduction band, the energy gap is called direct band gap otherwise indirect band gap. The electron mobility can be defined as average velocity attained by the electron per applied unit electric field).

Table 1.2 Some common semiconductor materials (*15, 17-19*).

Materials	**Band gap (eV)**	**Electron effective mass**[a]	**Hole effective mass**[a]
Si	1.10	1.080 m_e	0.560 m_e
Ge	0.66	0.550 m_e	0.370 m_e
GaAs	1.43	0.067 m_e	0.450 m_e
ZnO	3.37	0.190 m_e	1.210 m_e
ZnSe	2.70	0.170 m_e	1.440 m_e

[a] m_e indicates the mass of a free electron (9.11×10^{-31} kg).

Semiconducting NWs display interesting electronic, optical, and mechanical properties due to quantization of the electronic states (*20*). They have been proposed as building blocks for wide range of electronic and optoelectronic devices, such as field effect transistors (FETs), *p-n* diodes, memory elements, logic gates, chemical sensors (*21*), biological sensors and photovoltaic (*22-23*). Silicon NWs (SiNWs) and germanium NWs (GeNWs) are promising candidates in nanoelectronics and nanophotonics. The purification difficulties and thermal sensitivity of Ge make it less useful than silicon, but at nanoscale level, Ge displays unique physical, electrical, thermal and optical properties (*15-16, 24*) as compared to silicon. Due to its unique properties at nano level, Ge gained renewed interest as

materials for potential applications in high-speed electronics, photonics, field effect transistors, nano-scale logic chip (*25*).

Table 1.3 Some key properties of bulk germanium and silicon (*15*).

Bulk material	Bohr radius (nm)	Band gap (eV)		Mobility ($cm^2/V\ s$)	
		Direct	Indirect	Electron	Hole
Germanium	24.3	0.80	0.66	3900.0	1900.0
Silicon	4.7	-	1.10	1500.0	450.0

The larger excitonic Bohr radius of Ge (24.3 nm) as compared to Si (4.7 nm) leads to more prominent quantum confinement effects in relatively larger structures which makes GeNWs a potentially useful material for extremely low-power, high speed quantum computing.

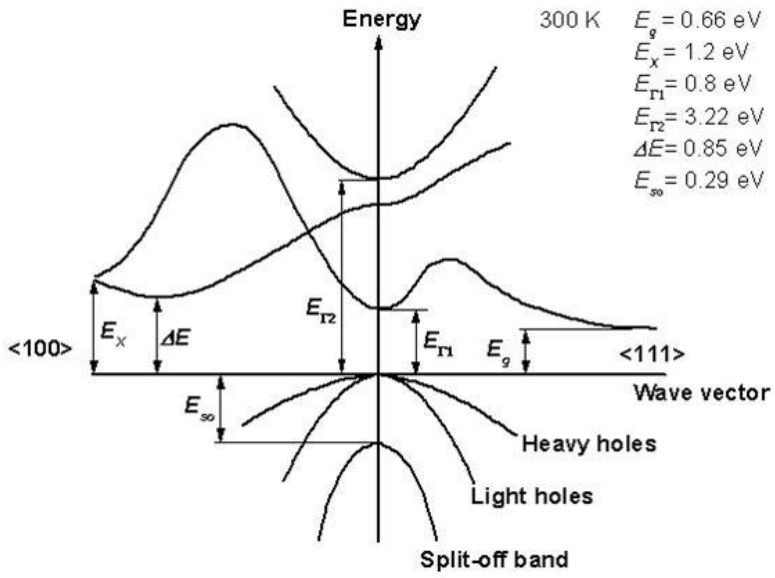

Figure 1.1 Band structure of bulk Ge, direct band gap of 0.8 eV (approx.) and indirect band gap of 0.66 eV (approx.). [Reprinted with permission from ref. (*15*). Copyright 2006, Springer]

GeNWs have been proposed for applying in spintronics as an alternative of carbon nanotubes (*26*), Li ion batteries anode as an alternative of graphite (*27*), photoresistors (*28*), photodetector in visible range (*29*) and memory devices (*30*). GeNWs can also be used for photonic signal detection such as ultra-fast integrated optical interconnects (*15*). At nanoscale Ge displays unique optical properties and holds promise for application in photonics.

Despite the wide range of applications of GeNWs, some major challenges mainly which affects the physical properties of GeNWs should be met. (a) First problem is the cost to synthesize a single crystal GeNWs is high since Ge is a naturally scarce element and mass production is lacking. (b) Second problem: GeNWs are susceptible to oxidation and corrosion when it is exposed to oxygen and water (*31*) and forms oxide (GeO_2) (*32-33*) on the surfaces which is unstable and soluble in H_2O. So, the interface between Ge and its oxide has high surface states. Hence there is an ardent need for efficient methods of mass production of Ge using robust chemical methods that will help in passivation of Ge surfaces to prevent its oxidation. (c) Third problem is that the majority of researchers have used gold (Au) (*23-24, 32, 34-35*) atom as catalyst for the synthesis of GeNWs while the Au atom remains integrated as a contaminant which is undesirable for electronic applications (*36*). Iron, nickel, and titanium were also used as catalysts for nanowire growth (*36*); since they are *back-end* materials in semiconductor processing, lead to device contamination. So, the non-contaminating catalyst schemes must be explored to facilitate the integration of GeNWs into applications. (d) Fourth problem is that the electrical properties of GeNW devices could be affected by various surface species including molecules adsorbed from environment.

Since the interface between Ge and GeO_2 have high surface state it will affect the performance of electronic devices (*37*) e.g., large hysteresis in current versus gate voltage curves in GeNWs (shown in Figure 1.2). Uncontrolled hysteresis in electronic devices is undesirable because it will make the operations highly unpredictable. Detailed understanding

of the surface chemistry is required to remove the hysteresis. Elimination of hysteresis is particularly important and challenging for GeNWs due to their well-known poor surface oxide properties. It was proposed that the observed hysteresis may be due to water molecules bound to GeO_2 on GeNWs, but the detailed mechanism is not fully understood (*38*). GeNWs also exhibit *p*-type field effect due to negative charge accumulation on surface. The surface state affects the electronic properties which are dominated in nanoscale level (*39*). The surface states in *p*- and *n*- types GeNWs cause opposite band bending with different doping (*40*).

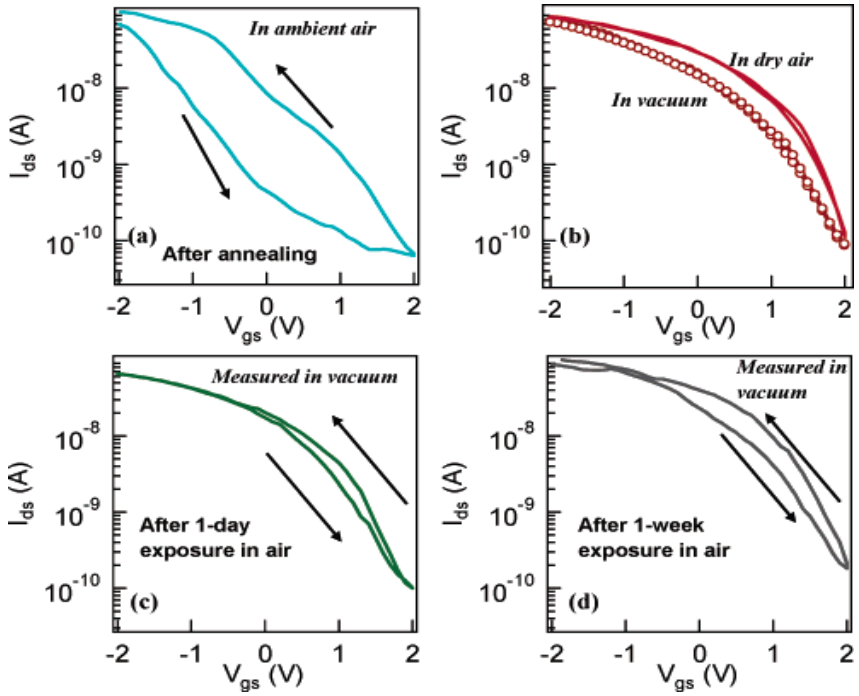

Figure 1.2 Hysteresis in current versus gate voltage curves in GeNWs after exposing in ambient and dry air. [Reprinted with permission from ref. (*41*). Copyright 2004, American Chemical Society]

Unfortunately surface chemistry of GeNWs is less explored and understood than that of Si. How different species on Ge surfaces affect the electrical properties of Ge is not yet clear. Rational strategies for developing tailored semiconducting devices would be greatly

facilitated by improved knowledge at the molecular level of how the properties of the nanowires changes. Calculated potential energy diagrams, band structures, surface density of states, work functions etc. provide information on the physical properties of the devices and allow a direct identification of the electronic properties of the materials. This motivated the current theoretical works on GeNWs. To study the electronic and magnetic properties of GeNWs, firstly we study the structures, bondings and electronic properties of germaallenes, building block of GeNWs. The knowledge of which can be used as the starting point to understand the bonding and electronic structures of GeNWs.

1.2 Carbon Nanotubes

Carbon nanotubes (CNTs) are cylindrical nanostructures made of rolling up of graphene sheets. CNTs are the strongest and stiffest materials discovered yet. The strength of CNTs is due to presence of the sp^2 bonds formed between carbon atoms. CNTs have unique electrical characteristic i.e., metallic and semiconducting depending on structures. CNTs have many structures which differ in lengths, diameters, chirality and number of layers. CNTs can be classified into two groups, single-walled carbon nanotubes (SWNTs) and multiple-walled carbon nanotubes (MWNTs) depending on the number of layers. The SWNTs are further classified in zigzag (n,n), armchair (n,0) and chiral (n,m) depending on the unit vector (n,m), where integers n and m denote the number of unit vectors along two directions in the honeycomb crystal lattice of graphene (see Figure 1.3). The unit vector (n,m) is called chiral vector. The chirality, which is defined by chiral vector, affects the conductance of nanotubes, its density, lattice structure and other properties. CNTs show metallic nature when the (n-m) is divisible by three, otherwise semiconducting. About one-third of as-synthesized SWNTs are metallic and about two-third are semiconducting.

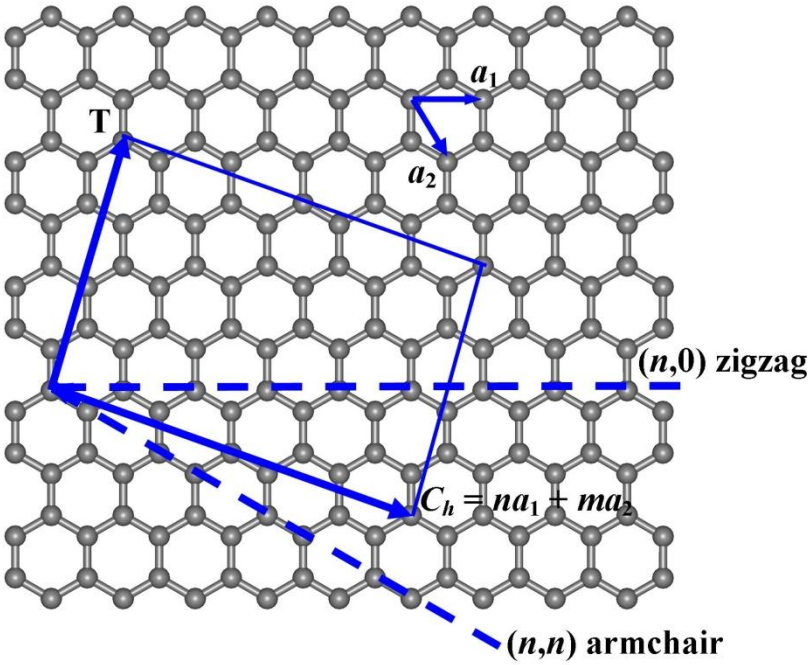

Figure 1.3 The (*n*,*m*) naming of SWNTs. T denotes the axis of tubes, $\boldsymbol{a_1}$ and $\boldsymbol{a_2}$ are the unit vector of graphene in real space. (www.wikipedia.com)

The CNTs can be synthesized by arc discharge (*42*), laser ablation (*43*), chemical vapour deposition (CVD) (*44*), pyrolysis (*45*) and electrochemical (*46-47*) methods. Iijima in 1991 first synthesized the CNTs by arc discharge method (*48*), but the synthesis of SWNTs (*49-50*) came in 1993. The SWNTs are attractive materials for use in FETs due to superior field-effect behaviour (*3-5*). Since, as-synthesized SWNTs contain a large amount of metallic tubes (about one-third), the presence of metallic tubes impair or destroy the switching behaviour of FET active channel. Thus, the removal or destruction of metallic tubes is necessary for the high performance of FETs. A numerous separation strategies have been taken to separate semiconducting CNTs from metallic CNTs which include the synthetic strategy of selective growth, electrophoretic separation, dielectrophoresis (*51-53*), density gradient ultracentrifugation (DGU) (*54-55*), chromatography (*56*), gel-based separation techniques, (*57*) surfactant extraction (*58-60*), selective aromatic extraction (*61-62*), amine extraction, (*56*) electrical breakdown of metallic nanotubes (*63-64*), etc. Functionalizations of

SWNTs using small aromatic molecules such as diazonium salts (*65*), pyrene, porphyrin and pentacene derivatives and flavin mononucleotide (*61, 66*) have been used for selective separation of SWNTs. The aromatic molecules can strongly binds with SWNTs via π-π interactions. However, most of the separation techniques are either expensive or do not produce SWNTs sample with sufficient semiconducting purity for applications in electronic devices. Thus, the theoretical studies on the interactions of molecules or radicals with SWNTs are necessary to obtain fundamental understanding about the differential binding properties of molecules/ radicals on SWNT and hence the mechanism of their separations.

The goals of the present work were –

(a) to study the structures, bonding and hyperconjugations of germaallene, building block of GeNWs.
(b) to understand the effect of adsorbed water molecules on electronic properties of GeNWs and to find the role of water in observed electrical hysteresis of GeNWs.
(c) to investigate the effect of surface defect on electronic and magnetic properties of GeNWs.
(d) to investigate the interactions of different molecules or radicals with various SWNTs.

Chapter 2

Theory and Computational Details

Ab initio electronic structure methods are computational chemistry methods based on quantum mechanics. The meaning of Latin word "*ab initio*" is "from the beginning". The *ab initio* calculations do not include any empirical or semi-empirical parameters other than a most basic description of the system. The most popular *ab initio* methods are HF (Hartree-Fock), MP2, (second order Møller–Plesset perturbation theory) (*67-68*), CCSD (coupled-

cluster theory including single and double excitations) (*69-72*) methods, etc. The density functional theory (DFT) (*73-74*) has been developed more recently and often considered to be *ab initio* methods. This method is originally derived from the theorem of Hohenderg and Kohn (*73*). It states that the ground-state molecular energy, wave function, and other molecular electronic properties of a molecule are uniquely determined by the ground-state electron probability density $\rho_0(x, y, z)$ (*75*). The ground-state electronic energy E_0 is a functional of ρ_0 and represents as $E_0 = E_0[\rho_0]$ (*76*). However, the HK theorem does not tell how to calculate E_0 from ρ_0 or how to find ρ_0 without first finding the wave function (*75*). The Kohn-Sham (KS) theory provides the practical solution for finding ρ_0 and for finding E_0 from ρ_0. The method is similar in structure with Hartree-Fock method. The electron density is expressed as a linear combination of basis functions. Then a determinant is formed from these functions, called Kohn-Sham orbitals (*77*). The electron density obtained from this determinant is used to compute the ground-state energy. In principle, KS theory allows one to solve the Schrodinger equation to obtain the exact ground-state energy. Unfortunately, the exact form of the exchange-correlation potential of KS theory is not known. Thus, the different approximations have been used e.g., local density approximation (LDA), generalized gradient approximation (GGA), hybrid functional, etc (*76*).

2.1 Computational Details

All the calculations were performed mainly by density functional theory (DFT) (*73-74*). The molecular structures, bonding, hyperconjugation and stability of germaallenes, building block of germanium nanowires (GeNWs), were studied by DFT (*78*) B3LYP (Becke's three-parameter hybrid function (*79*) with the non-local correlation of Lee-Yang-Parr (*80*)), MP2 (the second-order Møller–Plesset perturbation theory) (*67-68*) and CCSD (coupled cluster theory including single and double excitations) (*69-72*) methods with a

variety of basis sets. The calculations were carried out using Gaussian 03 suite of program (*81*). The NPA analysis and NBO hyperconjugation stabilization energies were obtained by the Natural Bond Orbital program (NBO 3.1) (*82*), which is implemented in Gaussian 03 (*81*). For periodic systems, e.g., GeNWs, carbon nanotubes (CNTs), all the calculations were performed within generalized gradient approximation Perdew-Burke-Eznerhof (GGA-PBE) (*83*) as implemented in Vienna *ab initio* simulation package (VASP) (*84-86*). We used projector augmented wave method (PAW) (*87-88*) to describe the interaction between the atomic cores and electrons. The energy cutoff of 400 eV was used for all the calculations. We mainly used 1x1x10 Monkhorst-Pack *k*-point (*89*) for our studies on GeNWs. For bulk calculations we used 11x11x11 Monkhorst-Pack *k*-point. For adsorption study on ⟨100⟩ GeO_2 surface and on SWNTs we used 2×2×1 and 1x1x1 Monkhorst-Pack *k*-point, respectively.

2.2 Models

The GeNWs and GeO_2 surface models used for our studies were created by cleaving the bulk Ge and GeO_2 along different growth orientation and with different size. To reduce the computational time required for optimization of GeNWs and GeO_2 surface, we first optimized the structures of bulk Ge and GeO_2. Then we constructed the GeNWs and GeO_2 surface models from optimized bulk models. For interaction study of SWNTs with molecules/ radicals, we used the periodic models of SWNTs. The details descriptions of GeNWs, GeO_2 surface models and SWNTs used for our studies were mentioned in the individual chapters.

2.3 Electronic Band Structures

The energy band and band gap are the main concepts of semiconductor physics. The materials are classified into metal, semiconductor and insulator based on their band structures

(*90*). In a solid, large numbers of bands are present. In a metal the band is partly filled and partly empty (*90*). The almost fully occupied band is called valence band (VB) and the almost unoccupied band is called conduction band (CB) (*90*) and the energy gap between VB and CB is called the band gap. The band structures of metal, semiconductor and insulator are illustrated in Figure 2.1. In a metal the two bands are overlapped (see Figure 2.1). The semiconductor and insulator are the material having the band gap. The difference between an insulator and semiconductor is that the band gap is larger in an insulator.

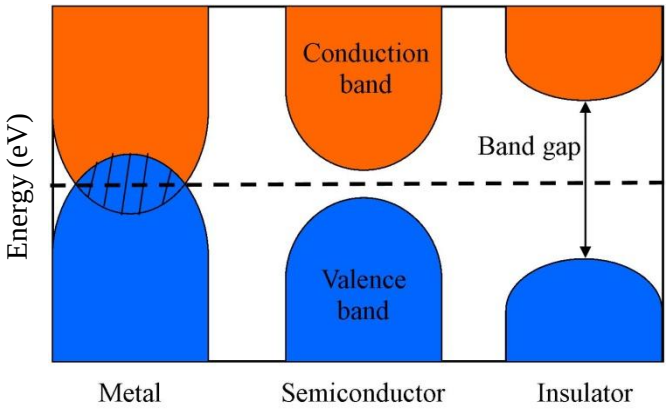

Figure 2.1 Simplified diagrams of band structures of metal, semiconductor and insulator. The dashed line is the Fermi level.

Band structure is the plot of electron orbitals' energies for each point in *k*-space, called the Brillouin zone (*77*). The *k*-space describes the bonding nature of orbitals (*77*). In a 3D crystal, *k*-space has three dimensions (k_x, k_y, k_z). The point where $k = 0$ is designated as Γ; $k = \pi/a$ is designated as *M*; $k = 0$ in some directions and $k = \pi/a$ in others is designated as *X*, *Y*, *K* and *A* depending on the symmetry of crystal (*77*). The typical band structure plot maps the orbital energies along the path between these points, called Spaghetti plot (*77*). The band structures of ⟨100⟩ and ⟨110⟩ GeNWs are shown in Figure 2.2.

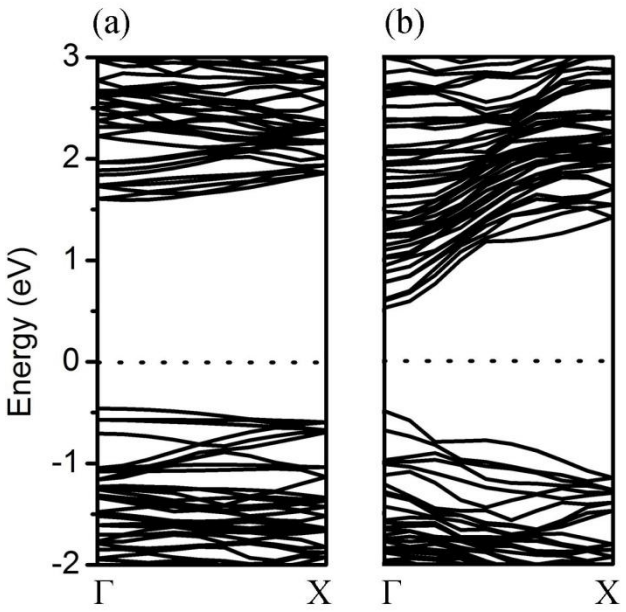

Figure 2.2 The band structures of hydrogen passivated GeNWs along (a) ⟨100⟩ and (b) ⟨110⟩ directions. The below bands are valence bands and upper bands are conduction bands. The dotted line is Fermi level and set to zero.

The computational methods which yield orbital energies can be used to calculate electronic band structures. In recent years the tendency to use *ab initio* or DFT methods are increasing. The *ab initio* methods require a set of basis functions, the choice of which is somewhat different from molecular calculations (*77*). The problem in large basis sets with diffuse functions is that it can contain contractions having a large overlap with their image in the adjacent unit cell, which prevents the self-consistent equations from being solved. To avoid this, small- to medium-size basis sets are used. The plane wave basis functions are popularly used because they reflect the infinite symmetry of a crystal (*77*). For calculation of band structures, unit cell lattice vectors and crystallographic angles must be provided (*77*). After computing the band structures it is very simple to calculate the band gap by inspection. But for some case it is not simple because the minimum and maximum energies of any given energy sometimes lie between different *k*-points. The highest occupied molecular orbital

(HOMO) level/band and lowest unoccupied molecular orbital (LUMO) level/band of a molecule are analogous to the valence band and conduction band of a semiconductor, respectively. So, the highest energy in the HOMO band plays a role analogous to high-energy edge of the valence band (VB). Similarly the bottom of LUMO band plays a role analogous to low-energy edge of conduction band (CB). Thus, some researcher used HOMO-LUMO energy separation to calculate the band gap of semiconductors. The electronic band structures of GeNWs were computed by using DFT GGA-PBE as implemented in VASP program (*84-86*). We also calculated the s- and p-occupancy of HOMO and LUMO by using DFT GGA-PBE as implemented in VASP program.

2.4 Effective Mass of Electrons

The effective mass of electrons is defined as (*91*) –

$$m^* = \left(\frac{h}{2\pi}\right)^2 / \left(\frac{d^2E}{dk^2}\right), \qquad (2.1)$$

where h is the Plank's constant, E is the energy dispersion near Γ point and k is the wave vector. The effective mass of electrons was calculated from the band structures. First the energy dispersion near Γ point is calculated using the wave vector from -0.1 to 0.1. Then, the curve of energy dispersion near the Γ point is fitted with second order polynomial

$$E = C_1K^2 + C_2k + C_3, \qquad (2.2)$$

where, C_1, C_2 and C_3 are the coefficients. Then the effective mass of electrons was calculated by taking the second derivative of equation (2.2) and putting the value in equation (2.1).

2.5 Density-of-State (DOS)

An important aspect of bands is the density-of-state (DOS) per unit energy as a function of energy (*92*). The DOS of a system describes how many orbitals are available at

any given energy level. It also gives the information about the nature of material, i.e., metal, semiconductor or insulator. The calculation of DOS depends on the nature of bands i.e., parabolic band, isotropic band, etc (*92*). One plot for DOS of ⟨100⟩ GeNW is shown in Figure 2.3. The dotted line indicates the Fermi level. The energy gap near the Fermi level, in which the DOS is zero, is the band gap of GeNW. The DOS of GeNWs was computed by DFT GGA-PBE as implemented in VASP program (*84-86*).

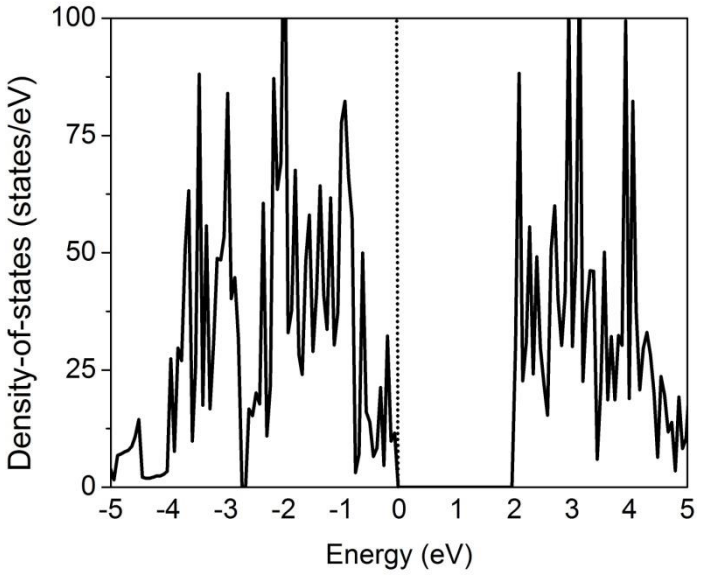

Figure 2.3 Density-of-state (DOS) of hydrogen passivated ⟨100⟩ GeNW. The dotted line is Fermi level and set to zero.

Chapter 3

Literature Review

In this Chapter we briefly reviewed the reported works on synthesis, properties, applications and theoretical works on Ge based nanowires and carbon nanotubes.

3.1 Ge Based Nanowires

3.1.1 Synthesis of Ge Based Nanowires

For applications, NWs must be crystalline, defect free with diameter ranging from 10 nm to 100 nm and length must be much larger than the diameter (*32*). The low growth temperature helps in reducing growth defects, preventing the wires from outgassing or deformation and minimizing dopant diffusion where local doping is demanded and offers

direct integration of NWs into nano-chip fabrication. In 1993, LeGoues et al. first reported the fabrication of single crystalline Ge quantum wires by liquid-solution synthesis (*93*). After that a significant number of methods have been reported for the synthesis of Ge based NWs which include laser ablation (*6*), simple vapor transport (*24*), vapor-liquid-solid (VLS) growth (*32, 94-100*), chemical vapor deposition (CVD) method (*20, 95, 101-107*), supercritical fluid-liquid-solid (SFLS) synthesis (*21, 34, 108-109*), low temperature gas phase deposition (*110*), low temperature CVD method (*35, 40*), thermal decomposition (*36*), solution synthesis (*25*), templated synthesis (*111*), solution-liquid-solid (*112*), electroplating (*113*), etc. In the following section, some of the synthetic methods used for preparation of Ge based NWs and their characteristics obtained from these methods are discussed.

In 2000, P. Yang et al. (*24*) prepared GeNWs using simple vapor transport process by vapor-liquid-solid (VLS) crystal growth mechanism. In a quartz tube, metallic Ge and GeI_4 mixture was put in one end and Si substrate coated with gold was put in the other end and heated to 1000-1100°C in N_2 environment at 30 mTorr which produces the wires of several hundred micrometers long and 80 nm in diameter. The size of the wires can be controlled by controlling the thickness of Au (which act as catalyst) coat. To further reduce the size of the wires, the as-synthesized wires collected from Si substrate surface was put in an evacuated quartz tube and further heated for 0.5-1 h at 800 °C. The sizes of produced web like nanowires were reduced to 16 nm. This method offers to synthesize single crystalline GeNWs with high yield and high purity.

B. Schmidt et al. (*114*), 2001, used ion beam synthesis (IBS) method for controlled synthesis of buried nanostructures. The SiO_2 covered V-grooves (001) Si wafers were used as substrate. After implementation of Si wafers at room temperature with Ge^+ ions ($1x10^{17}$ Ge^+ cm^{-2} at 70 eV), subsequent annealing was carried out in N_2 atmosphere at 950 ^{0}C which led to formation of nanowires of 35 nm diameter.

A single-crystal GeNWs were synthesized by H. Dai et al. (*115*) using the chemical vapor deposition (CVD) of germane (GeH_4) at 275 ^{0}C with Au nanocrystals as seed particles. The reaction was carried out in a quartz-tube reactor at 275 ^{0}C under H_2 flow of 110 sccm (standard cubic centimeter) using silicon coated with gold as substrate. The GeNWs were grown on the substrate through the Au particle-seeded VLS mechanism (see Figure 3.1). The method is simple and the high quality nanowires can be synthesized at low temperatures.

Figure 3.1 Growth of GeNW on catalyst (black color) via VLS method. [Reproduced with permission from ref. (*116*). Copyright 2005 Wiley-VCH Verlag GmbH & Co. KGaA, Weinheim]

Synthesis of GeNWs seeded by organic monolayer-coated gold nanocrystals based on VLS whisker growth mechanism was reported by B. A. Korgel et al. (*32*). The reaction was carried out in a titanium reaction cell. Si (100) wafer was used as substrate in this case. The reactor was deoxygenated by cyclohexane and pressurized with cyclohexane and heated to desired temperature. After that a stock solution of alkenethiol-coated Au nanocrystals in germanium precursors [tetraethylgermane (TEG) or diphenylgermane (DPG)] was injected to the reactor through sample loop into the supercritical cyclohexane in the hot reactor. The average diameter of the produced nanowires is 87 nm for TEG and 17 nm for DPG. The quality of GeNWs obtained from DPG was found to be superior as compared to TEG. This may be due to faster decomposition of DPG. The optimum growth temperature range is 350 to 400 ^{0}C. Unfortunately these GeNWs get oxidized significantly upon atmospheric exposure.

In 2003, B.A. Korgel et al. (*34*) also reported the synthesis of GeNWs seeded by colloidal metal nanocrystals. In this method, the wire was crystallized in the presence of a

metallic seed particle. A solution of alkanethiol passivated Au nanocrystals and germanium precursor (tetraethylgermane or diphenylgermane) was injected in a titanium reactor, pre-heated and pre-pressurized with supercritical hexane (at 375 ^{0}C and 20 Mpa). The solubility of precursor and high particle concentration permit the synthesis of large quantities of single-crystal nanowires having diameters ranging from 5 to 30 nm. This method yields bulk quantities of high quality nanowires.

S.M. Han et al. (*25*), 2006 used a simple solution synthesis method for preparation of GeNWs at lower temperature (285-315 ^{0}C) and pressure (1 atm) under Ar without use of any potentially contaminating seed materials. Ge precursor ($Ge(OC_6H_3(C(CH_3)_3)$-2,6)$_2$ dissolved in oleylamine was heated at 285-315 ^{0}C in a three-neck flash containing non-coordinating solvent 1-octadecene (11.5 ml, 17.0 mmol). The synthesized GeNWs were precipitated from chloroform by the addition of excess acetone and re-diluted with a variety of solvents, including $CHCl_3$, toluene, and hexane. The method is simple. No catalyst is required for the growth of GeNWs. As Ge^{2+} has lower reduction potential than Ge^{4+}, less energy is required to reduce the precursor to Ge. May be due to this reason, the method offers lower temperature growth of GeNWs.

GeNWs were synthesized by electrochemical etching of single crystalline *n*-type Ge in HCl-containing aqueous electrolyte in an electrochemical double cell with a four-electrode configuration by J. Carstensen et al. (*117*) in 2006. Prepared GeNWs were several hundred micrometers in length and roughly 50 to 500 nm in diameters. The method is easy and cheap compared to other methods but is a very slow process.

The synthesis of GeNWs by VSS growth mechanism was also reported by L. J. Lauhon et al. (*118*) in 2007. Mn deposited Si_3N_4 was used as the target substrate for nanowire growth. In a reactor Mn was deposited on Si_3N_4 by pyrolysis of tricarbonyl-(methylcyclopentadienyl) manganese (TCMn) at 350 ^{0}C and 100 Torr. Immediately after Mn

deposition, GeNW synthesis was initiated at 350 °C by introducing 0.125 sccm GeH_4 along with 25 sccm each of N_2 and H_2 at a total pressure of 25 Torr which yielded the nanowires having the diameters of 10-30 nm.

3.1.2 Major Challenges/Existing Problems for GeNW Applications

The major problems in GeNWs are (a) manufacturing cost, (b) surface oxidation, (c) catalyst contaminations and (d) electrical properties affected by different surface species adsorbed from the environment. The causes of different problems in GeNWs are mentioned in *Chapter 1*. In this section we discussed the different measures taken to overcome these challenges.

To overcome the oxidation difficulties of GeNWs, C. C. Tang et al. (*119*), 2005, reported a novel method to synthesize single-crystalline GeNWs with carbon coating. The reaction was performed in a quartz tube in argon atmosphere. A mixture of GeO_2 powder and Fe/Al_2O_3 (used as catalyst) with a weight ratio of 5:1 was heated in the reactor. At 750 ^{0}C argon was replaced by the flow of mixed gas of C_2H_4 (160 sccm) and NH_3 (80 sccm). This method yields the single-crystalline GeNWs having diameter distributions ranging from 15 to 50 nm and a length up to tens of micrometers with partial amorphous carbon covering. This method may open a new possibility for preparing the GeNWs for future applications. The GeNWs in protective C-shell also helps to prevent surface oxidation (*22*).

The surface passivations with different chemical species like alkene, alkyne and diene species, alkanethiols/ Grignard reaction, etc (*31*), (*33*) were mostly studied by different research group. The GeNWs were prepared from organogermane precursor, DPG by a gold (Au) nanocrystal-seeded process in supercritical Hexane. The prepared GeNWs were immersed in aq. 5% HCl or 5% HF for 5 min to terminate the surface with chloride or hydride, respectively. Then the surface was passivated by organic monolayer by exposing the

chloride or hydride-terminated GeNWs to alkene, alkyne, or diene species at elevated temperature in the supercritical fluid reactor. The thiol passivation was achieved by injecting the 1-octanethiol at 80 °C. It was found that the chloride or hydride-terminated GeNWs were very sensitive to oxidation. The alkene, alkyne, or diene passivated NWs were chemically robust and stable (*31*). However, the stable chemical passivation was also achieved with chloride (*120*).

H. Dai et al. (*33*), 2005, reported a modified CVD method to synthesize the oxidation resistant GeNWs. First, GeNWs were synthesized by CVD method and functionalized by alkanethiols/ Grignard reaction. For both the thiol and Grignard reactions, GeNWs were first treated with diluted HF or HCl to remove native oxides and terminate the surfaces with -H (for alkanethiol reactions) or -Cl (for Grignard reactions) and then functionalized by alkanethiols/ Grignard reactions (see scheme 3.1).

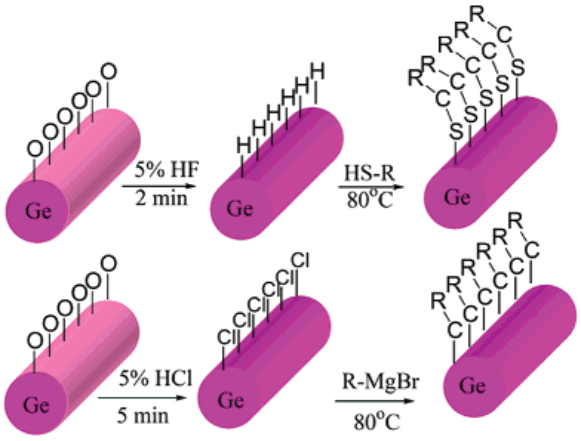

Scheme 3.1 GeNW (in pink color) functionalization steps using alkenethiols and Grignard reactions. [Reprinted with permission from ref. (*33*). Copyright 2004, American Chemical Society]

From the experiment it was found that the most stable passivation of GeNWs is achieved with C_{12} alkanethiol. The surface functionalized GeNWs exhibit high solubility in organic solvents and can readily be assembled into close-packed Langmuir-Blodgett films

potentially useful for future high performance electronic devices. Theoretical studies of effects of these functional groups on electronic structures will help to design proper passivation scheme to prevent the oxidation difficulty of GeNWs.

The other method to prevent the oxidation of GeNWs is by synthesizing Ge/Si NWs where the Si layer helps to prevent the oxidation of Ge. Ge/Si NW is a core-shell NW, in which the core part is made of Ge and shell part is made of Si and in Si/Ge NW the core part is Si and shell part is Ge. One structure of Si/Ge NW is shown in Figure 3.2.

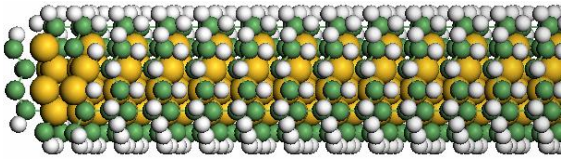

Figure 3.2 Si/Ge core-shell NW, central yellow colored part is Si and green colored shell part is Ge.

Si/Ge NWs are interesting heterostructures to study the heteroepitaxy and strain relaxation in NWs and NWs based devices. The Si/Ge NWs were mainly synthesized by CVD method via VLS growth mechanism (*94, 98, 121*). The Ge/Si core-shell NWs were also synthesized. The confinement potential in Ge/Si core-shell NWs is greater for holes as compared to Si\Ge core-shell NWs. In Ge/Si core-shell NWs, Si shell helps to prevent the oxidation difficulties of Ge because SiO_2 is more stable than GeO_2. FETs fabricated using Ge/Si core-shell NWs as channels have demonstrated better performance than SiNWs and GeNWs (*122*). Lew et al. (*94, 98*) in 2006, fabricated the Si/Ge NWs using commercial anodic alumina membranes. The membrane pores were initially loaded with Ag followed by Au. Then the Ag was removed by the treatment of HNO_3. The membrane was cleaned and dried. VLS growth was carried out by flowing SiH_4 and GeH_4 at temperature range of 275 °C to 500 °C which produced the Si/Ge NWs. The composition of Si and Ge depends on temperature and ratio of GeH_4 to (GeH_4 + SiH_4).

The majority of researchers have used gold (Au) (*23-24*, *32*, *34-35*), iron, nickel, and titanium (*36*) atoms as catalyst for the synthesis of GeNWs. But they remain integrated as a contaminant which is undesirable for electronic applications (*36*). The possible alternative catalysts are indium (In) and antimony (Sb) (*100*), which are the *front-end* materials and commonly used for channel or shallow junction doping of complementary metal-oxide semiconductor field effect transistor (*123*). M. Meyyappan et al. (*100*) reported a synthetic method for formation of GeNWs on insulator (SiO_2) using both In and Sb as catalysts. Si wafer (either Si 100 wafer or 111wafer coated with SiO_2) was used as the target substrate for nanowire growth. A mixture of hydrogen and argon was used as carrier gas. The catalyst (In or Sb films of varying thickness 100–300 Å) deposited on Si substrate was placed in a two-stage tube furnace system at low temperature zone while Ge powder (99.99%, Alfa Aesar) was placed at the center of the high temperature zone of the tube furnace. For nanowires growth based on In and Sb, the samples were heated to 400–500 and 600–700 °C, respectively. The catalysts used here (In and Sb), introduced no contamination in device processing and integration. Also at the nanowire growth conditions, the amount of catalysts (In and Sb) in nanowires could not reach the dopant concentrations. The prepared nanowires are single crystal with a defect-free diamond cubic lattice structure having diameters of around 10-15 nm. GeNWs, synthesized by this method, offer a viable nanomaterial platform for high-performance and low-power electronics. Due to use of non contaminating metal catalysts and nanowires growth on insulator, this method facilitates direct integration of nanowires' components into future nanoelectronic chips.

3.1.3 Properties and Applications of Ge and Ge/Si NWs

The first successful fabrication of high-performance GeNW FETs was reported by Wang et al. in 2003. The device was made up of *p*-doped GeNWs synthesized by low-

temperature chemical vapor deposition method with peak hole mobilities of 600 cm^2/V s and high ON/OFF current ratios. Lieber et al. in 2004 fabricated the similar devices with *p*- and *n*-type doped GeNWs. Gu et al. and Korgel et al. also attempted to synthesized GeNW FETs but observed low performance of the device which was argued to unintentional doping. We discussed the properties of GeNWs and their potential applications below.

3.1.3.1 Potential Applications of Ge Based Nanowires

In this sub-section we discussed the properties based potential applications of GeNWs. The Mn-doped GeNWs displays ferromagnetism at room temperature and hold promise for application in spintronic devices (*124*). The observed ferromagnetic properties depend on Mn concentrations and reach a maximum at intermediate Mn concentrations. This property is masked with decreasing nanowire diameter due to appearance of an interfacial strain. It was also observed that the spin diffusion length in GeNWs is slightly larger than that in carbon nanotubes. So, GeNWs may be an interesting alternative to carbon nanotubes in spintronics (*125*).

The electrochemical properties of GeNWs were studied by galvanostatic cycling using GeNWs on Si substrate as working electrode and Li foil as counter electrode. The chemical cycling is stable for 20 cycles at the C/20 rate. The first charge and discharge capacity is 2967 and 1141 mA. h/ g, respectively (Coulombic efficiency 39%). A good cyclability was observed at C/5, C/2, C and 2 C rates. The capacity at 2C dropped to 600 mA. h/ g (shown in Figure 3.3) which is higher than graphite capacity (372 mA. h/g). Due to their high specific capacity and excellent cycling performance GeNWs can be potentially used for higher-capacity alternative for the existing graphite anode in Li ion batteries (*126*).

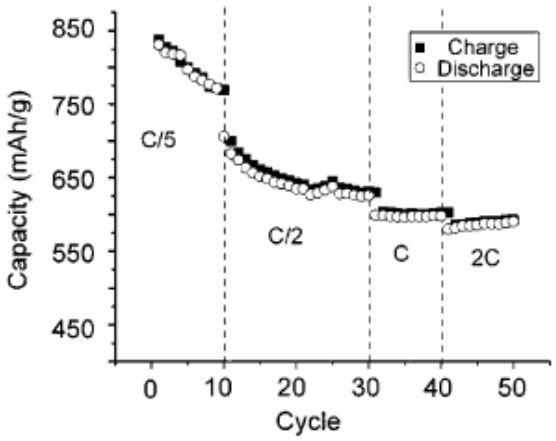

Figure 3.3 Cycling at different discharge rate with a charge rate of C/20. [Reprinted with permission from ref. (*126*). Copyright 2008, American Chemical Society]

The ultra-high density GeNWs were grown on Si and quartz substrates with packing densities of up to $2x10^{12}$ wires/ cm^2. The high density GeNWs display room temperature photoluminescence which depend on NWs diameter (*127*). The size dependent photoluminescence was also observed in GeNWs grown within the pores of mesoporous silica matrices (*128*). High density ordered arrays of GeNWs was synthesized within mesoporous thin films (MTF) (*129*) and anodized aluminium oxide (AAO) matrices (*16, 129-130*). The good conducting behavior of GeNWs-AAO indicates that the prepared NWs are continuous. For GeNW-MTF, a large region is non-conducting. So, better contacts are required for good electrical properties of GeNWs arrays. Laser induced increased in current is observed for GeNWs-AAO. The photocurrent in single GeNW with semitransparent Au electrode is in the range of 30 fA and 3 fA for 100 and 50 nm nanowires, respectively and increases linearly with bias voltage. This study offers a method for the use of Ge nanowire arrays as photoresistors (*16*). Ge is considered as near-IR photodetector material. But the optical response of GeFET especially in low intensity regime indicated that GeNW can be used as photodetector in visible range also (*131*). High density arrays and vertical GeNWs were prepared which have smooth surfaces, uniform diameters (*132*). These devices can be

used to produce vertical transistors, terapixel infrared photodetection systems, memory devices, Ge-based cryogenic power electronics for deep-space exploration, monolithic and Ge nanoresonators (*132*).

Nanoelectromechanical programmable read-only memory (NEMPROM) devices were constructed based on bistable Si and Ge NWs. The synthesized devices were robust. The nanowire remains in contact with electrode even after removal of electrostatic field. Nanowire could be switched ON and OFF multiple times, ~ 20–50, without noticeable deformation/ fracture. The devices have switching potentials as low as 1 V and high stability which make them ideal candidates for low-leakage electronic devices (*133*).

Doped GeNWs were used as channel material in the FETs (Back- and top-gated FETs (*35*, *40*), surround-gate FETs (*105*), vertically stacked layers of multi-NW FETs (*134*), impact ionization nanowire multiple-gate FETs (*135*), metal-oxide-semiconductor FETs (*136*), high performance Ge FinFETs (*137*), complementary FETs (*96*)). One example of FET using GeNWs as channel material is shown in Figure 3.4. All FETs have gate, source and drain terminal. In Figure 3.4 S, G and D indicate source, gate and drain, respectively. The GeNW passivated with nitride and silicon and coated with Al_2O_3 gate dielectric layer followed by Al layer is used as gate.

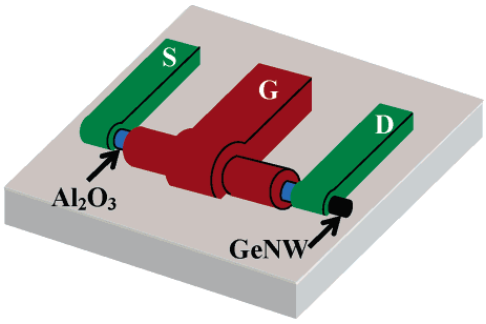

Figure 3.4 GeNW FET (Surround Gate FET), GeNW is in black, Al_2O_3 gate dielectric layer in blue and Al layer in red color. [Reprinted with permission from ref. (*105*). Copyright 2006, American Chemical Society]

For back gated FETs, observed hole mobility was higher than 600 cm^2/V s. The integration of high-k gate dielectric into nanowire-based transistors with HfO_2 gate insulators was achieved which will help to scale the channel length (*35, 40*). The device exhibits high I_{ON}/I_{OFF} ratio of 10^3 (approx.) and low linear resistances of 500 kΩ (approx.) for the ON state (*40*). The complementary FETs fabricated from GeNWs consist of individual GeNW with Ti source and drain contacts and gated via the degenerately doped Si substrate through a 60 nm thick zirconium oxide (ZrO_2) dielectric layer. The FETs showed the I_{ON}/I_{OFF} ratio of 105 with sub-threshold slope of 240 mV at drain voltage of 1 V. The observed trans-conductance corresponding to an estimated field-effect mobility of ~ 115 cm^2/V s is 3.3 μA/V (*96*). Surround-gate FETs prepared from GeNWs exhibited *p*-type characteristics with I_{ON}/I_{OFF} ratio of ~ 10^5 at -0.5 V source-drain bias (*105*). The capacitance-voltage characteristics of GeNW FET show that the surround-gate FETs have higher capacitance and better electrostatic gate control (*138*). The Ge on insulator *p*-MOSFETs fabricated with plasma-nitrided Ge surface, Al_2O_3 high-*k* gate dielectric, and self-aligned NiGe contacts showed 40% hole mobility enhancement at a high effective field. The observed I_{ON}/I_{OFF} ratio is 3.3×10^5 even at drain voltage of -2.1 V and the observed sub-threshold swing is 71 mV/dec, which was better than those of the bulk and nanowire Ge *p*-MOSFETs reported (*137*). The hysteresis (*35, 105*) in current versus gate voltage is observed for FETs without surface passivations but with surface passivations the hysteresis is negligible (*105*).

The core-shell and core-multishell NW heterostructures were grown by CVD method (*101*). The coaxial FETs were also fabricated which consist of *p*-Si/*i*-Ge/SiOx/*p*-Ge core-multishell NW (*p* stand for *p*-type and *i* stand for intrinsic). *i*-Ge shell served as active channel. The device showed enhancement of capacitance, trans-conductance up to 1500 nAV^{-1} for 1 V source-drain bias. The Si/Ge NWs MOSFETs integrated with HfO_2 gate

dielectric, TaN/Ta metal gate and Pd source/drain electrode showed I_{ON}/I_{OFF} ratio of 10^4 and sub-threshold swing of 97 mV/dec (*136*).

In 2006, Jo et al. (*139*) studied the band gap modulation in Si/Ge NWs. The studies showed that the energy band gap of Si/Ge NWs can be tuned from 0.68 to 2.25 eV. The shift of optical-absorption band edge depends on the Ge content and also on diameter of NWs. This observation can provide interesting applications of Si/Ge NWs in photonics.

The MOSFET integrated with ALD HfO_2 and TaN/Ta gate, was fabricated using phosphorous doped Si/Ge NWs (*121*). The current-voltage (I_{ds}-V_{gs}) curve showed the enhancement mode of *p*-MOS operation with I_{ON}/I_{OFF} of 10^4 (approx.), subthreshold swing of 136 mV/ decade (approx.), and small hysteresis of 90 mV. Three-dimensional, multilayer, multifunctional FETs were fabricated using Ge/Si core-shell NWs (*134*). A uniform high-performance device characteristic was achieved for these devices.

3.1.4 Theoretical Studies on Ge Based Nanowires

Compared to the experimental works on GeNWs and theoretical works on SiNWs, theoretical works reported on Ge based NWs are less and include the following areas: growth mechanisms (*140-141*), molecular structures (*142-146*), electronic (*14, 147-153*), optical (*144, 147, 154*), magnetic (*143*) and mechanical properties (*152*), phonon transport and phonon thermal conductivity (*155-164*) on GeNWs. Monte Carlo simulations were used to study the growth mechanisms and density functional theory (DFT), molecular dynamics (MD) simulations and tight-binding calculations were used to study the molecular structures, electronic structures, and optical properties of GeNWs. Problem of phonon transport and thermal conductivity have been studied by different approaches like Boltzmann transport equation (BTE), molecular dynamics (MD) and the transmission approach.

3.1.4.1 Growth Mechanism

To understand nanowires formation mechanisms, the kinetic 3D lattice Monte-Carlo simulation (KLMC) was performed by Schmidt et al. in 2001(*140*). KLMC code was used for diffusion and reaction of impurity atoms on a 3D fcc lattice. The process includes the nucleation stage, competitive growth of the Ge clusters by Ostwald-ripening and coalescence. The simulated (100) surface has higher surface energy than (110) surface. The evolution of energetically favored (111) facets on the nanowire surface may act as knife and lead to fragmentation of the nanowire. The nanowires aligned to [110] direction having (111) facets is relatively stable at much smaller diameters. So, the stability of the nanowire depends on the relative alignment of the wire. Besides the stability, the KLMC simulations give the indication that the temperature variation is another growth controlling factor. The kinetic Monte-Carlo scheme is also used by Ragade et al. (*141*) to understand faceting, growth directions, and the growth kinetics. The use of dynamic size constraint is the main feature of these simulations. The adatom adsorption and desorption with a set of rate constants were used to model the growth. The linear relationship between the length of nanowire and time was observed.

3.1.4.2 Structural Properties

Chacham et al. (*142*) studied the structures of Si and Ge NWs for three types of structures: diamond-structure, fullerene like and high-density nanowires (shown in Figure 3.5). The nanowire structures were derived from crystalline structures. The calculations were performed by density functional theory. The generalized-gradient approximation (GGA) and norm-conserving pseudopotentials in the Kleinman-Bylander factorized form were used. The LCAO method with a double-zeta basis set plus polarization orbitals was used. An order-*N* density matrix tight-binding (DMTB) method was used to study the energetics of larger

structures. The total energy per atom of bulk phases for cubic diamond (cd), hexagonal diamond (hd), β-tin, simple hexagonal (sh), simple cubic (sc), bcc, hcp, and fcc was calculated first. The formation energies of the high-density sc, sh, and β-tin nanowires, and fullerene like wires (0:9 nm<*D*<1:4 nm range,) are very close to the energies of cd1 and cd2 which indicates that the energetic of wire formation is strongly depends on surface effects.

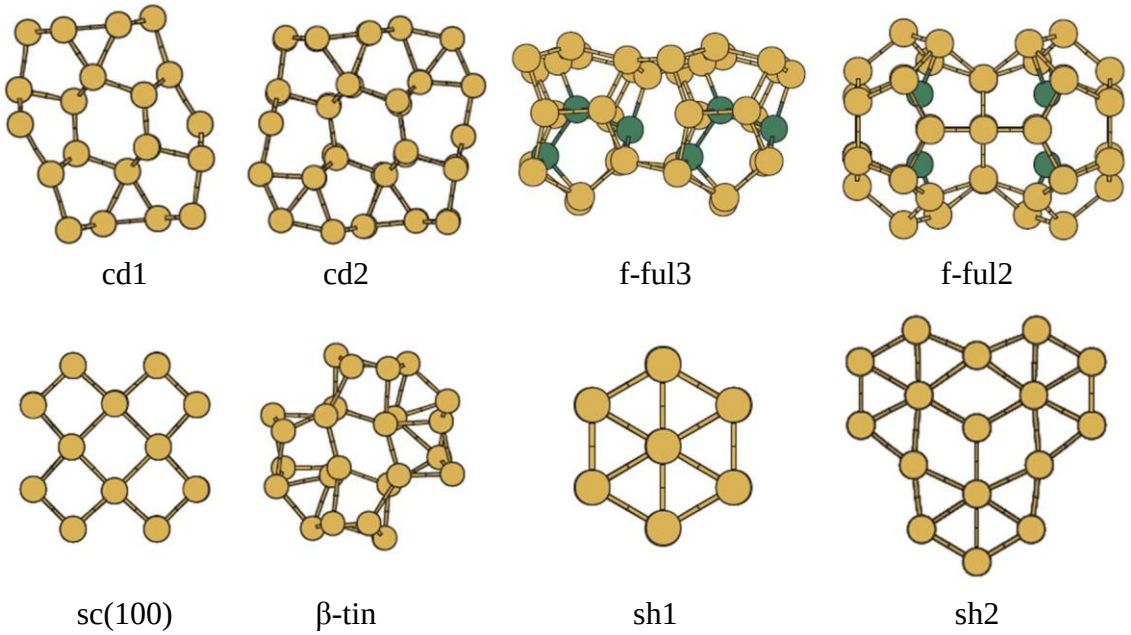

Figure 3.5 Nanowire structures derived from cubic diamond (cd1 and cd2), simple cubic wire (sc), β-tin wire (β-tin), simple hexagonal wire (sh1 and sh2) and from fullerene like geometries (f-ful3 and f-ful2), inner Ge atoms are in green color, others are in yellow color (*142*).

The results also showed that amorphous wires with comparable diameters have higher formation energies than the high-density and the fullerene like wires, the unfilled-fullerene and the empty-hexagon structures have very high energies than the denser structures, sh structure (*D*<0:7 nm) have high stability compared to the other small-diameter geometries and filled fullerene like (0:7 nm<*D*<0:9 nm) wires are the most stable structures. The results suggested that the energetic of nanowire formation is determined by the interplay between the

energies of a bulk part and a surface part of the wire which is further investigated for cd- and sh- based Si and Ge NWs. The results are plotted in Figure 3.6.

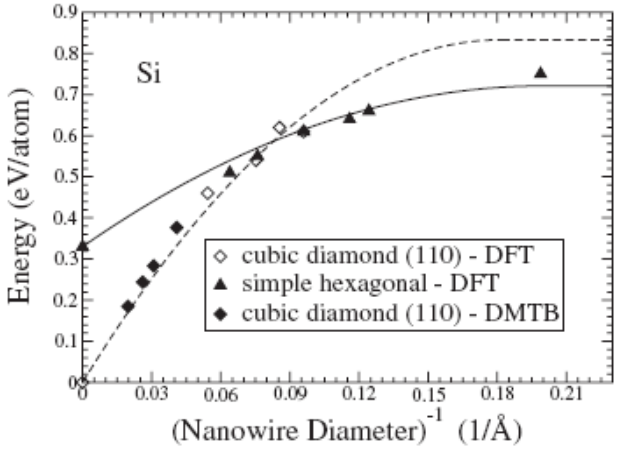

Figure 3.6 DFT and density-matrix tight-binding (DMTB) total energies of SiNWs as a function of inverse of nanowire diameters (*142*).

The results of Figure 3.6 was well fitted by the following expression which is come from a simple continuum model –

$$\varepsilon_{nw} = \varepsilon_s + (\varepsilon_b - \varepsilon_s)\frac{\left(D - 2p^{-\frac{1}{3}}\right)^2}{D^2}, \qquad (3.1)$$

where ε_{nw} is the total energy difference (ΔE_{tot}) for nanowire, ε_b is the total energy difference (ΔE_{tot}) for bulk structure, ε_s is the surface energy per atom of nanowire, D is the diameter of the wires and ρ is the number of atoms per volume for the bulk structure. The applicability of the equation is verified by density-matrix tight-binding (DMTB) calculations. This equation is not applicable for filled-fullerene geometries because no bulk structure is associated with these geometries).

The geometry of GeNWs was optimized by Fazzio et al. (*143*) based on spin-polarized density-functional theory within the generalized gradient approximation for the exchange-correlation potential using ultrasoft pseudopotentials and a plane-wave expansion.

The optimized average Ge-Ge bond lengths around centre and surface are 2.49 and 2.47 Å, respectively and the average Ge-H bond length in surface is 1.54 Å (*143*). The geometry of GeNWs was also optimized by Borisenko and Migas (*144*) using the first principles total-energy ultrasoft pseudopotential method with plane-wave basis set. The exchange and correlation potentials were included using local density approximation (LDA) of Ceperly and Alder with parameterization of Perdew and Zunger. The optimized shape of the nanostructures is slightly protuberant when the dimers are formed otherwise concave when dimers are broken. The unit cell parameter of NWs with dimers is smaller (1-2%) than the NWs without dimers. Another study (*145*) showed that the Ge-Ge bond lengths in two Ge dimers bridged by Pt pairs are 2.31–2.39 Å, which is much smaller than bulk Ge.

A molecular dynamics (MD) simulations (*146*) were performed to study the structures of GeNWs. The Ge-Ge interactions were described by many-body empirical potentials. The ground-state structures of nanowires were found by using the standard simulated annealing global optimization technique. The study showed that the atoms on (100) surfaces form 2x1 dimers (0.249nm in length) results in distortion of the lattice spacing of the whole wire and there is no reconstruction on the (110) surfaces.

3.1.4.3 Electronic Properties

The band structures of GeNWs were studied by both density functional theory and tight-binding calculations. In 2004, Ossicini et al. (*147*) studied the effect of spatial orientations on the electronic properties for freestanding Ge wires passivated with hydrogen atoms along [100], [110] and [111] directions by the linearized augmented plane wave (LAPW) implemented into the WIEN97 code. The structures of NWs are shown in Figure 3.7. It was observed that the well-resolved direct band gap in [110]-oriented Ge quantum wires appeared at the Brillouin zone (BZ) center and the valence-band maximum (VBM) is

composed of pure *p*-states of core Ge atoms while the conduction-band minimum (CBM) is composed of *s*-states with some admixture of *p*-states of both the core and surface Ge atoms.

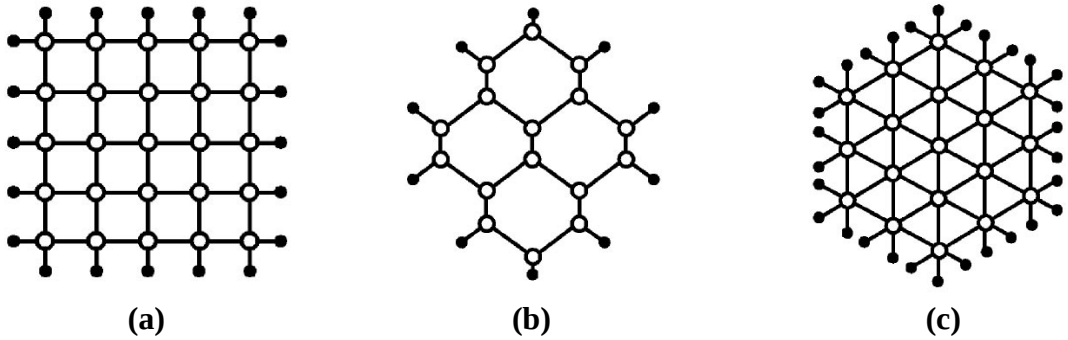

Figure 3.7 Structures of hydrogen passivated GeNWs along (a) [100], (b) [110] and (c) [111] directions, black dots are hydrogen and hollow circles are germanium (*147*).

The orbital compositions of both [100] and [111]-oriented quantum wires are similar to [110]-oriented Ge quantum wires and the VBM for both are situated at the BZ centre with the CBM shifted towards its edge. The band gap in [100] and [111 Ge quantum wires is indirect while the band gap in [110] is direct. The absence of dangling bond like states within band gap region for all wires suggested the saturation of dangling bond by hydrogen. The band gap along all the directions followed the order E_g[100]> E_g[111]> E_g[110] and decreases monotonically with the increases of wire width (shown in Figure 3.8) (*147*).

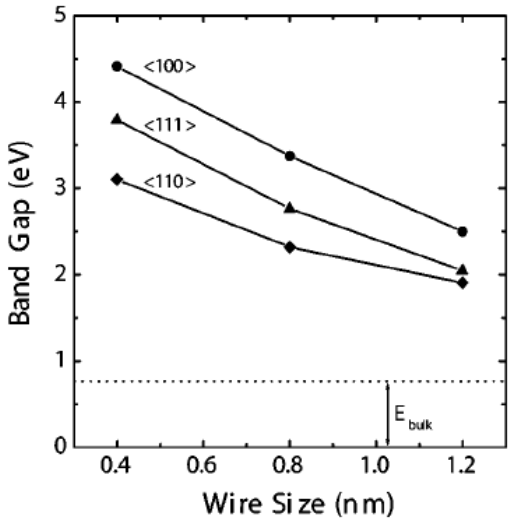

Figure 3.8 Effects of wire size on band gap of Ge quantum wires (*147*).

A DFT pseudopotentials method was performed to study the quantum confinement effects in hydrogen passivated Ge (110) NWs. The results showed that the band gap decreases with increases of the diameter and approaches to bulk Ge (*148*). The change in HOMO-LUMO gap of GeNWs with diameter greater than 1.4 nm is due to confinement of CB states. The HOMO-LUMO gap was fitted with diameter by following expression –

$$E_{gap}(D) = \frac{\alpha}{D^{\beta}} + 0.44\,, \qquad (3.2)$$

where α = 1.20 and β = 0.98. The shape and energies of conduction band of GeNWs (d < 3.0 nm) are strongly affected by quantum confinement. But the energy of valence-band maximum is not affected with d > 2.0 nm (*148*).

The band gap along the [100], [110] and [111] directions by sp3d5s* tight binding calculations (*149*) for GeNWs followed the same order reported by Ossicini et al. (*147*). The change in band gap with wire width is shown in Figure 3.9. The difference between energy gap of the Ge [100] and Ge [110] remains constant with increases of nanowire width while for SiNWs the energy gap decreases with width.

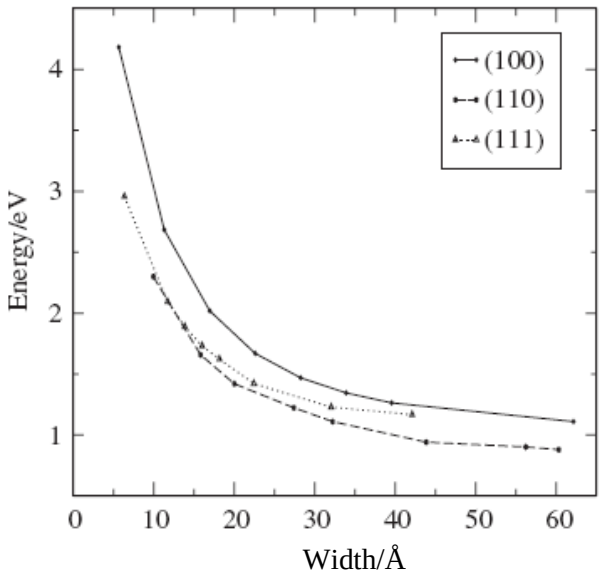

Figure 3.9 The change of band energy of GeNWs with size in (100), (110) and (111) directions. [Reprinted with permission from ref. (*149*). Copyright 2006, Elsevier B. V.]

The study also showed that the variation of zone centre band gap depends on nanowire stacking direction for example, the zone centre band gap converge to different bulk band gap for [100] and [110] GeNWs, the [110] gap converges towards the *Γ-L* gap but [100] and [111] converge towards *Γ-X* gap (*149*). The GeNWs have a direct band gap only along [110] direction while the SiNWs have a direct band gap in all directions. This may be the reason to limit the use of GeNWs for production of light.

The band structures of GeNWs passivated with hydrogen and ethane along [100], [110], [111] and [112] were investigated by using the ultrasoft pseudopotentials plane wave program for different wire diameters (*150*). This study also showed that the fundamental band gap increases with the decrease of size. But one exception is that the band gap of [110]-oriented wire at d = 6.6 Å is smaller than band gap of wire at d = 8.7 Å. The orbital analysis showed that the surface hydrogen atoms have very little contribution to the conduction band and have no contribution for valence bond for wire d = 8.7 Å, but have contribution to both the band for wire d = 6.6 Å. All the (110)-oriented wires have direct band gap. The (112)-oriented wires have indirect band gap even at d = 3.9 Å. The study showed different result for the nature of band gap of [100] and [111]-oriented wires which have direct band gap at the size of less than 12 and 10 Å, respectively. The fully relaxed hydrogen passivated GeNWs have direct band gap. The nature of band gap of the [100] and [111]-oriented wires is sensitive to their lattice constant (relaxed or un-relaxed lattice constant). The difference between direct and indirect band gap obtained for LDA is greater than GGA (*150*). The theoretical and experimental band gap of Ge is smaller that Si. The nature and magnitude of (100) and (111)-oriented SiNWs and GeNWs are fairly similar and the quantum confinement effect is stronger in GeNWs than SiNWs (*150*). The VBM in ethane-passivated GeNWs is located in *Γ* while the CBM is shifted to *X* point. The hydrogen atoms have no contributions towards CBM and/or VBM, but the CH_2 groups have contributions towards both the CBM

and VBM. Thus, the quantum confinement effect is less in ethine-passivated GeNWs as compared to the hydrogen passivated GeNWs (*150*).

The DFT studies on [110] and [111]-oriented core-shell Ge/Si or Si/Ge nanowires (shown in Figure 3.10) were performed by Musin and Wang (*151*). Two strategies were used to study the effect of compositions. Firstly, the number of total atoms was fixed while changing the number of core and shell atoms. Secondly, the number of core atoms was fixed while changing the number of shell atoms.

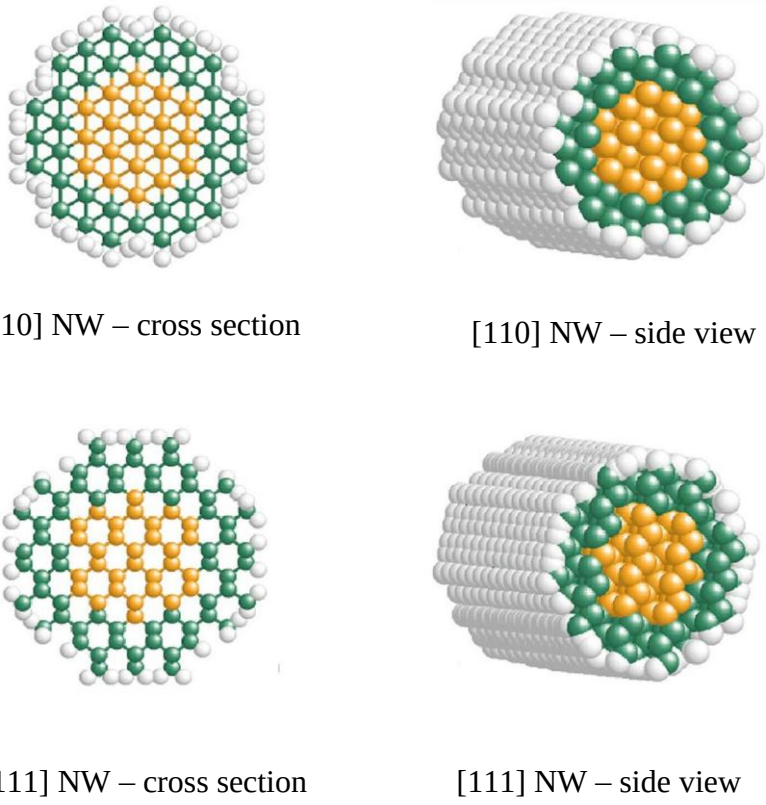

Figure 3.10 The cross section and side view of Si/Ge core-shell NWs along [110] and [111] directions, Si is in yellow, Ge in green and hydrogen in white color (*151*).

The results showed a nonlinear relation of band gap energies with composition when diameter is fixed, but showed a linear relation with the fixed core size and varying shell thickness for direct band gap (*151*). Since, the Si/Ge or Ge/Si nanowires is cylindrical in

shape, the fundamental band gap showed linear relation with inverse square of wire radius which is good agreements with experimental data. The results also showed the linear dependence of energy gap of [110] and [111] oriented SiNWs and GeNWs with inverse of atom numbers (N) and expressed by following form –

$$E_{gap}(N) = E_{gap}(\infty) + \frac{A}{N}, \qquad (3.3)$$

where $E_{gap}(\infty)$ is the bulk limit value of energy gap, A is an adjustable parameter. The above equation is valid also for ultrathin NWs of diameters as small as 1 nm.

The first principles plane-wave calculations within DFT showed that the bare Ge_n, Si_n, (n = 25, 57) and Si_nGe_n (n = 75) nanowires are metallic due to surface dangling bonds, but by hydrogen passivation these nanowires become semiconducting (*152*). The hydrogen passivated SiNW (H-Si_{150}) and GeNW (H-Ge_{150}) have indirect band gap of 1.1 and 0.7 eV, respectively. The unexpected nature was observed for bare Si_nGe_n which is semiconductor for n = 75 and 114 (*152*).

A DFT study performed within GGA showed that the GeNWs along [110] growth direction have direct band gap of 0.53, 0.78, 1.00 and 1.34 eV for diameters 35.00, 27.00, 18.70 and 14.70 Å, respectively while along [111] growth direction have indirect band gap of 0.97, 1.36 and 1.94 eV for the diameters 22.20, 17.50 and 12.60 Å, respectively (*14*). In GeNWs growth in [111] direction, the energy difference between two minima in conduction band remains unchanged but in [110] direction the difference increases with the decrease in diameter (*14*).

The dopants like B and P have an impact on band structures of GeNWs. Addition of *p*-types dopant shifts the Fermi level towards VB and increase the energy of maximum of the VB and the minimum of the CB while *n*-types dopant has opposite effects and also the addition of dopant has little effect on the dispersion of VB and CB (*153*).

3.1.4.4 Optical Properties

The optical properties of Ge quantum wires were studied by Ossicini et al. (*147*). The results showed the different anisotropy of optical spectra with different orientation of the wires and the anisotropy is increased as the wire become narrower. The dielectric function for [110] and [111] oriented wires is larger for z-polarizations near the edge but the dielectric function variations for [100] oriented wires are similar in energy for x and z polarizations. The intensity and positions of peaks in dielectric functions at high frequency region do not change significantly. Since the imaginary part of dielectric function is directly related to absorption coefficient, the peak in optical spectra indicates a strong absorption of photons at visible light for [110]-oriented wires. The increase in effective width of the wires results in shifting of peak in low energy region and decreasing intensity of the peak. This indicates the quantum size effect.

Bruno et al. in 2007 studied the optical properties (*154*) of GeNWs and SiNWs. The observed optical spectra are shown in Figure 3.11. The top spectra are including self-energy corrections and bottom spectra are including excitonic effects. The results showed large oscillator strength near the onset of optical absorption for GeNWs but not for SiNWs when the self-energy corrections are included. When the excitonic effects are included the oscillator strength is transferred below the electronic gap and a strong optical peak is observed in visible range for GeNWs with d = 0.8 nm.

The oscillator strength is also observed for SiNWs, GeNWs and SiGeNWs with dimmers (*144*). For SiNWs, SiGeNWs and Si/Ge core-shell NWs, the maximum in dielectric function (imaginary part) curves appeared at about 4 eV. The peak becomes broader for GeNWs with dimers and splits into two parts for GeNWs with GeH_2 species.

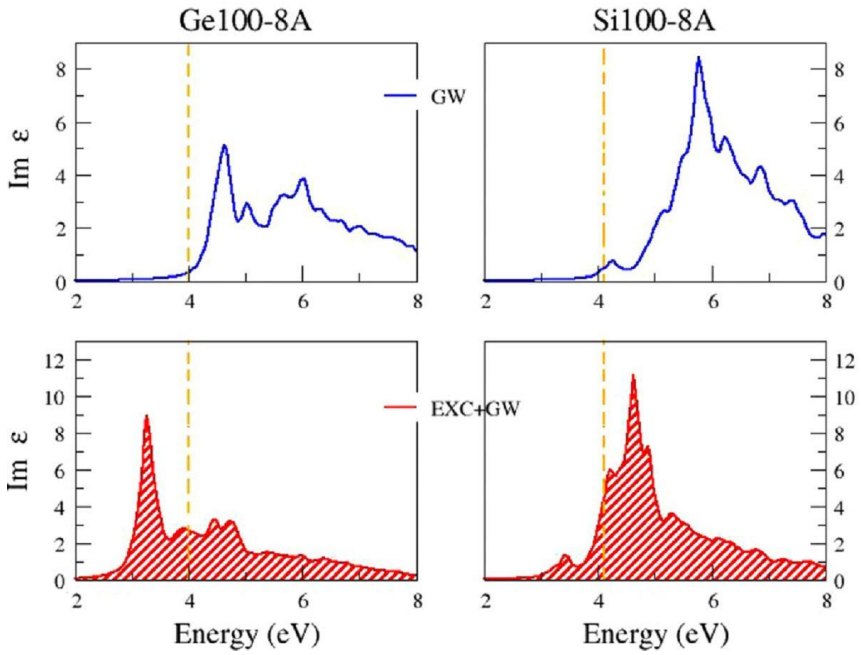

Figure 3.11 Optical spectra of GeNWs and SiNWs. Top blue curve is including self-energy corrections and bottom red curve is including excitonic effects. [Reprinted with permission from ref. (*154*). Copyright 2006, Elsevier B. V.]

3.1.4.5 Magnetic Properties

The magnetic properties of Mn-doped GeNWs were studied by Arantes et al. (*143*). The Mn-Mn coupling is studied to understand the magnetic ordering by replacing two Ge atoms by Mn and enforcing different total spin configurations. The total energies were calculated for two spin states (ferromagnetic, FM and anti-ferromagnetic, AFM). The energy differences are plotted against Mn-Mn distances (see Figure 3.12). From the figure we observed that there is no AFM-FM oscillatory behavior in the wire and also the ferromagnetic coupling is similar for Mn-Mn distances ranging from 4.0 to 8.0 Å. The transition metals adsorbed on GeNWs surface results in GeNW with different electronic and magnetic nature depending on the nature of transition metals, i.e. nonmagnetic metals (Sc, Cu) or semiconductors (Ni, Zn), weak-ferromagnetic metals (Ti, V), ferromagnetic semiconductor (Cr), and the ferromagnetic half-metals (Mn, Fe, Co) (*165*).

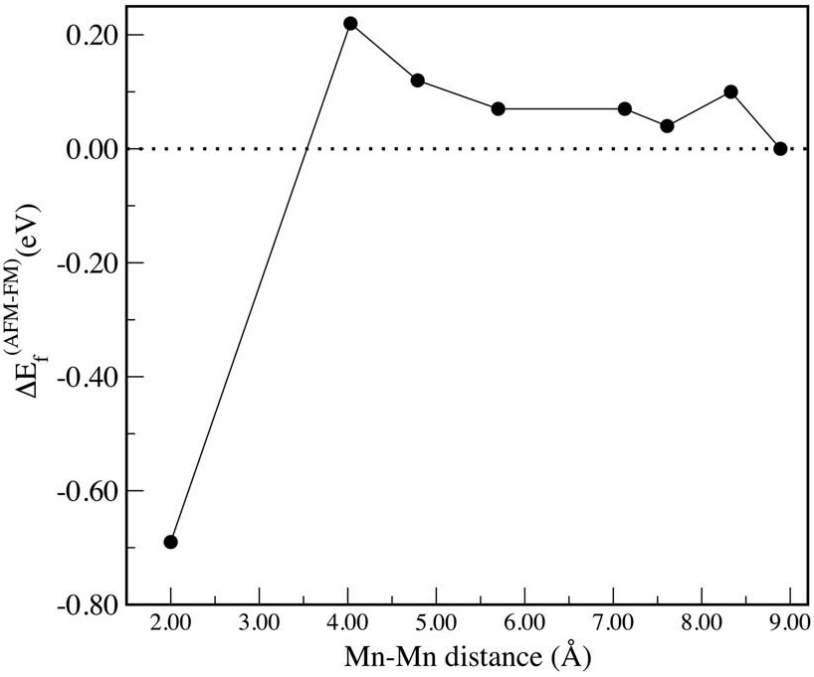

Figure 3.12 Total energy differences between the AFM and FM as a function of Mn-Mn distance (*143*).

3.1.4.6 Mechanical Properties

In 2007, Akman et al. (*152*) investigated the mechanical properties of Si_n NWs, Ge_n NWs and Si_nGe_n NWs superlattices. The study showed that the Si_n NWs are stiffer than Ge_n NWs. This indicates that the lattice mismatch in Si_nGe_n NWs superlattices between Si and Ge is mainly due to Ge zone. After hydrogenation both Si_n NWs and Ge_n NWs and also the Si_nGe_n NWs superlattices become stiffer. The force (spring) constant κ increases with increase of cross section of the wires. The strain ratio of the Ge zone to Si zone for $Si_{75}Ge_{75}$ under tensile stress is calculated to be 2.5, which is reduced to 1.25 for $Si_{114}Ge_{114}$. This indicates that the Ge zone is more elongated than Si zone in Si_nGe_n NWs superlattices.

3.1.4.7 Phonon Transport and Thermal Conductivity

The problem of phonon transport in Ge and Ge/Si based nanowires, nanowires superlattices and nanocomposites have been studied by different approaches like Boltzmann

transport equation (BTE), molecular dynamics (MD) and the transmission approach, etc (*155-164*). The phonon transports in nanowires with long resistive length at high temperatures were successfully studied by BTE. MD can accurately consider the anharmonic interactions between atoms, but it is difficult to study the system with low temperatures using MD. The transmission function approach can be used to study the phonon flows ballistically or semiballistically. This method is also used successfully to study the heat flow through a mesoscopic link, a nanocrystal and monatomic chains (*166*). In the following section the theoretical study on phonon transport in Ge and Ge/Si based nanowires are discussed.

In 2004, Chen and Dames (*155*) developed an incoherent particle model to calculate the phonon thermal conductivity of Si/Ge superlattice nanowires. The model is the extension of photon net-radiation method and Schuster-Schwarzschild approximation. The model was developed assuming the incoherent three-dimensional dispersion, because it is hard to achieve a smooth and uniform surface for coherent interfaces, experimentally. The calculated thermal conductivity of SiNWs with d = 22 nm is in poor agreement with experimental data but is good for wires $d \geq 37$ nm. For $Si/Si_{0.9}Ge_{0.1}$ superlattice nanowires of 58 and 83 nm diameter, the calculated thermal conductivity is in good agreement with experimental data at temperatures outside 30 and 150 K.

Yang et al. (*157*) developed a model to study the phonon transport and thermal conductivity of silicon-germanium nanowire composites in longitudinal direction. The model is valid for periodic composites. The results showed that the effective thermal conductivity changes with volumetric fraction of constituents, radius of nanowires and cylindrical pores. The effective thermal conductivity of bulk SiGe composites increase with the increase in cross-sectional area or volumetric ratio of Si. For large volumetric ratio of Si, the effective thermal conductivity of nanocomposites followed the same trend like macrocomposites. For small volumetric ratio of Si, the thermal conductivity increases with increase in low thermal

conductivity component. The effective thermal conductivity of Si-Ge nanocomposites decreases with the decrease of radius of wire inclusion. Studies on simple and tubular nanowire composites showed that the tubular composites have lower thermal conductivity than simple composites.

Thermal conductivities of Si-Si and Si-Ge NW composites were investigated by Monte Carlo simulation (*161*). The thermal conductivity decreases with the size of wires and become almost temperature independent for smaller size of the wire. The non-equilibrium Green's function method also showed that the thermal conductivity of Si-Ge NWs increases with the size at moderate temperature (*162*).

The surface functionalizations of GeNWs with different chemical groups like Cl, F, SH, alkene, alkyne and diene species have been studied experimentally to prevent the problems of oxidation hysteresis in electric current of GeNWs, while the structural and electronic properties of hydrogen passivated GeNWs (H-GeNWs) have also been widely studied theoretically. To the best of our knowledge, there are no theoretical reports on OH passivated GeNWs (OH-GeNWs). In this work, we apply DFT calculations to evaluate how the water molecule adsorption on the GeNW surface would affect its electronic properties and reveal the possible cause of electrical hysteresis in GeNW based electronic devices. Another surface issue is the dangling bond defects. Recently, researchers are trying to add surface defects by creating surface dangling bonds to nanomaterials for better properties, e.g., the surface defects together with non-magnetic dopants in silicon nanowires lead to half-metallic properties. Thus, we also study the defect induced electronic and magnetic properties of GeNW and predict that the half-metallic GeNW can be achieved via solely manipulating the structures and surfaces of GeNW.

3.2 Carbon Nanotubes

In this section, we briefly mentioned the properties and applications of CNTs and the separation strategies used to separate CNTs and theoretical works reported on interactions of molecules/ radicals with SWNTs.

3.2.1 Properties and Applications of CNTs

CNTs exhibit unique mechanical, electronic and thermal properties. The presence of sp^2 bonds in CNTs makes them the strongest and stiffest materials. The tensile strength and Young's modulus of single-walled carbon nanotubes (SWNTs) can be upto 20 GPa and 1 TPa, respectively. The electronic properties of CNTs depend on its chirality. Based on chirality it can be either metallic or semiconducting. The SWNTs showed ballistic conductance due to weak acoustic phonon scattering in metallic SWNTs (*167*) which makes metallic CNTs an excellent conductor (*168*) with an extremely high current density up to 4×10^9 A/cm^2 and a carrier mobility of 10,000 $cm^2V^{-1}s^{-1}$ (*169*). The semiconducting SWNTs exhibit varied band gap ranging from 0.4-0.07 eV which depends on the diameter of tubes (*170*). The SWNTs are the promising candidates for many applications due to its unique properties. Due to its mechanical properties, the SWNTs have potential applications in polymer composite (*171*), probe tips (*172*), membrane filters (*173*), etc. The SWNTs have potential applications in field effect transistors (*174*), thin film transistors (*175*), memory devices (*176*), sensors (*177*), field emission displays (*178*), etc. due to its unique electronic properties. The SWNTs also have potential applications such as super-capacitors (*179*), solar cell materials (*180*). The SWNTs also have variety of bio-applications like in cell and tissue imaging (*181*), drug delivery (*182*), etc. However, the main challenge of these applications is the availability of high purity SWNTs.

3.2.2 Separation of CNTs

It is well known that the as-synthesized CNTs contain about one-third of metallic and two-third of semiconducting. The separation of metallic and semiconducting CNTs is essential for the applications of CNTs. The separation techniques used for separation of semiconducting CNTs from metallic CNTs includes synthetic strategy of selective growth, dielectrophoresis (*51-53*), density gradient ultracentrifugation (DGU) (*54-55*), chromatography (*56*), gel-based separation techniques (*57*), surfactant extraction (*58-60*), selective aromatic extraction (*61-62*), amine extraction (*56*), electrical breakdown of metallic nanotubes (*63-64*), etc. Recently, small aromatic molecules are used to functionalize the CNTs for the selective separation of SWNTs. Thus, the theoretical studies on the interactions of molecules/ radicals with SWNTs are necessary to understand the binding mechanism of these surface species with SWNTs. In following section, we briefly reviewed the theoretical works reported on interactions of surface species with SWNTs.

3.2.3 Theoretical Studies on CNTs

3.2.3.1 Interactions of CNTs with Molecules

Azizi et al. (*183*) studied the interaction of carbon monoxide (CO) with armchair SWNT using DFT B3LYP methods. The interaction between CO and SWNTs is physisorption in nature. The CO molecules strongly bind with SWNT when interacts via oxygen head. They found that the dispersion force play major role in total adsorption energy rather than electrostatic interaction.

In 2007, Woods et al. (*184*) studied the interaction of benzene and its derivatives with SWNT (8,0) using DFT method in VASP code. Their study showed that the equilibrium distance between benzene and the CNT for their hollow, top and bridge model is 3.22, 3.12 and 3.12 Å, respectively. The binding affinity of benzene is less than its derivatives, aniline,

toluene and nitrobenzene. Their calculated binding energies and equilibrium distance are consistent with physisorption. The study also showed that the binding energy of ammonia and methane molecules is less than benzene and its derivatives.

B. B. Shirvani et al. (*185*), studied the NH_3 adsorption on zigzag SWNT (5,0), (8,0) and armchair SWNT (5,5) and (6,6) at the level of B3LYP/6-31G*. The calculated binding energy of NH_3 with (5,0), (8,0), (5,5) and (6,6) is -112, -50, -11, -3 meV respectively. Their results showed that NH_3 has more binding affinity towards zigzag CNTs as compared to armchair CNTs. The binding affinity also decreases with the increase in diameter of CNTs.

3.2.3.2 Interactions of CNTs with Atoms/ Radicals

N. Park et al. (*186*), studied the interactions of Br with zigzag SWNTs (8,0), (9,0), (10,0), (17,0) and (18,0) using DFT within a local density approximation (LDA) with energy cut-off of 50 Ry. The binding energy of Br with metallic SWNT (9,0) and (18,0) is -1.33 and -1.45 eV, respectively. The binding energy of Br with semiconducting SWNT (8,0), (10,0) and (17,0) is -1.16, -1.26 and -1.40 eV, respectively. Their results also showed that Br has more affinity towards metallic as compared to semiconducting and the binding affinity increases with the increase in the diameter of CNTs. Baei et al. (*187*) study the interaction of OCN radicals with various CNTs using DFT B3LYP method as implemented in Gaussian 98 program. They used the cluster model of CNTs. Their results showed that the binding energy of OCN radicals with CNTs is slightly more when the N atom of OCN radical interacts with CNTs.

3.2.3.3 Interactions of CNTs with Metals

The transition metal atoms bind strongly with small diameter SWNTs as compared to graphene sheet (*188*). The Co atom binds with graphene, SWNT (4,4) and SWNT (8,8) with

binding energy of -1.58, -1.86, -1.63 eV, respectively at hollow site (*188*). Most of the transition metal atoms favor hollow site (*188-189*) and prefer outer side (*188, 190-191*) for binding interactions with SWNTs. The transition metals like Sc, Ti, V, Cr, Mn, Fe, Co, Nb, Mo, and Ta preferred hollow site on SWNT (8,0) with binding energy varies from -2.10 to -4.60 eV for spin-unpolarized calculation except Zn which has binding energy of -0.05 eV. The transition metal Ru binds strongly on SWNT (or graphene) surface with binding energy of ~ 3.20 eV and the Ru atom prefers outer side of CNT (*191*). The Pt atom also prefers the outer side of CNT for interaction (*190*). Inntam and Limtrakul (*192*) studies interactions of M species and M2 dimers (M = Cu, Ag and Au) on pristine and defective armchair SWNT (5,5) using DFT B3LYP method using 6-31G(d,p) basis set as implemented in Gaussian 03 program. The cluster model of CNTs was used for their study. They found that the metal cations bind strongly with both the primitive and defective SWNT as compared to metal anions. The strong interaction of metal cations with SWNTs is due to transfer of electron density between metal species and CNTs and electrostatic attraction counteracted by Pauli repulsion. The Cu and CNT complexes are the most stable as compared to others. The Cu species binds strongly with several surface carbon atoms on CNTs but for Au and Ag directly binds on top site. The metal species prefer to deposit on the defect site particularly in vacancy site as compared to pristine CNTs due to lesser Pauli repulsion and easier polarization of electron densities.

3.2.3.4 Interaction of Diazonium salts with CNTs

In 2009, Wang and Xu (*193*) theoretically studied the two-step mechanism in fuctionalizations of SWNTs by aryl diazonium salts using the ONIOM (B3LYP:UAM1) method. ONIOM techniques model large molecules by dividing the structure into two or three layers that are treated at different computational level, i.e., low-level, medium-level,

high-level, etc. Wang and Xu (*193*) used the B3LYP method as high-level and AM1 method as low-level. The B3LYP method is used for top 16 carbon atoms and terminal hydrogen atoms of nanotube using 6-31G* basis set while the AM1 method is used for the rest atoms including the reacting species (i.e. aryl diazonium or aryl radical). They used the cluster model for SWNT (5,5). Their study showed that the adsorption of diazonium on CBTs occurred via two steps. First the diazomium forms charge transfer complex with CNTs (IN). The IN complex then decomposes to form a covalent bond.

The most of the theoretical studies reported on CNTs used cluster models. In our current study we use periodic models of CNTs to investigate the interactions between molecules/ radicals with SWNTs to understand the binding properties and hence, the separation mechanism of metallic CNTs from semiconducting CNTs.

Chapter 4

Theoretical Studies on Germaallenes

In order to design Ge based nanowires, an important building block of GeNWs, germaallene firstly selected to get familiarize with molecular modeling and different computational theory. The knowledge about germaallene structures, nature of bonding and electronic properties can be used as the starting point to understand the bonding and electronic structures of GeNWs. Germaallenes are heavier group 14 analogues of allene which have attracted much attention of experimental and theoretical chemists due to their

different bonding, structures and reactivities from allene (*194-209*). In 1998, West et al. had synthesized the first stable germaallene (*201*), 1-germaallene, which was protected by the bulky substituent and in 2005, Kira et al. (*206*) isolated and characterized the first stable compound with cumulative "Ge=Ge" bond, trigermaallene and also by other groups. Although there are more reported experimental works on germaallenes, the corresponding theoretical research is limited and mainly studied by Apeloig et al. (*207-208*). The computational methods and results of present theoretical studies on five germaallene molecules for molecular structures, chemical bonding, hyperconjugation and stability are discussed below:

4.1 Computational Methods

The atom numberings in germaallenes and its cyclic isomers **3-10** used throughout the text are shown in Figure 4.1. All calculations were performed by the DFT B3LYP (Becke's three-parameter hybrid function (*79*) with the non-local correlation of Lee-Yang-Parr (*80*)), MP2 (the second-order Møller–Plesset perturbation theory) (*67-68*) and CCSD (coupled cluster theory including single and double excitations) (*69-72*) methods with a variety of basis sets. The calculations were carried out using Gaussian 03 suite of programs (*81*).

The bending PESs of germaallenes were obtained by decreasing $\angle M_1M_2M_3$ (M=Ge, C) from 180° to 60° or 30° by a step size of 15°. The $\angle M_1M_2M_3$ bond angle was kept constant while other parameters were optimized at the B3LYP/6-311+G(d,p) level (*210*) (our previous works (*211-212*) have justified that the 6-311+G (d,p) basis set is sufficient for the current work) and no symmetry restriction was kept at the course of germaallene bending. The geometries of stationary points along the bending PES were fully optimized and frequency analyses were performed in order to ensure that the located structure is either a minimum or a transition state (TS) and evaluate zero-point energies (ZPEs) for correcting the

relative energies. The NPA analysis and the NBO hyperconjugation stabilization energies were obtained by the Natural Bond Orbital program (NBO 3.1) (*82*), which is implemented in Gaussian 03 (*81*).

4.2 Optimized Geometries of Germaallenes and their Cyclic Isomers and the NPA Analysis

The structures of five germaallene molecules are shown in Figure 4.1. We first locate germaallenes and their cyclic isomers along the skeleton of the bending PES of germaallenes (see Figure 4.2) and then elucidate the bonding nature based on the NPA analysis. To show concisely the geometry of germaallenes and for ease of discussion, we define the $\angle M_1M_2M_3$ (M = Ge, C) bond angle as α; and the sum of the bond angles around terminal M atom as $\Sigma\theta$, $\Sigma\theta = \theta_1 + \theta_2 + \theta_3$ (see Figure 4.3). For the ease of presenting our discussions and conclusions, our reported values below will be based on calculations at the B3LYP/6-311+G(d,p) level, unless otherwise specified (*213*).

4.2.1 Monogermaallenes

The relative stabilities on germaallenes, their cyclic isomers and the transition states along the bending PES are given in Table 4.1. The present optimization on 1-germaallene **3** and 2-germaallene **4** supports previously reported geometries by Sigal and Apeloig (*207*). The 1-germaallene (**3**, C_s symmetry) and 2-germaallene (**4**, C_2 symmetry) are bent at the central atoms with α=162.9° and 176.0°, respectively (see Figure 4.1). The optimized geometry of 1-germaallene **3** is almost identical to the reported single crystal structure (*201*). We also have optimized a weak-bent minimum with C_2 symmetry for 2-germaallene **4**, (see Appendix A) which is close to the unconstrained geometry reported previously by Apeloig (*207*). The energetic of 1-germaallene **3** and 2-germaallene **4** are of comparable stability with

their linear structure (see Table 4.1 and Figure 4.2) (*213*).

Table 4.1 Relative energies (in kcal/mol) of germaallenes, their cyclic isomers and transition states along respective bending PESs to their linear structures. [Reprinted with permission from ref. (*213*). Copyright 2004, American Chemical Society]

Molecules	Linear structure	Stable structure	TS	Cyclic isomer
GeH_2=C=CH_2	0.0 (0.0)[a] [0.00][b]	-0.63 (-0.46)	-	-
CH_2=Ge=CH_2	0.0 (0.0) [11.45][b]	-0.01 (0.05)[c]	14.43 (14.25)	-37.83 (-35.25)
GeH_2=Ge=CH_2	0.0 (0.0) [0.00][b]	-15.32 (-15.56)	-12.36 (-12.58)	-26.89 (-26.40)
GeH_2=C=GeH_2	0.0 (0.0) [15.62][b]	-	-	-
GeH_2=Ge=GeH_2	0.0 (0.0)	-30.71 (-30.12)	-24.52 (-24.46)	-24.58 (-24.37)

[a] The value in the parenthesis is the relative energy corrected with zero-point energy. [b] The relative energy (with zero-point energy correction) of linear structures in monogermaallene and digermaallene groups. The total energies of GeH_2=C=CH_2 **3** and GeH_2=Ge=CH_2 **6** are -2155.50502 and -4194.42988 a. u., respectively. [c] The relative energy at the CCSD/6-311+G(d,p) level is -0.38 kcal/mol.

Their bending PESs show that 1-germaallene **3** has no stable cyclic isomer and the global minimum of 2-germaallene **4** is the cyclic isomer (germacyclopropylidene) with α=43.1°, which is lower in energetic than 2-germaallene **4** by 35.25 kcal/mol (see Figure 4.2). Because the energetic barrier from 2-germaallene **4** to its cyclic isomer **5** is the largest of five germaallenes (14.21 kcal/mol, see Figure 4.2), 2-germaallene **4** and its cyclic isomer are dynamically stable. The GeC_1 bond of germacyclopropylidene **5** is elongated to 2.032 Å, which is slightly longer than normal Ge-C single bond (1.969 Å) and C_1C_2 bond length

(1.492 Å) of **5** is close to normal C-C single bond length (1.531 Å) (*213*).

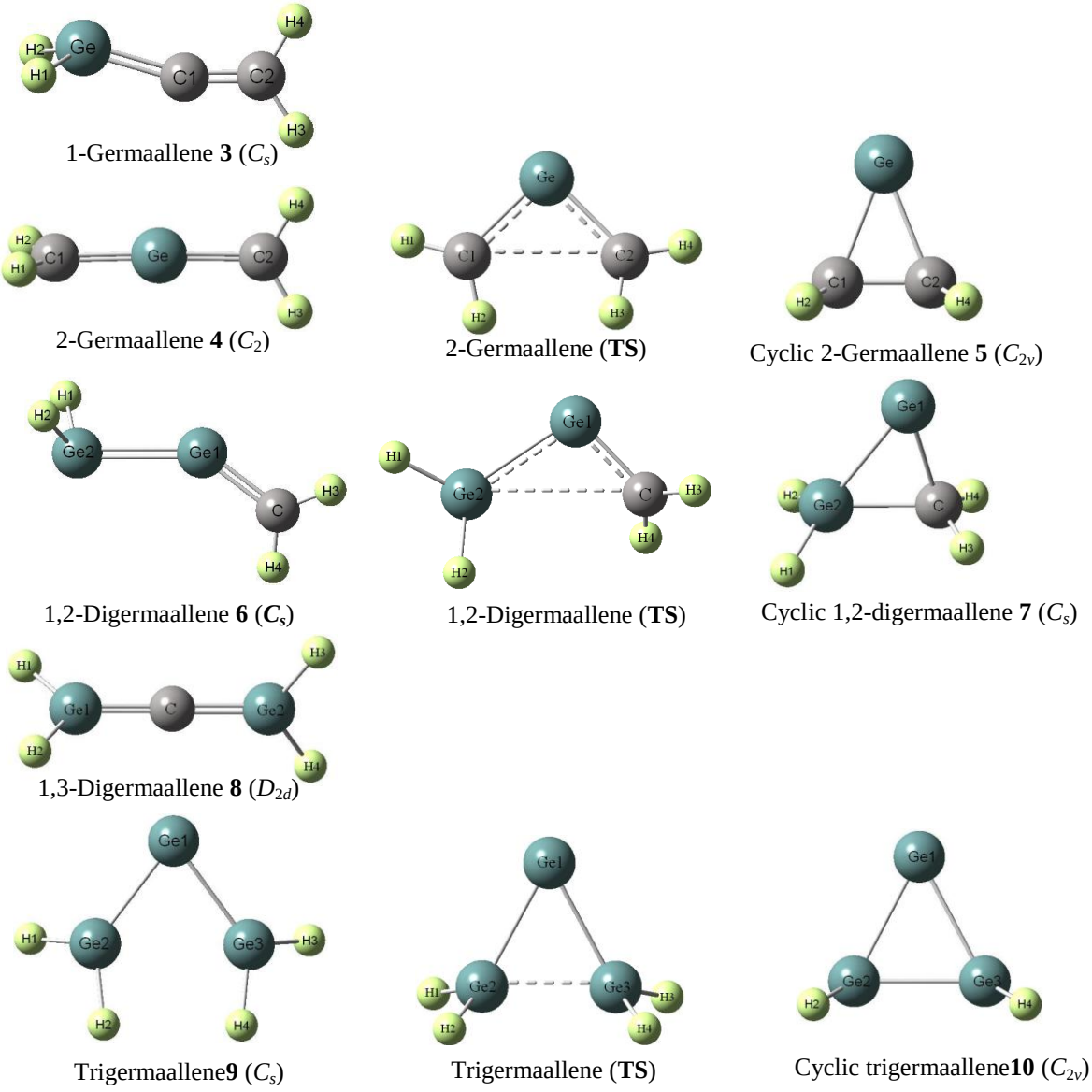

Figure 4.1 The optimized structures of germaallenes and their respective cyclic isomers and transition state bending from the linear or bent structure to the cyclic structure. [Reprinted with permission from ref. (*213*). Copyright 2004, American Chemical Society]

We use the Wiberg Bond Index (WBI) (*214*) as a criteria to estimate the bond order. The WBI values for the $Ge{=}C_1$ and $C_1{=}C_2$ bonds of 1-germaallene **3** are 1.709 and 2.075 respectively (see Table 4.2), close to 2, indicating that the $Ge{=}C_1$ and $C_1{=}C_2$ double bonds remain mainly intact in 1-germaallene. The $\sigma_{Ge\text{-}C1}$ bond of 1-germaallene **3** is composed of a

sp hybrid orbital (central C_1 atom) interacting with a $sp^{2.17}$ orbital (terminal Ge atom) and the $\pi_{Ge=C}$ bond of 1-germaallene **3** is composed of an impure *p* orbital (including 7.1% *s*-character) on Ge interacting with another *p* orbital on C_1 atom. The *s*-character increases in the $\pi_{Ge=C1}$ bond of 1-germaallene **3**, allowing the two *p* orbitals to bend away from the line of Ge-C_1 center by 100.0° and 101.6°, respectively. Therefore, the electron cloud does not distribute equally around the internuclear line between the Ge and C_1 atoms (see Figure 4.4(a)) (*213*).

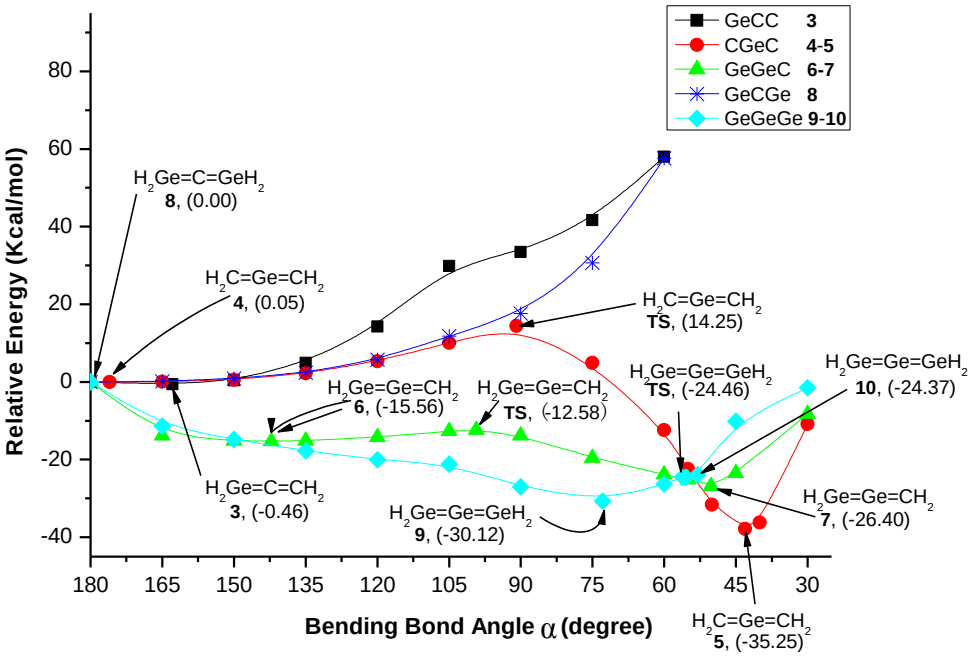

Figure 4.2 The bending PESs of five germaallene molecules at the B3LYP/6-311+G(d,p) level. [Reprinted with permission from ref. (*213*). Copyright 2004, American Chemical Society]

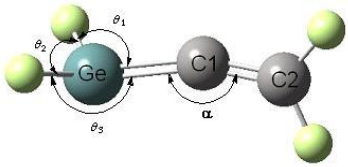

Figure 4.3 Definition of geometric parameters a) bond angle α bent at the central atom and b) the sum of bond angles around the terminal Ge_1 atoms, $\Sigma\theta$, which measures the degree of pyramidalization at the terminal atom, taking 1-germaallene as an example. [Reprinted with permission from ref. (*213*). Copyright 2004, American Chemical Society]

Table 4.2 The NBO occupancies of orbitals and Wiberg bond indices (WBI) in germaallenes and cyclic isomers **3-10**[a, b]. [Reprinted with permission from ref. (*213*). Copyright 2004, American Chemical Society]

$H_2X=Y=ZH_2$	occup. σ_{X-Y}	occup. π_{X-Y}	π_{X-Y} bond pattern	WBI (X-Y)	occup. σ_{Y-Z}	occup. π_{Y-Z}	π_{Y-Z} bond pattern	WBI (Y-Z)	occup. σ_{X-Y}	σ_{X-Y} bond pattern	WBI (X-Z)
$GeH_2=C=CH_2$ **3**	1.98	1.93	$s^{0.08}p\text{-}s^{0.02}p$	1.71	1.99	1.98	p-p	2.08	-	-	-
$CH_2=Ge=CH_2$ **4**	1.97	1.99	p-p	1.74	1.97	1.99	p-p	1.74	-	-	-
(cyclic) **5**	1.95	-	$s^{0.14}p\text{-}s^{0.06}p^c$	0.82	1.95	-	$s^{0.14}p\text{-}s^{0.06}p^c$	0.82	1.99	$sp^{2.24}\text{-}sp^{2.24}$	1.10
$GeH_2=Ge=CH_2$ **6**	1.82	1.82	$s^{0.21}p\text{-}s^{0.22}p$	1.42	1.97	1.99	p-p	1.73	-	-	-
(cyclic) **7**	1.96	-	$s^{0.24}p\text{-}s^{0.04}p^c$	0.92	1.98	-	$s^{0.07}p\text{-}s^{0.22}p^c$	0.80	1.99	$s^{0.24}p\text{-}sp^{2.97}$	0.90
$GeH_2=C=GeH_2$ **8**	1.98	1.96	p-p	1.75	1.98	1.96	p-p	1.75	-	-	-
$GeH_2=Ge=GeH_2$ **9**	1.93	-[d]	$sp^{1.62}\text{-}s^{0.06}p^c$	1.30	1.93	-[d]	$sp^{1.62}\text{-}s^{0.06}p^c$	1.30	-	-[e]	0.56
(cyclic) **10**	1.96	-	$sp^{4.67}\text{-}s^{0.05}p^c$	0.94	1.96	-	$sp^{4.67}\text{-}s^{0.05}p^c$	0.94	1.97	$sp^{3.55}\text{-}sp^{3.55}$	1.01

[a] Atom numbering is given in Figure 4.1. [b] From the B3LYP NBO analysis. [c] The bonding pattern of σ_{X-Y} bond between terminal and central Ge atom in germaallenes and their cyclic isomers. [d] There is a *p-p* partial overlapping. [e] The partial overlapping of *p* orbitals of two terminal Ge atoms.

For 2-germaallene **4**, the WBI of two Ge=C bonds is estimated to be 1.743, close to 2, indicating a relatively intact Ge=C double bond. NPA analysis on 2-germaallene **4** indicates that it has a normal σ bond and a normal π bond between the Ge and C atoms. The NPA results show that the *p* orbitals of the $\pi_{C=Ge}$ bond are almost perpendicular to the C-Ge bond, whose bending angles are 91.0° and 91.4°, respectively (see Figure 4.4(b)). The bond length, NPA occupancy (1.99) and WBI value (1.10, see Table 4.2) between the C_1 and C_2 atoms show that there is a stable C-C single bond in germacyclopropylidene **5**. The C_1-C_2 σ bond is located almost in the GeCC ring plane. There is a full *s* orbital (occupancy = 2.00) and an empty 4*p* orbital (0.02) on Ge atom. The empty 4*p* orbital on Ge does not interact with the terminal C atom as it is strictly perpendicular to the ring plane (*213*).

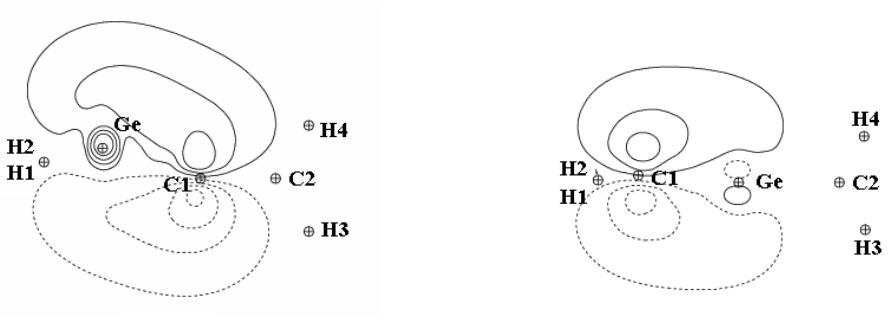

(a) (b)

Figure 4.4 The NBO contour figure of the $\pi_{Ge=C1}$ bond of monogermaallene: (a) 1-germaallene **3**, (b) 2-germaallene **4**. [Reprinted with permission from ref. (*213*). Copyright 2004, American Chemical Society]

4.2.2 Digermaallenes

The linear 1,2-digermaallene is the secondary stationary point on its bending PES. Along the bending PES of 1,2-digermaallene, the minima (1,2-digermaallene **6**, C_s symmetry and its cyclic isomer **7**, C_s symmetry) are located at α = 142.2° and 50.2°, respectively. The 1,2-digermaallene **6** and digermacyclopropylidene **7** are more stable than the linear 1,2-digermaallene by 15.56 and 26.40 kcal/mol, respectively (see Table 4.1). However, the cyclization energy barrier from 1,2-digermaallene **6** to its cyclic isomer **7** has a height of only 2.98 kcal/mol. This implies that the 1,2-digermaallene **6** is not dynamically stable. The bending PES of 1,3-digermaallene **8** has only a stable linear structure with α = 180.0° (D_{2d} symmetry) and its energy gradually increases with a decrease of the α angle (see Figure 4.2) (*213*).

1,2-Digermaallene **6** is strongly bent at the central Ge_1 atom and the $\alpha(Ge_2Ge_1C)$ angle of optimized 1,2-digermaallene **6** changes in a range from 137.3° to 153.8° depending on different computational methods (see Appendix A). The 1,2-digermaallene **6** is pyramidalized at the terminal Ge_2 atom ($\Sigma\theta$ = 312.6°). For its cyclic isomer **7**, the terminal Ge_2 and C atoms are bonded by Ge-C single bond of 1.969 Å (*213*).

Highly-symmetric 1,3-digermaallene **8** (C_{2v}) adopts a classic allenic-type structure for all the computational methods: the Ge_1CGe_2 skeleton of 1,3-digermaallene is linear and the two GeH_2 groups favor the same planar structure. It is also worth noting that the Ge=C bond (1.754 Å) is shorter in length than the normal Ge=C double bond by 0.025 Å (*213*).

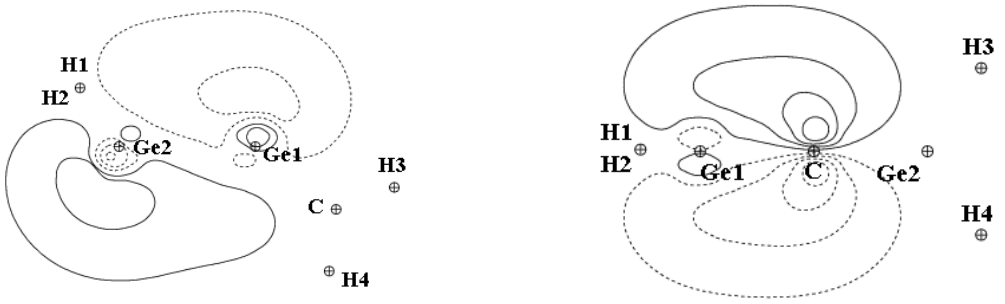

(a) (b)

Figure 4.5 The NBO contour figure of digermaallene: (a) $\pi_{Ge1=Ge2}$ bond of 1,2-digermaallen **6**, (b) $\pi_{Ge1=C}$ bond of 1,3-digermaallene **8**. [Reprinted with permission from ref. (*213*). Copyright 2004, American Chemical Society]

The WBI of the Ge_1=Ge_2 bond of 1,2-digermaallene **6** is only 1.422 (see Table 4.2), which implies that this is not the classical σ and π bonding between Ge_1 and Ge_2. The central Ge_1 atom adopts a nonclassical *sp* hybridization, whose hybrid orbital includes more *p*-character (62.5%) than monogermaallene (almost 50.0%). The π bond between two Ge atoms, occupied by 1.825 electrons, is composed of two impure *p* orbitals, $s^{0.21}p$-$s^{0.22}p$. The increased s-character in the $\pi_{Ge1\text{-}Ge2}$ bond of 1,2-digermaallene **6** hybridized the two *p* orbitals: hence, they are bent away from the Ge_1-Ge_2 internuclear axis with angles of 107.4° and 119.4°, respectively. This makes the electron cloud of the $\pi_{Ge1=Ge2}$ orbital strongly prefer one side (see Figure 4.5(a)) (*213*).

The WBI value of the Ge=C bond of 1,3-digermaallene **8** is 1.746, close to 2. The NPA analysis shows that the Ge=C bond of 1,3-digermaallene **8** is an allenic-type double

bond: these are the classical σ and π bonds between terminal Ge and central C atoms (1.984 and 1.957 electrons) and the central C atom adopts a classical sp hybridization (see Figure 4.5(b)). The bonding character of digermacyclopropylidene **7** is similar to that in germacyclopropylidene **5** (*213*).

The considerably different geometries between 1,2-digermaallene **6** and 1,3-digermaallene **8** can be rationalized by their deviation in the sum of singlet-triplet excitation energy ($\Sigma\Delta E_{S\rightarrow T}$) of fragments and the double bond energy ($E_{\sigma+\pi}$). Our B3LYP calculations found that 1,3-digermaallene's fragments (H_2Ge: + :$CGeH_2$) had a relatively lower $\Sigma\Delta E_{S\rightarrow T}$ value (41.66 kcal/mol) compared to the bond energy ($E_{\sigma+\pi}$ = 87.08 kcal/mol). On the basis of Trinquier and Malrieu's studies (*215-218*), those fragments interacted in their triplet states and thus classical planar double bonds are formed with the whole molecule adopting the classical allenic geometry. In contrast, the sum of singlet-triplet excitation energy ($\Sigma\Delta E_{S\rightarrow T}$) of 1,2-digermaallene's fragments (H_2Ge: + :$GeCH_2$) had the highest values in germaallenes (86.34 kcal/mol) and bond energy of 1,2-digermaallene is very low ($E_{\sigma+\pi}$ = 22.97 kcal/mol). Bond energy of 1,2-digermaallene cannot offset the energetic cost of the singlet→triplet state and the fragments interact by taking the lone pair of one fragment (donor) and filling into an empty *p* orbital of another fragment (acceptor). The *trans*-bent Ge=C double bonds are consequently formed and the molecular structure is deeply bent at the central atom (*213*).

4.2.3 Trigermaallene

The linear trigermaallene structure is the second-order saddle point of the bending PES and it has two minima, significantly bent C_s structure **9** and cyclic C_{2v} structure **10** (see Figure 4.1), which are more stable than the linear trigermaallene by 30.12 and 24.37 kcal/mol, respectively (the C_s and cyclic C_{2v} minima of trisilaallene lie 20.6 and 23.3 kcal/mol below its linear structure at the B3LYP/6-31G(d,p)) level (*200*). The

trigermacyclopropylidene **10** is kinetically unstable and it can be easily transformed to the C_s trigermaallene **9** through a ring-opening process with a very low barrier, i.e., 0.06 kcal/mol at the B3LYP/6-311+G(d,p) level (MP2/6-311+G(d,p): 0.26 kcal/mol; CCSD/6-311+G(d,p): 0.49 kcal/mol). This is consistent with the low ring-opening barrier of 0.02 kcal/mol at the B3LYP/6-31G(d,p) level for trisilaallene (*200*).

The C_{2v} trigermacyclopropylidene **10** has a cyclic structure: it is highly bent at the central Ge atom with α = 55.4° and the distance between terminal Ge atoms (2.404 Å) is slightly shorter than normal Ge-Ge single bond of digermane (2.444 Å). The WBI values of the Ge_1-Ge_2 (Ge_1-Ge_3) and Ge_2-Ge_3 bonds of trigermacyclopropylidene **10** are 0.94 and 1.01, respectively (see Table 4.2), very close to 1. The NBO analysis on trigermacyclopropylidene **10** indicates that its bonding character is similar to other cyclic germaallenes: there is an s orbital with lone-pair electrons (2.00) and an empty *p* orbital (0.02), which is strictly perpendicular to the ring plane (see 4.6(a)) (*213*).

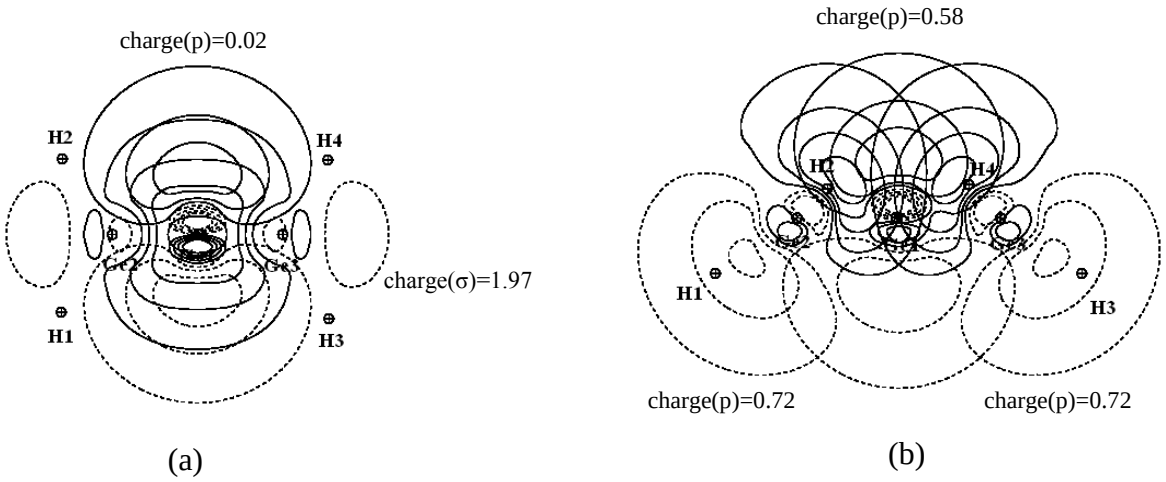

Figure 4.6 The NBO contour figure of trigermaallene **9**: (a) σ bond between terminal Ge atoms and the empty *p* orbital of the central Ge atom; (b) *p*-*p* partially overlapping between the two terminal Ge atoms and its interaction with the *p* orbital of the central Ge atom. [Reprinted with permission from ref. (*213*). Copyright 2004, American Chemical Society]

Although the C_s trigermaallene **9** also adopts a more acute $\alpha(Ge_1Ge_2Ge_3)$ bond angle of 72.9° and a shorter distance between the two terminal Ge atoms (2.848 Å), it is not a real cyclic molecule. The WBI bond index between the Ge_2 and Ge_3 atoms (0.56) in trigermaallene **9** is less than its cyclic isomer **10** and thus there is only a partial interaction. The NPA analysis shows that the partial bond between the two terminal Ge atoms come from the partial overlapping of their p orbitals, which rotate the same degree in the opposite direction to become partially head-to-head (see Figure 4.6(a)). The rotation causes the two Ge-H bonds from a different terminal Ge atom to become coplanar and trigermaallene **9** adopts a C_s molecular structure (see Figure 4.1) (*213*).

It is interesting that the central Ge atom does not adopt the hybridization, like other germaallenes, and its two *p* orbitals interact with two terminal Ge atoms by σ bonding (see Table 4.2). For the other two valence orbitals of the central Ge atom, one is an *s* orbital occupied by a lone-pair electron (1.94) and another is a *p* orbital (0.58), which is perpendicular to the ring plane. Because the two interacting *p* orbitals on the terminal Ge atoms are not in the plane of the ring (different from trigermacyclopropylidene **10**, see Figure 4.6), the p orbital on the central Ge atom can interact partially with them. The three *p* orbitals include 0.72 x 2 + 0.58 = 2.02 electrons. The WBI between the Ge_1 and Ge_2 atoms (1.299) and the optimized Ge_1=Ge_2 bond length (2.398 Å), which is between the normal single Ge-Ge bond (2.444 Å) and double Ge=Ge bond (2.305 Å), support this analysis. The interaction is similar to trisilaallene (*199-200*) and is beyond the classical valence bond theory (*213*).

The optimized structure of trigermaallene **9** (C_s) deviates from its crystal structure (*206*), for example, trigermaallenic crystal structure has a considerably larger $\alpha(Ge_1Ge_2Ge_3)$ bond angle (122.61°) compared to the DFT optimized geometry (72.9°). The difference comes from the strong steric effect of bulky substituents attached to the terminal Ge atoms in the crystal structure (*196*), which offsets the partial interaction between the terminal Ge

atoms (*213*).

For the central Ge atom, the $Ge_1Ge_2Ge_3$ bond angle of α = 72.9° is much smaller than supposedly right-angle structure (not the sp hybridization). This is due to the weak interaction of the two terminal Ge atoms. When we increase the steric repulsion between the two terminal Ge atoms by replacing the two H atoms with methyl groups, the $\alpha(Ge_2Ge_1Ge_3)$ bond angle of CH_3HGe-Ge-$GeHCH_3$ increases to 76.0°. Replacing all H atoms with methyl groups, the $\alpha(Ge_2Ge_1Ge_3)$ bond angle of $(CH_3)_2Ge$-Ge-$Ge(CH_3)_2$ further increases to 88.9°, close to the expected right angle between two *p* orbitals (see Scheme 1(a)). However, the steric repulsion between methyl groups becomes too strong so that the C_s tetramethyltrigermaallene is unstable (one imaginary eigenvalue: 20.1 cm^{-1}). This will deform to the C_2 zwitterionic structure with the $\alpha(Ge_2Ge_1Ge_3)$ of 91.1° (at B3LYP/6-31+G(d,p), $\alpha(Ge_2Ge_1Ge_3)$ = 87.0° (*206*), see Scheme 1(b)), which is 4.42 kcal/mol lower in energy compared to the C_s tetramethyltrigermaallene (at B3LYP/6-31+G(d,p), 8.4 kcal/mol) (*206*). The larger $\alpha(Ge_2Ge_1Ge_3)$ bond angle can be expected with the bulky alkyl substituents, as observed in the structure of **2**, where it has severe steric strain (*213*).

Scheme 1

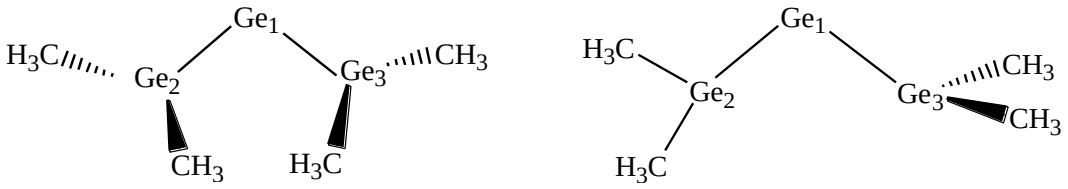

(a) $(CH_3)_2GeGeGe(CH_3)_2$, C_s (b) $(CH_3)_2GeGeGe(CH_3)_2$, C_2

4.3 Hyperconjugation of Stable Germaallenes

Because the $\pi_{M1=M2}$ bonds and σ_{M3-H} bonds of germaallenes (**3**, **4**, **6**, **8**, **9**) are close to (or lie at) the common plane, hyperconjugation interactions exist between the $\pi_{M1=M2}$ and σ_{M3-H} bonds ($\pi \rightarrow \sigma^*$ and $\sigma \rightarrow \pi^*$, see Figure 4.7). To study and compare the strength of the

hyperconjugation, we divide stable germaallenes (**3**, **4**, **6**, **8**) into two groups according to the number of germanium atoms, monogermaallene and digermaallene groups. We directly estimate the strength of the hyperconjugation interaction based on the NBO donor-acceptor interaction stabilization energies. This can also be derived by the energy decomposition analysis (EDA), which gives an exact direct estimate of intrinsic conjugative and hyperconjugative stability (*219-220*).

The NBO donor-acceptor interaction stabilization energies are calculated on the foundation of a Lewis-like localized structure. We present the classical hyperconjugation concepts by a refinement of NBO second-order perturbation analysis (*221*). For a hyperconjugation network including a M_1-M_2 π bond and a common-plane (close to the coplanar) M_3-H σ bond as shown:

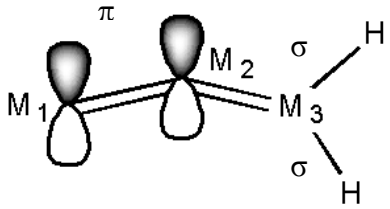

the molecular orbital can be pictured using the refined idealized Lewis structures by NBO donor-acceptor interaction of $\pi \rightarrow \sigma^*$ and $\sigma \rightarrow \pi^*$ (see Figure 4.7). According to the perturbation theory, the NBO second-order perturbation stabilization energy could be estimated as

$$\Delta E_1(\pi \rightarrow \sigma^*) = -2\frac{\langle \pi | \hat{F} | \sigma^* \rangle^2}{\Delta\varepsilon_1} \tag{4.1}$$

and

$$\Delta E_2(\sigma \rightarrow \pi^*) = -2\frac{\langle \sigma | \hat{F} | \pi^* \rangle^2}{\Delta\varepsilon_2} \tag{4.2}$$

where $\Delta\varepsilon_1 = \langle \sigma^* | \hat{F} | \sigma^* \rangle - \langle \pi | \hat{F} | \pi \rangle$ and $\Delta\varepsilon_2 = \langle \pi^* | \hat{F} | \pi^* \rangle - \langle \sigma | \hat{F} | \sigma \rangle$ are the energy differences of interacting NBOs (*221*). Our pervious works (*211-212*) have indicated that the NBO second-order perturbation stabilization energy is a good criterion to estimate the

conjugation strength for the delocalization network, although it cannot be used for estimating absolute resonance energies (*213*).

The NBO second-order perturbation stabilization energies ($\pi\rightarrow\sigma^*$ and $\sigma\rightarrow\pi^*$) of stable germaallenes (**3**, **4**, **6**, **8**) are given in Table 4.3. The π–σ hyperconjugation strength of every germaallene is indicated in terms of the total NBO second-order perturbation stabilization energies (see Table 4.3). Because the $\pi_{M1=M2}$ orbital always interacts with two $\sigma_{M3\text{-}H}$ orbitals, we provide the sum of their values in Table 4.3 ($\Delta E_1(\pi\rightarrow\sigma^*)$ or $\Delta E_2(\sigma\rightarrow\pi^*)$).

Table 4.3 The NBO second-order perturbation stabilization energies ($\pi\rightarrow\sigma^*$ and $\sigma\rightarrow\pi^*$) of 1-germaallene **3**, 2-germaallene **4**, 1,2-digermaallene **6** and 1,3-digermaallene **8** ($M_1H_2=M_2=M_3H_2$) on the hyperconjugation effect involving the $\pi_{M1=M2}$ and $\sigma_{M3\text{-}H}$ bonds (or the $\pi_{M3=M2}$ and $\sigma_{M1\text{-}H}$ bonds). [Reprinted with permission from ref. (*213*). Copyright 2004, American Chemical Society]

Germaallene	π	σ	ΔE_1[a] [$\pi\rightarrow\sigma^*$]	ΔE_2[a] [$\sigma\rightarrow\pi^*$]	**Sum A**[b]	σ	π	ΔE_1[a] [$\pi\rightarrow\sigma^*$]	ΔE_2[a] [$\sigma\rightarrow\pi^*$]	**Sum B**	**Total**
GeH_2=C=CH_2 **3**	Ge=C	C-H	14.70	13.54	28.24	H-Ge	C=C	5.12	5.22	10.34	38.58
CH_2=Ge=CH_2 **4**	C=Ge	C-H	4.57	3.93	8.50	H-C	Ge=C	4.57	3.93	8.50	17.00
GeH_2=Ge=CH_2 **6**	Ge=Ge	C-H	4.06	3.29	7.35	H-Ge	Ge=C	2.36	2.36	4.72	12.07
GeH_2=C=GeH_2 **8**	Ge=C	Ge-H	10.32	3.98	14.30	H-Ge	C=Ge	10.32	3.98	14.30	28.60
GeH_2=Ge=GeH_2 **9**	Ge=Ge	Ge-H	-[d]	-[d]	-	H-Ge	Ge=Ge	-[d]	-[d]	-	-

[a] The sum of NBO second-order perturbation stabilization energies from interactions between two M-H σ bonds and the π bond, in kcal/mol. [b] The sum A (or sum B) values = $\Delta E_1(\pi\rightarrow\sigma^*)$ + $\Delta E_2(\sigma\rightarrow\pi^*)$, in kcal/mol. [c] The total NBO second-order perturbation stabilization energies = sum A + sum B, in kcal/mol. [d] There is no formal π bond between the central and terminal Ge atoms.

For mono- and digermaallene groups the total NBO second-order perturbation stabilization energies follow the trend 1-germaallene **3** (38.58 kcal/mol) > 2-germaallene **4** (17.00 kcal/mol), 1,3-digermaallene **8** (28.60 kcal/mol) > 1,2-digermaallene **6** (12.07 kcal/mol). Our NBO second-order perturbation analysis indicates that there is no formal π bond between the central and terminal germanium atoms of trigermaallene **9** (see above) and there should be no π–σ hyperconjugation interaction for trigermaallene **9** (*213*).

Table 4.4 The polarization coefficients of the NBO $\pi_{M1=M2}$, σ^*_{M3-H}, $\pi_{M2=M3}$ and σ^*_{M1-H} bonds in $M_1H_2=M_2=M_3H_2$ molecules (M = Ge or C) and the distance between M_2 and M_3 atoms (or between M_1 and M_2 atoms) at the B3LYP/6-311+G(d,p) level. [Reprinted with permission from ref. (*213*). Copyright 2004, American Chemical Society]

$H_2M_1=M_2=M_3H_2$	$\pi(M_1=M_2)$		$\sigma^*(M_3-H)$		$d(M_2-M_3)^a$	$\pi(M_2=M_3)$		$\sigma^*(M_1-H)$		$d(M_1-M_2)^a$
	M_1	M_2	M_3	H		M_2	M_3	M_1	H	
$H_2Ge=C=CH_2$ **3**	0689[b]	0.727[b]	0.779[c]	0.627[c]	1.307	0.711[b]	0.703[b]	0.670[c]	0.742[c]	1.789
$H_2C=Ge=CH_2$ **4**	0.834	0.552	0.785	0.619	1.761	0.552	0.834	0.785	0.619	1.761
$H_2Ge=Ge=CH_2$ **6**	0.768	0.641	0.783	0.620	1.784	0.597	0.802	0.664	0.748	2.380
$H_2Ge=C=GeH_2$ **8**	0.582	0.813	0.666	0.746	1.754	0.813	0.582	0.666	0.746	1.754
$H_2Ge=Ge=GeH_2$ **9**	-	-	-	-	-	-	-	-	-	-

[a] The M_2-M_3 or M_2-M_3 bond length, in Å. [b] The polarization coefficients of the NBO $\pi_{M1=M2}$ (or $\pi_{M2=M3}$) orbital on M_1 and M_2 (M_2 and M_3) atoms. [c] The polarization coefficients of the NBO σ^*_{M-H} orbital on M and H atoms.

Similar to π-conjugation in silabutadiene and germabutadiene (*211-212*), the total NBO second-order perturbation stabilization energies of π-σ hyperconjugation for germaallenes are found to be very sensitive towards the orientation of $\pi_{M1=M2}$ bond (M = Ge, C), and the distance between M_2 and M_3 atoms. For example, 1,2-digermaallene **6** and 1,3-digermaallene

8 have similar Ge-C bond lengths (1.784 and 1.754 Å, see Table 4.4) but higher polarization coefficients of the $\pi_{Ge=Ge}$ ($\pi_{Ge=C}$). 1,3-digermaallene **8** (central C atom polarization coefficient = 0.813) obviously has a stronger hyperconjugation ($\Delta E_1(\pi \rightarrow \sigma^*)$ = 10.32 kcal/mol) than 1,2-digermaallene **6** (polarization coefficient = 0.641, $\Delta E_1(\pi \rightarrow \sigma^*)$ = 4.06 kcal/mol, see Table 4.4). 2-Germaallene **4** and 1,2-digermaallene **6** have almost the same polarization coefficient at the central Ge (0.552 and 0.597) and the longer Ge=Ge bond length of 1,2-digermaallene **6** (2.380 Å) reduces the hyperconjugation strength (4.72 kcal/mol), leading it to have only a half of 2-germaallene **4**'s NBO second-order perturbation stabilization energy (8.50 kcal/mol, see Table 4.4).

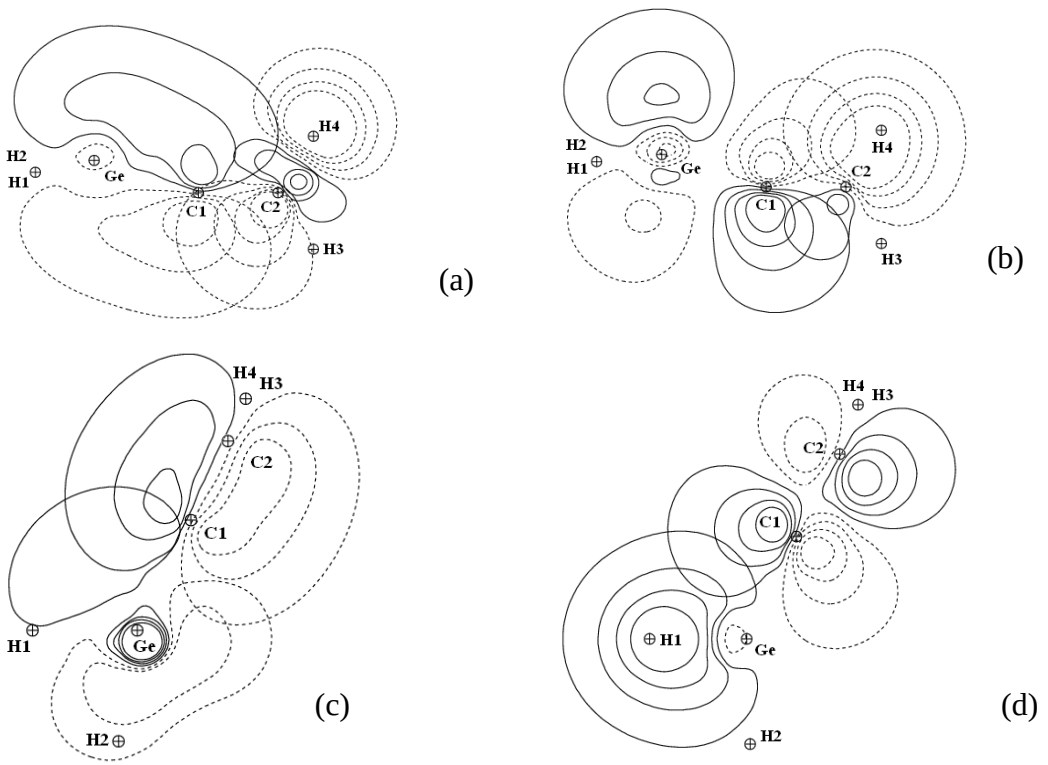

Figure 4.7 The π–σ hyperconjugative interaction of germaallenes showed in NBO contour figures (taking 1-germaallene **3** as example): (a) $\pi_{Ge=C} \rightarrow \sigma_{C=H}^*$; (b) $\sigma_{C=H} \rightarrow \pi_{Ge=C}^*$; (c) $\pi_{C=C} \rightarrow \sigma_{Ge=H}^*$; (d) $\sigma_{Ge=H} \rightarrow \pi_{C=C}^*$. [Reprinted with permission from ref. (*213*). Copyright 2004, American Chemical Society]

4.4 Stability of Germaallenes

The stabilities of the monogermaallene and digermaallene isomers follow the sequence as following: 1-germaallene **3** (0.00 kcal/mol) > 2-germaallene **4** (11.91 kcal/mol) and 1,2-digermaallene **6** (0.00 kcal/mol) > 1,3-digermaallene **8** (31.18 kcal/mol, at the B3LYP/6-311+G(d,p) level, see Table 4.1). The 1,2-digermaallene **6** is significantly more stable than 1,3-digermaallene **8** in the digermaallene group and the stability difference between 1,2-digermaallene **6** and 1,3-digermaallene **8** is considerably stronger than the difference between 1-germaallene **3** and 2-germaallene **4** (*213*).

The stability discrepancy between germaallenic isomers mainly come from the different bond order for the -M=N- (M, N = C, Ge) double bond. The bonding analysis in MH_2=NH_2 from Jacobsen and Ziegler (*222*) shows that there is a considerably decrease in the intrinsic bond strength of the M=N double bond as M and N atoms become heavier. Their DFT calculations found that the dissociation energies of MH_2=NH_2 are 176.63 and 43.02 kcal/mol, respectively. We compare the contributions of the -C=C-, -Ge=C- and -Ge=Ge- double bonds to the stability using two reactions as follows:

$$CH_2{=}CH_2 + GeH_4 \rightarrow GeH_2{=}CH_2 + CH_4 \qquad \Delta H = 10.20 \text{ kcal/mol} \quad (4.3)$$

$$GeH_2{=}GeH_2 + CH_4 \rightarrow GeH_2{=}CH_2 + GeH_4 \qquad \Delta H = 25.86 \text{ kcal/mol} \quad (4.4)$$

In fact, the eqs (4.3) and (4.4) represent the different parts after the germaallenes are broken up into two units of hetero- and mononuclear analogues of ethane. They show that the bond energies in 1-germaallene **3** and 1,2-digermaallene **6** are more stable than in 2-germaallene **4** and 1,3-digermaallene **8** by 10.20 and 25.86 kcal/mol, respectively. The relative bond energies are close to the corresponding total relative stabilities (11.91 and 31.18 kcal/mol) in monogermaallene and digermaallene groups. Thus, we come to a conclusion that the stability of germaallenes is determined primarily by the stability of the bonds that compose them. The stability sequence of the bond energies in the digermaallene group (1,2-

digermaallene > 1,3-digermaallene) is contrary to that of the hyperconjugation. As expected, it reflects that stabilization by hyperconjugation is not the main factor that determines the compound's total stability (*213*).

In summary, germaallenes, except 1,3-digermaallene, have different electronic structure and bonding from classic allene. 2-germaallene and 1,2-digermaallene molecules have more stable cyclic structure and the cyclic isomer of trigermaallene is higher in potential energetic than its strongly bent C_s structure. The natural population analysis shows that the *p*-character increases in the valence orbital of central Ge atom and the *s*-character also become more in orbitals composing of the π bond. For trigermaallene, there is a partial overlapping from two *p* orbitals on terminal Ge atoms and the central Ge atom does not adopt an orbital hybridization. The NBO second order perturbation analysis indicates that there is π-σ hyperconjugation interaction within germaallene and the strength of π-σ hyperconjugation follow the order: 1-germaallene > 1,3-digermaallene > 2-germaallene > 1,2-digermaallene.

In this chapter, different computational methods like DFT, MP2 and CCSD methods have been used successfully to understand the molecular structures and electronic properties of germaallenes which will help to carry out the current research work in Chapter 5 and 6.

Chapter 5

Theoretical Studies on Germanium Nanowires

In this Chapter, we performed density functional calculations to investigate the electronic and magnetic properties of GeNWs. Firstly, we study the water induced electrical hysteresis observed in GeNWs to understand the origin of electrical hysteresis. Secondly, we study the electronic and magnetic properties of surface defected GeNWs to design half-metallic GeNWs.

5.1 Water Induced Electrical Hysteresis in Germanium Nanowires

Recently, the electrical properties of GeNW field effect transistors (FETs) have been studied experimentally by Wang et al. (*38*). They reported a large hysteresis in electric current upon exposure to ambient air. The hysteresis is reported to be removed when the GeNWs are annealed at higher temperature, 450° C if they have not been exposed to ambient air for more than a day. It can be concluded that hysteresis in electric current observed experimentally in GeNW FETs is of two types (*38*). (a) *Reversible hysteresis*: when a GeNW FET is exposed to ambient air, it shows large hysteresis in electric current but it disappears when the GeNW FET is placed back into a vacuum chamber after a short (~10 min) exposure to air. The short exposure of the GeNW FET to air may likely lead to molecular adsorption of water that can be removed. (b) *Irreversible hysteresis*: when GeNW FET is exposed to ambient air for a longer period of time (~1 day), it shows irreversible hysteresis, i.e. the GeNW FET exhibits hysteresis after placing it back into the vacuum chamber. The amount of hysteresis depends on the exposure period to air. During long exposure, molecular adsorbed H_2O is likely to oxidize GeNW, leading to the formation of GeNW with a terminal OH group. It is know that Ge can be oxidized into GeO_2 and $Ge(OH)_4$ in water. Thus, OH passivated GeNWs (OH-GeNWs) could be responsible for the irreversible hysteresis observed. However, the origin of the electrical hysteresis in GeNW based electronic devices has not been explored in detail (*223*).

So far, surface functionalizations of GeNWs with different chemical groups like Cl, F, SH (*224-225*), alkene, alkyne and diene species (*31*) have been studied experimentally to prevent the problems of oxidation and hysteresis in electric current of GeNWs, while the structural and electronic properties of hydrogen passivated GeNWs (H-GeNWs) have also been widely studied theoretically (*226-232*). To the best of our knowledge there are no theoretical reports on OH-GeNWs. However, few theoretical works are reported on the

electronic properties and chemical potential of OH passivated silicon nanowires (OH-SiNWs). Nolan et al. (*233*) reported that the surface passivation groups like OH and NH_2 have introduced hybridization effect in silicon nanowires (SiNWs) which competed with the quantum confinement effect and resulted in band gap narrowing. The hybridization effect in OH and NH_2-SiNWs is resulted from the interaction between O/N 2*p* and Si 3*p* states in the valence band edge of NWs. Recently, Ng et al. (*234*) showed that the chemical potential of SiNWs depends on the surface passivation. The electron withdrawing effect of F increased the chemical potential, while the resonance effect of the OH group decreased the chemical potential as compared to hydrogen passivated SiNWs (*223*).

In this part, we apply DFT calculations to evaluate how the water molecule adsorption on the GeNW surface would affect its electronic properties and reveal the possible cause of electrical hysteresis in GeNW based electronic devices. We first rationalize how the OH-GeNW is formed, from which we propose the formation mechanism of OH-GeNW. Then, we evaluate in details its electronic properties such as band gap, density-of-state (DOS), formation energy and effective mass. Furthermore, by examining OH-GeNWs with various OH coverage percentages and different alignments of the OH groups on the GeNW surface, we come up with the possible causes to the origin of electrical hysteresis phenomenon observed in experiment.

5.1.1 Models

For the GeO_2 surface, it is constructed by cutting the optimized bulk GeO_2 (quartz like structure) along the (100) surface orientation. We have used two layers of the GeO_2 surface model and fixed the bottom layer while relaxing the top layer. A 10 Å vacuum slab is applied above the top layer (*223*).

For the GeNWs, they are constructed from the optimized bulk Ge by cleaving the surface with the desired diameters and growth directions. The dangling bonds are passivated by hydrogen, forming hydrogen passivated GeNWs (H-GeNWs). The axis of the nanowire is oriented along the *z*-direction of the unit cell while *x*- and *y*-directions are the vacuum. To prevent the interactions of neighbouring atoms, we keep the distance of >10 Å between the two nearest supercells (*223*).

The stoichiometries and diameters of the ⟨100⟩ and ⟨110⟩ GeNWs in their primitive cells are $Ge_{32}H_{24}$ and $Ge_{32}H_{18}$, and, 12.2 Å and 14.0 Å, respectively. We use two primitive cells to construct the nanowires for all the ⟨100⟩ and ⟨110⟩ GeNWs calculations. Since, the unit length of ⟨111⟩ GeNWs is 9.980 Å, we use one primitive cell to construct ⟨111⟩ GeNWs with stoichiometry of $Ge_{38}H_{30}$. To construct the OH passivated GeNWs (OH-GeNWs), the H atoms on the GeNWs are replaced by OH groups. We calculate the bulk Ge to evaluate the method. The optimized lattice constant of the bulk Ge using the GGA-PBE method is 5.775 Å, which is within 2 % as compared with the experimental value (*235*).

5.1.2 Formation Mechanism of OH-GeNWs

It is shown in experiment (*38*) that the surface Ge atoms are oxidized to GeO when the clean GeNWs are exposed to air. GeO adsorbs water molecules reversibly and with longer exposure GeO is oxidized to GeO_2 which strongly adsorbs water molecules. The adsorbed water molecules cannot be removed by the treatment with polymethylmathacrylate (PMMA) with baking, while the same treatment removed the adsorbed water molecules from the nanotubes and SiO_2 surfaces. To understand the phenomenon, we investigate the behaviour of water molecules adsorbed on the GeO_2 surface. We consider both molecular adsorption and dissociative chemisorption of the water molecules on the GeO_2 surface. GeO_2

surface model is shown in Figure 5.1. Adsorption energy of water molecules is calculated according to following equation –

$$E_{ads} = E_{complex} - E_{water}, \qquad (5.1)$$

where E_{ads} is the adsorption energy of the water on the surface of the GeO_2, $E_{complex}$ is the total energy of the GeO_2 surface containing water molecules, E_{water} is the total energy of the water molecules. Negative adsorption energy indicates the favourable interactions (*223*).

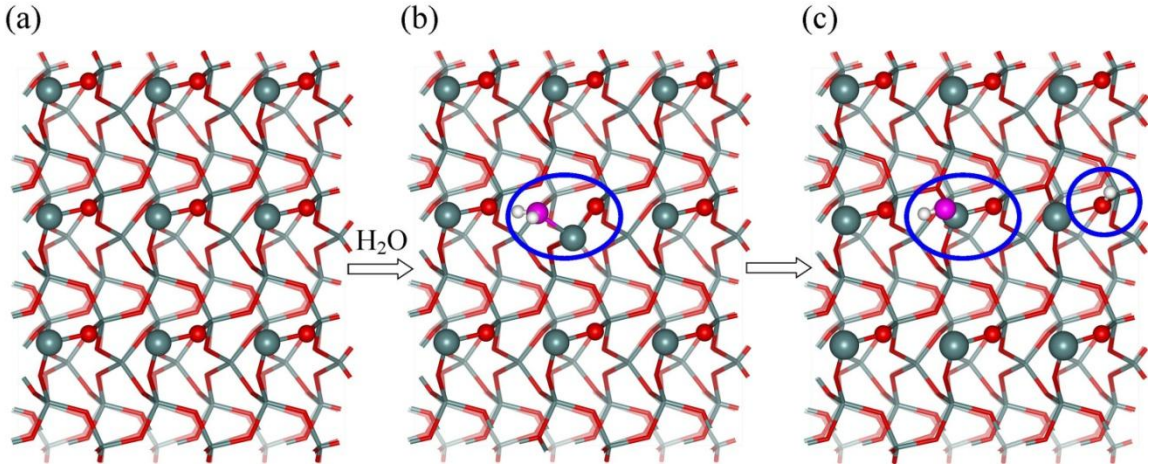

Figure 5.1 Top-view of (a) optimized structure of the ⟨100⟩-GeO_2 surface, (b) GeO_2 with molecular adsorption of water and (c) GeO_2 with dissociative chemisorption of water. Green sphere – Ge, red sphere – O, pink sphere – O from water, white sphere – H (*223*). [Reproduced by permission of the PCCP Owner Societies]

The calculated adsorption energy of water on the GeO_2 surface is listed in Table 5.1. The calculated adsorption energy for molecular adsorption of water on the GeO_2 surface is exothermic, -0.60 eV. Upon dissociation of water, one OH is adsorbed on a surface Ge atom and the dissociated H atom migrated and is bonded to a surface O with a more favourable exothermic energy of -1.79 eV as compared to molecular adsorption. Once the water molecule is dissociated, the reversible desorption of the water molecule is a highly endothermic process. Based on our results, we propose that first the water molecule adsorbed

physically on the GeNWs surface, then with time the adsorbed water molecules dissociate to OH· and H· radicals and form two OH groups on the GeO_2 surface. As a result, the OH passivated Ge surface is formed.

Table 5.1 Calculated adsorption energy (in eV) of the water molecules on the ⟨100⟩-GeO_2 surface (*223*). [Reproduced by permission of the PCCP Owner Societies]

	Adsorption energy (eV)
Molecular adsorption	-0.60
Dissociative chemisorption	-1.79

In the process of water adsorption on GeNWs, it is important to know the preferential adsorption site because later on we will show that the OH alignment would have a strong effect on the electrical hysteresis. By symmetry, the ⟨100⟩ GeNW has three different adsorption sites on the surface as shown in Figure 5.2. We find that OH substitution at adsorption site 1 has the lowest energy, indicating that it is the preferential site (see Figure 5.2).

The reason is that the Ge atom at site 1 is mono-substituted, i.e. no internal repulsive force within the site. Thus, it is more stable. However, sites 2 and 3 are on the same Ge atom, the adsorbed OH at site 2 would experience more repulsive force from the nearby OH group at site 3, and *vice versa*. As a result, this makes sites 2 and 3 the less preferential sites as compared to site 1. Consequently, the OH passivated GeNW with higher OH coverage percentage are then formed according to the energy of the adsorption site (from low to high energy sites, see Figure 5.3). Similarly, we determine the OH adsorption sequence for the ⟨110⟩ and ⟨111⟩ GeNWs (see Figures 5.2b and c).

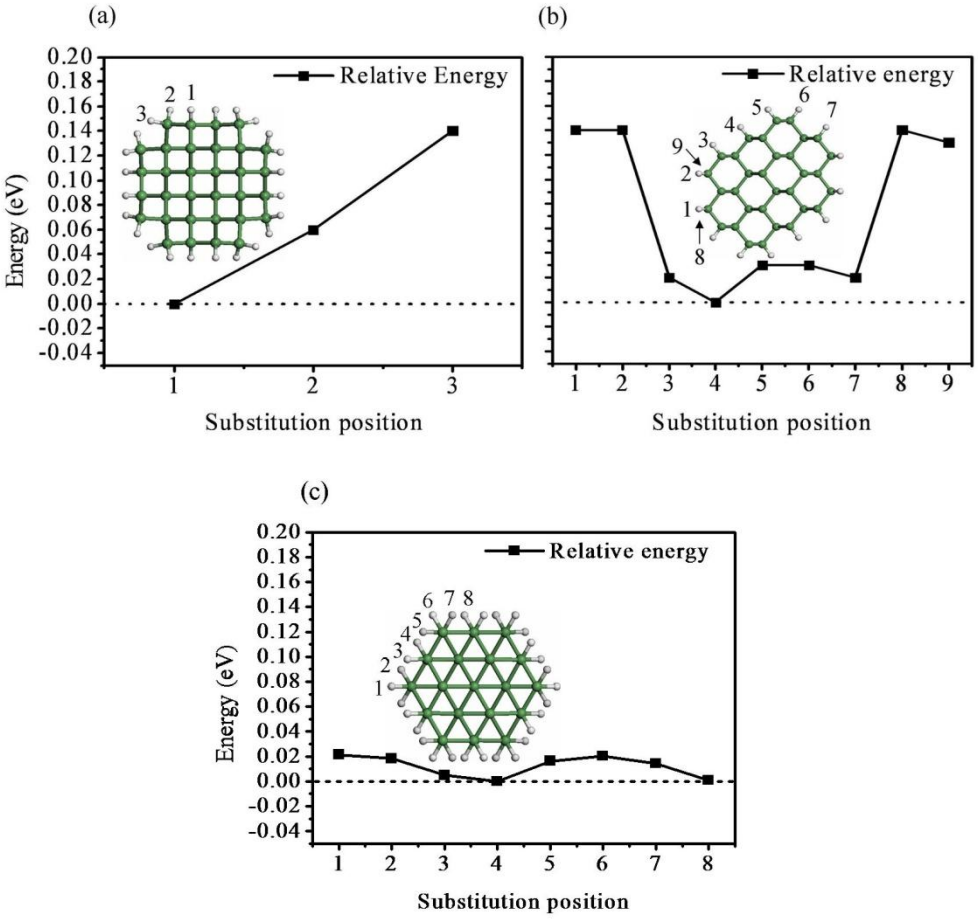

Figure 5.2 Relative energy of mono-substituted OH-GeNWs as a function of the substitution position in (a) ⟨100⟩ GeNW, (b) ⟨110⟩ GeNW and (c) ⟨111⟩ GeNW. Inset are the structures of GeNWs showing the substitution positions (*223*). [Reproduced by permission of the PCCP Owner Societies]

6.1.3 Stability and Electronic Properties of OH-GeNWs

The amount of water molecules being adsorbed on the GeNW surface is one of the main factors affecting its electrical behaviour. To investigate the effect of water adsorption on the stability of GeNWs, we calculate the formation energy E_{form} of OH-GeNWs with different OH coverage percentages using the equation, (*236*) –

$$E_{form} = E_{wires} - \sum_{i=Ge,O,H} n_i \mu_i \,, \qquad (5.2)$$

where E_{wires} is the total energy for a given nanowire, n_i and μ_i are the occurrence and chemical potential of various elements, respectively. For the chemical potential of Ge, we derive it from bulk state while for the chemical potential of O and H atoms, we derive them from O_2 and H_2 molecular states, respectively.

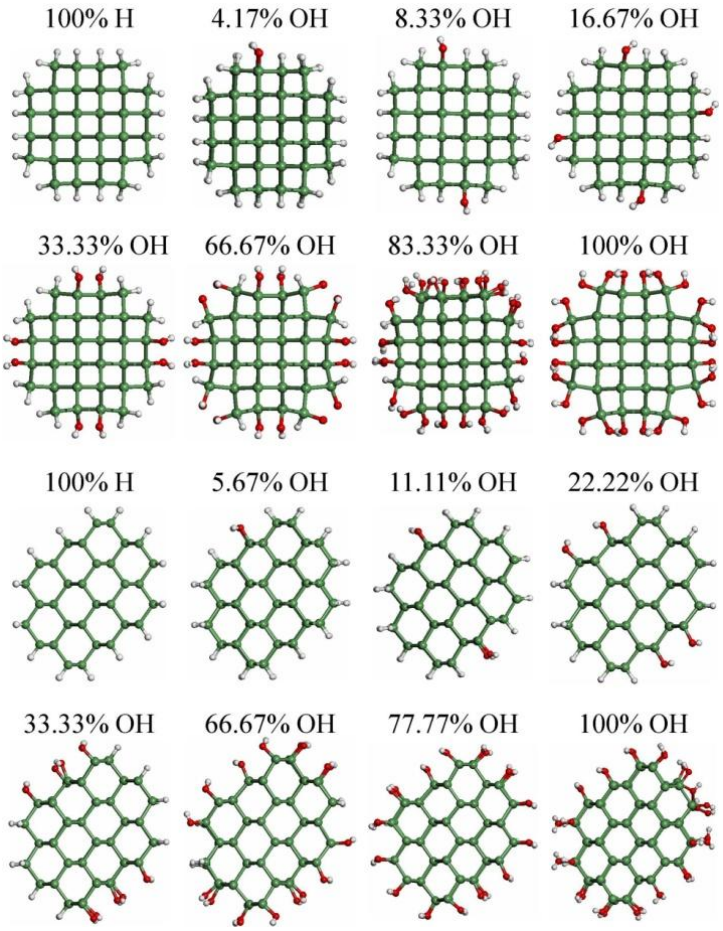

Figure 5.3 Cross-sectional view of optimized structures of ⟨100⟩ (top two rows) and ⟨110⟩ (bottom two rows) OH-GeNWs (*223*). [Reproduced by permission of the PCCP Owner Societies]

The plot of formation energy of GeNWs as the function of the OH coverage percentage is shown in Figure 5.4 and the details are listed in Table 5.2. Our results show that with the increase in the OH coverage percentage, the formation energies for both the ⟨100⟩ and ⟨110⟩ GeNWs become more negative, indicating that the formation of OH-GeNWs with

higher surface coverage percentage is more favourable. The reason can be attributed to the stronger Ge-OH bond strength. The calculated average Ge-OH bond strength in mono-substituted ⟨100⟩ OH-GeNWs is 3.92 eV, which is stronger than the calculated Ge-H bond strength of 3.11 eV in ⟨100⟩ GeNWs. Thus, the formation of Ge-OH bonds on GeNW has a stronger stabilizing effect. Moreover, for the ⟨100⟩ and ⟨110⟩ GeNWs, the formation energies of both of them show a linear relationship with OH coverage percentage.

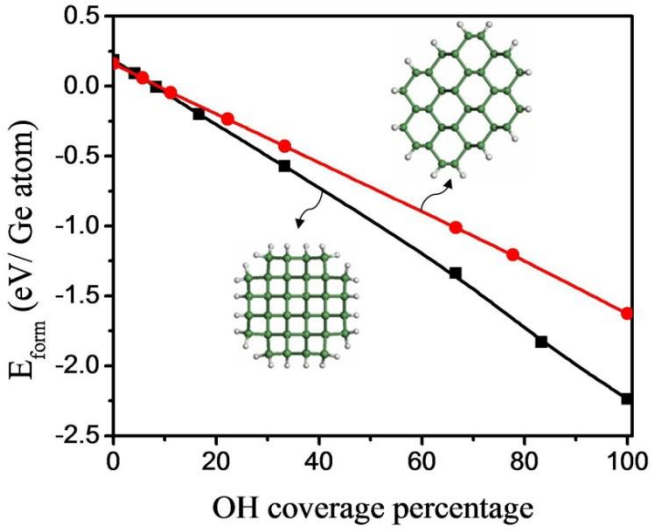

Figure 5.4 The formation energy of OH-GeNWs as a function of OH percentage coverage. Black line with squares: ⟨100⟩ OH-GeNWs; Red line with circles: ⟨110⟩ OH-GeNWs (*223*). [Reproduced by permission of the PCCP Owner Societies]

For comparison, we also calculate the formation energies of 100% OH passivated ⟨100⟩ and ⟨110⟩ silicon nanowires (OH-SiNWs) according to eqn (5.2), where the chemical potential of Si is derived from the bulk Si. The calculated formation energies are listed in Table 5.2. The formation energy of OH-SiNW, -1.98 eV, is larger than that of OH-GeNWs, indicating the formation of OH-SiNWs is energetically more favourable than OH-GeNWs.

Table 5.2 The calculated formation energy (E_{form}) and band gap (E_{gap}) of ⟨100⟩ and ⟨110⟩ OH-GeNWs (*223*). [Reproduced by permission of the PCCP Owner Societies]

⟨100⟩ OH-GeNW			⟨110⟩ OH-GeNW		
P_{SC}[a]	E_{form} (eV/ Ge atom)	E_{gap} (eV)[b]	P_{SC}[a]	E_{form} (eV/Ge atom)	E_{gap} (eV)[b]
0.00	0.19	2.05 *i*	0.00	0.16	1.05 *d*
4.17	0.09	2.02 *i*	5.67	0.06	1.13 *d*
8.33	-0.01	2.03 *d*	11.11	-0.05	1.12 *d*
16.67	-0.20	1.88 *d*	22.22	-0.23	1.09 *d*
33.33	-0.57	1.51 *d*	33.33	-0.43	1.00 *d*
66.67	-1.34	1.38 *d*	66.67	-1.01	0.78 *d*
83.33	-1.83	1.14 *d*	77.78	-1.21	0.84 *d*
100.00	-2.24	1.05 *d*	100.00	-1.63	0.52 *d*
100.00[c]	-2.77	1.79 *d*	100.00[c]	-1.98	1.00 *d*

[a] P_{SC} is the surface OH coverage percentage. [b] *i* indicates indirect and *d* indicates direct. [c] OH-SiNWs with 100 % surface OH coverage.

For the electronic structures of OH-GeNWs, the band structures of the OH-GeNWs are shown in Figure 5.5. It is shown that the higher the percentage of OH passivation, the smaller the band gap for the GeNW. The band gaps of ⟨100⟩ OH-GeNWs with various OH coverage percentages ranged from 2.02 to 1.05 eV while for the ⟨110⟩ OH-GeNWs, 1.13 to 0.52 eV. The reduction of the band gap may be explained by the increase of *s*- and *p*-occupancy of the highest occupied molecular orbital (HOMO) and the lowest unoccupied molecular orbital (LUMO) with the increase of the surface OH coverage percentage (see Table 5.3).

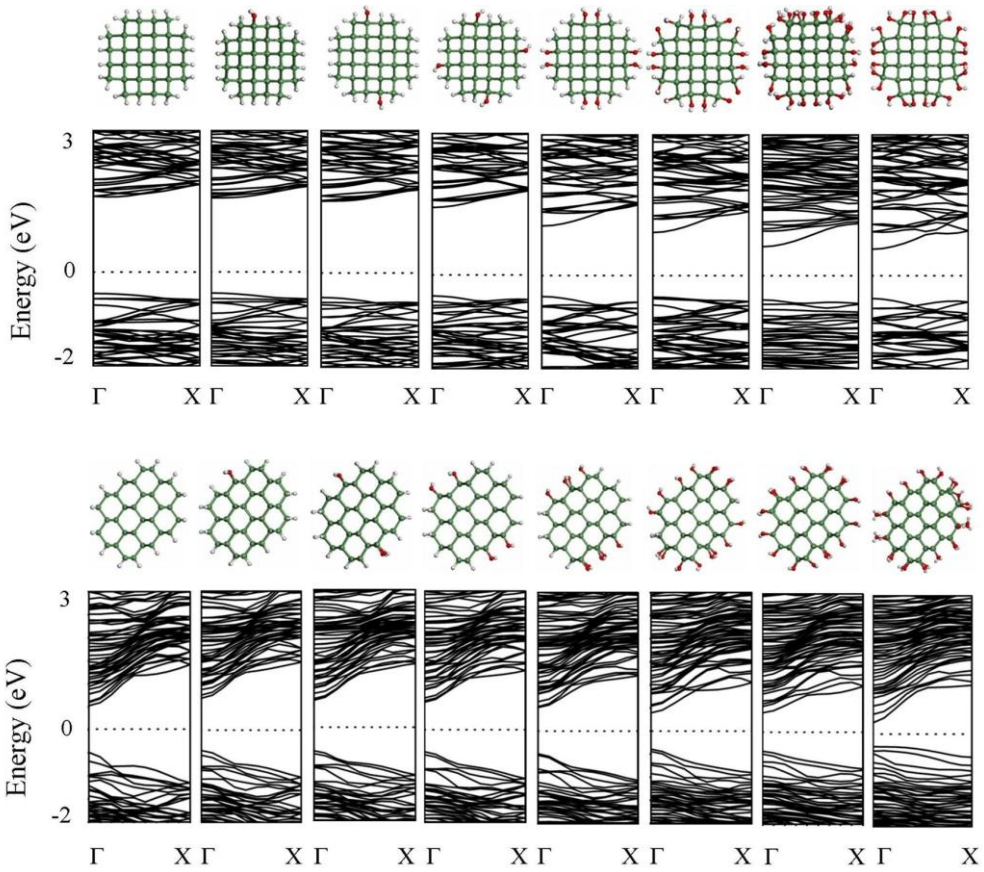

Figure 5.5 The band structures of ⟨100⟩ (top figures) and ⟨110⟩ (bottom figures) OH-GeNWs. The Fermi level is set as the reference energy and denoted by dotted lines (*223*). [Reproduced by permission of the PCCP Owner Societies]

It is shown that with the increase of OH surface coverage percentage, the *p*-occupancy of HOMO is increased. It indicates that the substitution of H with OH in GeNWs forms Ge-O bonds, which increases the *p*-electrons in the system and can result in band gap narrowing. Moreover, the density-of-states show that the reduction of band gap for the ⟨100⟩ GeNW with OH passivation is due to generation of the new electronic states near Fermi level, while the OH group has less effect on electronic states near Fermi level in the ⟨110⟩ GeNW (see Appendix B). For comparison, we calculate the band gaps of 100% ⟨100⟩ and ⟨110⟩ OH-SiNWs and find that they are larger than OH-GeNWs (see Table 5.2).

Table 5.3 *s*- and *p*-occupancy of HOMO and LUMO of ⟨100⟩ and ⟨110⟩ OH-GeNWs (*223*). [Reproduced by permission of the PCCP Owner Societies]

⟨100⟩ OH-GeNW				⟨110⟩ OH-GeNW			
P_{SC}[a]	s_{LUMO}	p_{LUMO}	p_{HOMO}	P_{SC}[a]	s_{LUMO}	p_{LUMO}	p_{HOMO}
0.00	0.291	0.147	0.447	0.00	0.309	0.143	0.469
4.17	0.288	0.155	0.446	5.67	0.307	0.144	0.465
8.33	0.475	0.112	0.451	11.11	0.306	0.145	0.465
16.67	0.483	0.115	0.451	22.22	0.304	0.148	0.471
33.33	0.512	0.129	0.481	33.33	0.413	0.154	0.477
66.67	0.513	0.165	0.495	66.67	0.473	0.157	0.505
83.33	0.518	0.192	0.499	77.78	0.476	0.166	0.408
100.00	0.529	0.204	0.518	100.00	0.493	0.191	0.498

[a] P_{SC} is the surface OH coverage percentage.

5.1.4 Electrical Hysteresis in OH-GeNWs

We show up to here that (a) water would be adsorbed on GeNW, forming OH-GeNWs, and (b) the amount of water molecules being absorbed is one of the critical factors that affecting the stability and band gap of GeNWs. In other words, it would affect the electrical properties as well. We reveal below how the water adsorption can cause the electrical hysteresis phenomenon.

Since, the electrical conductivity of any material is inversely proportional to the effective mass of electrons and holes, we calculate the effective mass of electrons of OH-GeNWs. We calculate the effective masses from the band structures. First we calculate the energy dispersion near Γ point. We use the wave vector from -0.1 to 0.1. Then, the curve of energy dispersion near Γ point is fitted with a second order polynomial $E = C_1 k^2 + C_2 k + C_3$,

where k is the wave vector and C_1, C_2 and C_3 are the coefficients. Then we calculate the effective mass of electrons using the formula (*91*) $m^* = \left(\frac{h}{2\pi}\right)^2 / \left(\frac{d^2E}{dk^2}\right)$, where h is the Plank's constant.

Calculated effective electron mass of OH-GeNWs is plotted as the function of OH coverage percentage as shown in Figure 5.6a.

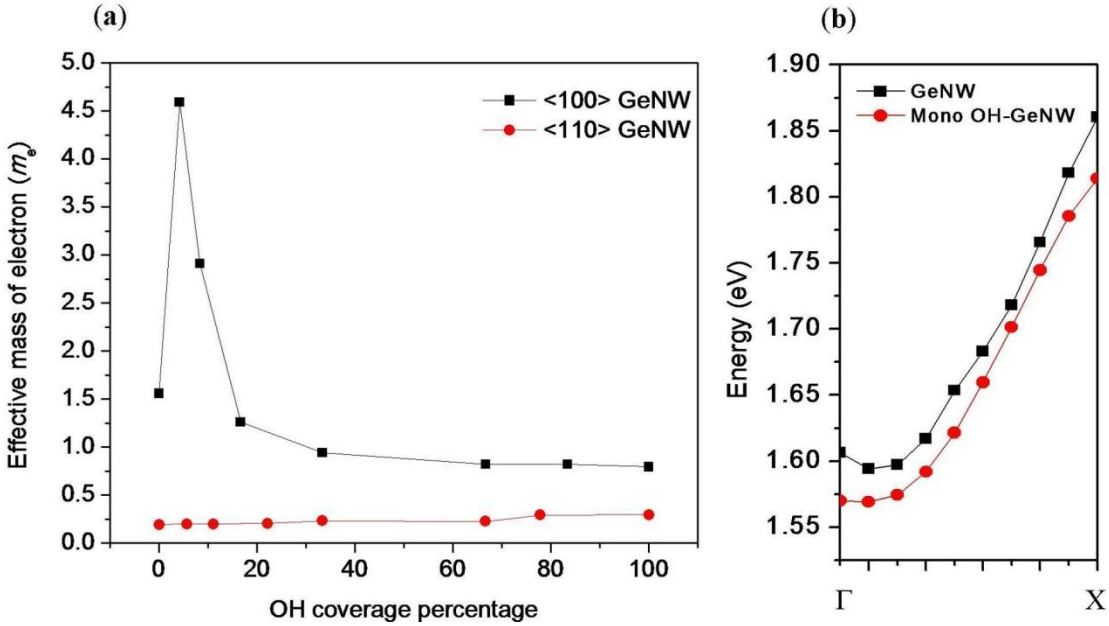

Figure 5.6 (a) Effective mass of electron (m_e*) of ⟨100⟩ and ⟨110⟩ OH-GeNW as the function of the OH coverage percentage on the surface of GeNWs. (b) A plot of the conduction band of ⟨100⟩ the GeNW and the mono-substituted ⟨100⟩ OH-GeNW (4.17% surface coverage) near the Fermi level (*223*). [Reproduced by permission of the PCCP Owner Societies]

The effective electron mass of the ⟨100⟩ GeNW increases with mono-substitution of GeNW with OH. To understand the rapid increase of the effective electron mass for mono-substituted GeNW, we plot the conduction band near the Fermi level of the ⟨100⟩ H-GeNW and the mono-substituted GeNW with OH as shown in Figure 5.6b. The energy dispersion around the Γ point shows that OH substitution in GeNW almost causes the change of the

nature of the band gap of the ⟨100⟩ GeNW from indirect to direct, which results in the increased effective mass for mono-substituted GeNWs with OH. Once the nature of the band gap of the ⟨100⟩ OH-GeNW becomes direct, the effective electron mass decreases with the increase in the OH coverage percentage. In contrast, the effective electron mass in the ⟨110⟩ OH-GeNWs increases with increase in the OH coverage percentage on the nanowire surfaces.

A smaller effective electron mass implies larger charge carrier mobility, thus, either increase or decrease of the charge carrier mobility in GeNWs will be observed with OH passivation depending on the growth directions of the GeNWs. Since the electrical conductivity is inversely proportional to effective mass of electrons, the decrease in effective electron mass will increase the electrical conductivity in the ⟨100⟩ GeNWs, while it will decrease in the ⟨110⟩ OH-GeNWs.

A previous experiment (*38*) shows that when the GeNWs are exposed to ambient air, the hysteresis in electric current of GeNWs is observed, but after annealing of GeNWs which removes the adsorbed water molecule and the oxide layer from the nanowire surface, no hysteresis is observed. Based on our results of OH-GeNWs, we can correlate the fact that when the GeNWs are exposed to ambient air they form GeO_2 which is dissolved in water and forms the OH group which is attached with surface Ge atom. The formation of a Ge-OH bond on the surface of the nanowire increases or decreases the electrical conductivity of GeNWs depending on growth directions. As such, we propose that the cause of hysteresis can be explained in such a way that during the experimental *I-V* measurement (*38*), the coverage OH percentage on the GeNW surface highly depends on the experimental conditions such as temperature and applied voltage. When the numbers of OH groups change, e.g. be removed from the surface of GeNWs due to high temperature, the effective electron mass of the nanowire will be altered i.e., the electrical conductivity. Consequently, the electrical

behaviours such as the *I-V* characteristics will be changed, resulting in a possible hysteresis phenomenon.

We attribute the OH group alignments on the surface of GeNW as another possible cause for the electrical hysteresis because it takes into account the influence of an applied electric field during the experimental measurement. We construct two neighbouring OH groups on the GeNW and see how their alignments would affect the band gap and the effective electron mass (Figure 5.7). We rotate one OH group by rotating $\angle Ge_1Ge_2OH$ dihedral angle (shown in Figure 5.7) from 0° to 360° in steps of 60° while keeping the other one fixed. The calculated band gap and effective electron mass for different configurations are listed in Table 5.4.

Table 5.4 The calculated band gap and effective mass of the mono-substituted ⟨100⟩ OH-GeNW (4.17% surface OH coverage) with different orientations of the OH group (*223*). [Reproduced by permission of the PCCP Owner Societies]

θ ($\angle Ge_1Ge_2OH$)[a]	**E_{gap} (eV)**	**m^*_e (m_e)**
75.7	2.02 *i*	3.59
135.7	2.02 *i*	3.36
195.7	2.01 *i*	3.33
255.7	2.01 *i*	3.91
315.7	2.01 *i*	3.83
15.7	2.01 *i*	3.66

[a] See Figure 5.7 for definition.

It is shown that the band gap does not change significantly (~0.01 eV). However, the effective electron mass of the mono-substituted OH-GeNW varies from 4.59 to 3.59 m_e (See

Figure 5.6 and Table 5.4) by changing the alignment of OH groups. The effective mass of electron in different configurations either increases or decreases depending on the rotated OH groups (Table 5.4). This hints that in the orientation of the OH group is changed during the experimental *I-V* curve study by applying the external electric field can change the effective mass of electron and thus the electrical conductivity of OH-GeNWs, resulting in possible the hysteresis phenomenon.

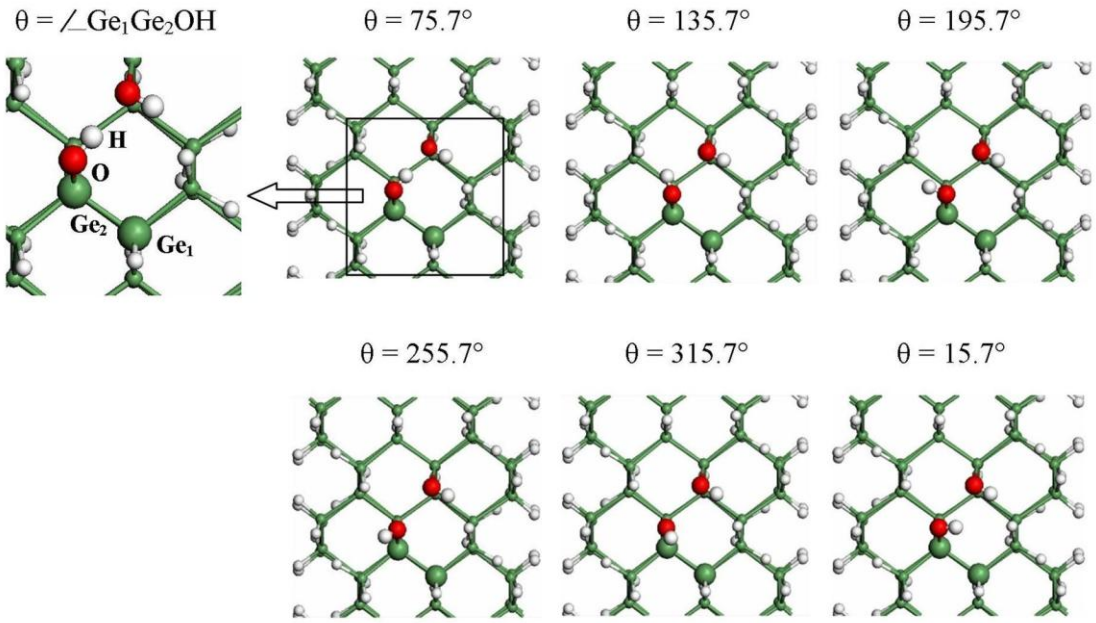

Figure 5.7 Structures of mono-substituted ⟨100⟩ OH-GeNW (4.17% surface coverage) with different orientations of the OH group (θ = 0 to 360°). θ is the dihedral angle (*223*). [Reproduced by permission of the PCCP Owner Societies]

In addition, the interface states in GeNWs due to Ge surface oxides can act as charge traps and also lead to the observed electrical hysteresis in GeNWs (*38*), (*237*). Here, we model the charge traps in OH-GeNWs by removing the OH group from the fully optimized 100% ⟨100⟩ OH-GeNW (see Figure 5.8) to create the surface defects. Then we investigate the effect of surface defects (which act as charge traps) on electronic properties of the 100%

⟨100⟩ OH-GeNW. The calculated band gap and effective mass of electron of the 100% ⟨100⟩ OH-GeNW with surface trap state defects are listed in Table 5.5. We find that the presence of charge traps in OH-GeNWs decrease the band gap of OH-GeNWs and vary the effective mass of electron. The results suggest that the surface trap state is another possible reason that can cause the observed electrical hysteresis in GeNWs.

Table 5.5 The calculated band gap and effective mass of electron of the ⟨100⟩ OH-GeNW (100% surface coverage) with surface trap state defects (*223*). [Reproduced by permission of the PCCP Owner Societies]

% Defects	E_{gap} **(eV)**[a]		m^*_e **(**m_e**)**	
	Spin-up	Spin-down	Spin-up	Spin-down
4.17	0.84 *d*	0.74 *d*	0.90	1.78
8.34	0.99 *d*	0.65 *d*	2.44	14.00

[a] *d* indicates direct band gap.

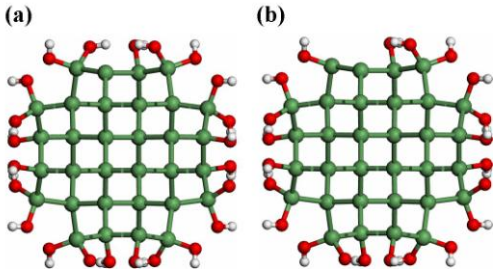

Figure 5.8 The structures of the 100% ⟨100⟩ OH-GeNW with (a) 4.17% and (b) 8.34% surface trap state defects (*223*). [Reproduced by permission of the PCCP Owner Societies]

In summary, we reveal that a water molecule is initially physisorbed on the GeNW surface which is a reversible adsorption and over time, the water molecule would dissociate into OH· and H· radicals leading to irreversible adsorption and formation of OH-GeNWs. In

addition, we also show that the amount of water adsorbed is a key factor that affects the stability and electronic properties of GeNWs. In summary, from our theoretical calculations, we attribute the causes of electrical hysteresis observed in GeNWs to (a) the different amount of water being adsorbed, (b) the alignment of the OH groups on the surface of the GeNWs; and (c) the presence of trap state defects on the surface of OH-GeNWs.

5.2 Stress Induced Half-Metallicity in Surface Defected Germanium Nanowire

In actual device applications, the nanostructures employed are usually not of perfect crystalline structures. The introduction of defects into these nanostructures can actually enhance the device performance. For example, defects can be introduced by dopant atoms such as boron (B) or phosphorus (P). The *n*- or *p*-doped nanostructures usually have more effective electrical response because of the enhanced electron or hole carriers raised by the dopant atoms. Another possible type of defect is surface dangling bond (SDB) which could be formed intrinsically during its formation. Since SDB defects occur naturally, investigating the effects of SDB on the electronic properties in nanostructures is thus important.

In particular, SDBs are responsible for nanostructures' magnetic properties (e.g. magnetic dipole moment, ferromagnetism, and half-metallicity are strongly associated with unpaired electron). In particular, for GeNWs, tuning of magnetic and electronic properties by transition metals doping have been reported to be possible (*238-239*). Therefore, it is important to understand the effects of defects to design nano-material for targeted applications such as spintronics or spin filters.

To the best of our knowledge, there are only a handful of theoretical reports for SDB defects related magnetic and spin properties on nanowire structures (*240-241*). In particular, Xu et al. (*240*) reported the electronic properties of ultrathin ⟨100⟩ silicon nanowires (SiNWs) with multiple SDBs by density-functional-theory (DFT) calculations. The presence of surface

defects generates bands that intersect with the Fermi level and split the bands into spin-up and spin-down orientations when spin polarization is taken into an account. The doped SiNW with B becomes half-metallic, which is robust against the applied external electric field. Park et al. (*241*) investigated the origin of ballistic hole gas observed in Ge/Si core-shell nanowire using spin-polarized DFT calculations. The Si surface dangling bonds and substitutional Au (Au_{Si}) defects behave as charge traps in Ge/Si NWs which generate hole carriers in the Ge core. Though the defect level in the case of Si SDBs and Au_{Si} defects is much deeper, the defect level for spin-down configuration becomes sufficiently shallow (even at room temperature) in large-diameter Ge/Si core-shell nanowires with large Ge core, which leads to *p*-type conductions. So far, the magnetic properties and half-metallicity of the studied nanowires are associated with the dopant impurity. The possibility of associating surface defect without dopant atoms with the half-metallic properties of nanowire remains unclear.

In this sub-section, we systematically investigate the effect of SDB defects on the magnetic and electronic properties of hydrogen passivated GeNWs using DFT calculations. First, we determine the SDB defect locations on the surface of GeNW. We show that the defects induced magnetic and electronic properties highly depend on the location of the defects. Secondly, we examine the effect of applying axial strain on these surface defected GeNWs and from which, we predict the possibility of half-metallic properties for GeNWs. Our results predict that half-metallic GeNWs can be obtained through manipulating of surface defect and nanowire structure without dopants.

5.2.1 Single & Multiples SDB Defects

To investigate the effect of surface defects on the electronic and magnetic properties of the GeNW, we create SDB defects by removing surface H atoms. By symmetry, the

GeNW surface has three different types of H atoms (labeled with H1, H2 and H3, see Figure 5.9).

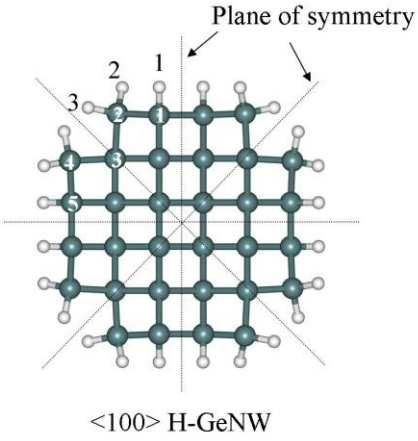

Figure 5.9 Cross-sectional views of optimized ⟨100⟩ H-GeNW. Three symmetric planes are shown. Green and white spheres represent Ge and H atoms, respectively.

The H1 atom is bonded to the Ge atom at the middle part of the surface, denoted as surface H atom. Both the H2 and H3 atoms are bonded to the corner Ge atom, denoted as corner H atoms. Though H2 and H3 atoms are bonded to the same Ge atom, H2 and H3 are in different chemical environment and hence non-identical. The three GeNWs to be considered with SDB defect are shown in Figure 5.10.

For multiple SDB defects, we select the double SDB defected GeNWs based on the symmetry. To generate double SDB defected GeNWs, we remove only the same type of H atoms (see Figure 5.9) e.g., we remove two nearest H1 atoms to get surface defected GeNW **2a** (see Figure 5.10). The only one exception is surface defected GeNW **2b**. We include **2b** to investigate the effect of double SDBs attaching to the same Ge atom. We also investigate the effect of quadruple and octuple SDB defects in order to understand the effect of defect concentration on the electronic and magnetic properties of GeNWs. Selected single, double and multiple SDB defected GeNWs in the following discussion are shown in Figure 5.10 and the rest can be found in the Appendix B.

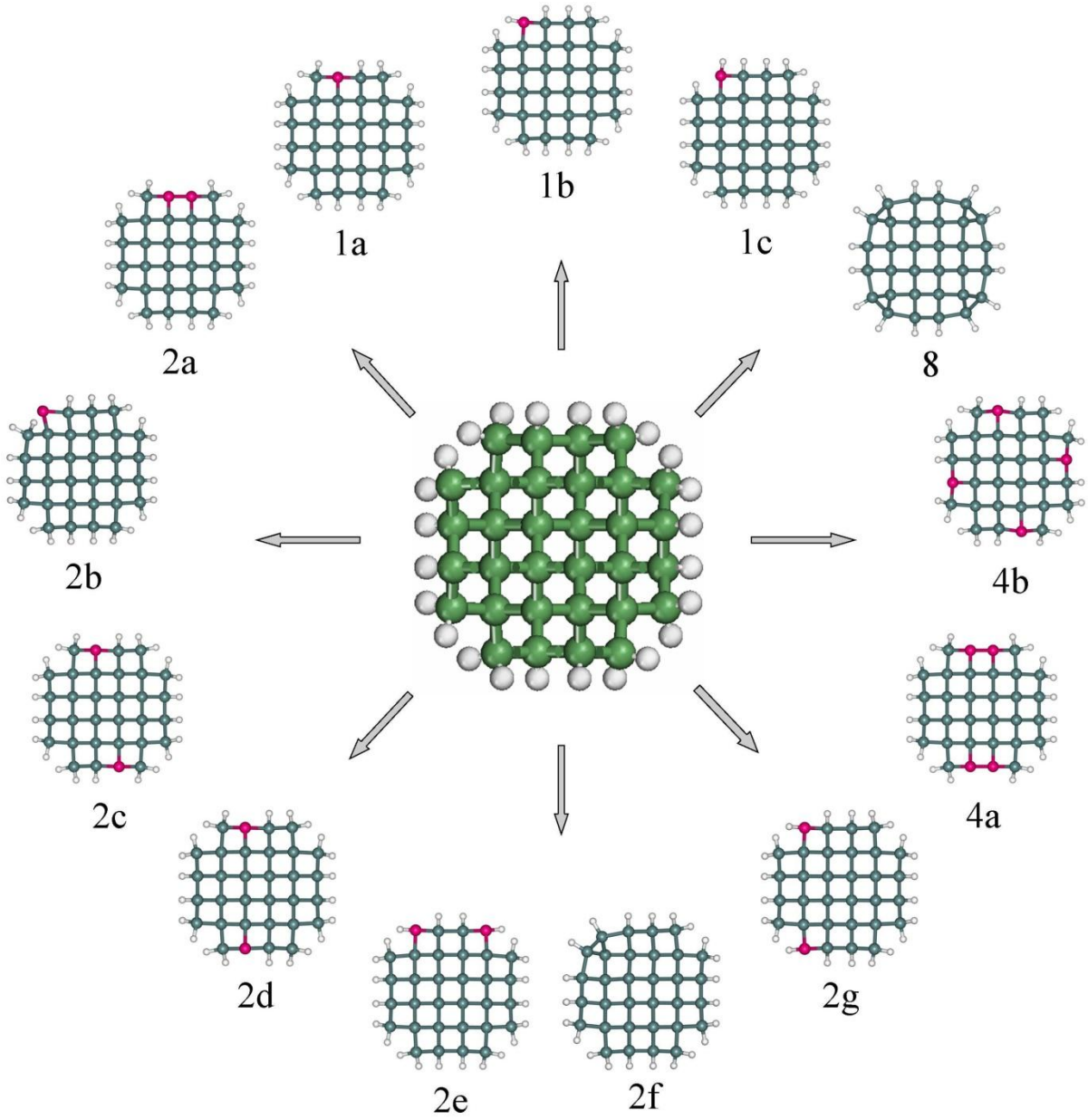

Figure 5.10 Selected optimized ⟨100⟩ surface defected GeNWs. Pink spheres represent Ge atoms with SDBs. The numbers 1, 2, 4 and 8 represent the single, double, quadruple and octuple SDB defects, respectively.

5.2.2 Defect Generation Energies

Before the investigation of the effect of surface defects on the magnetic and electronic properties of GeNW, we calculate the energy cost to generate SDB defects, defect generation energy, using the following equation, (*242*) –

$$E_{Gen}^{SDB} = E_{GeNW+SDB} + n\mu_H - E_{GeNW}, \quad (5.3)$$

where E_{Gen}^{SDB} is the defect generation energy of SDBs, $E_{GeNW+SDB}$ is the total energy of surface defected GeNW, E_{GeNW} is the total energy of H-GeNW, n is the number of H atom(s) removed, μ_H is the chemical potential of H, derived from H_2 molecular state. The calculated defect generation energies of SDB defects per SDB are listed in Table 5.6. All the calculated defect generation energies are endothermic except for **2f** (refer to Figure 5.10 for the nanowire labeling) which indicates that the generation of SDB is essentially thermo-neutral. To investigate the stability of surface defected GeNWs, we calculate the formation energies of surface defected GeNWs in a way that similar to our previous work (*223*). The calculated formation energies of surface defected GeNWs are listed in Table 5.6.

For single SDB defect, **1a** is the most stable structure compared to **1b** and **1c**, which indicates that the energy cost to remove H1 is the least for SDB defected GeNW. For double SDB defected GeNWs, **2f** is the most stable structure as it undergoes surface reconstruction via Ge2−Ge4 bond formation and results in GeNW with no unpaired electron. Thus, the energy cost to remove corner H atoms is compensated by the formation energy of additional Ge-Ge bond. Similarly, when H2 and H3 atoms are removed, significant electronic and surface rearrangement occurred (**2b**, see Figure 5.10) making it the most stable double SDB defected GeNWs after **2f** (see Table 5.6).

The calculated formation energy of SDB defected GeNWs shows that the surface defected GeNWs which undergo significant surface reconstruction, e.g., **2f** and **2b**, are the most stable structures with double SDB defects. On the other hand, for quadruple SDB defected GeNWs, **4a** and **4b** have the same formation energy.

Table 5.6 Calculated defect generation energies of SDB defects[a] per SDB (E_{Gen}^{SDB}), and formation energies (E_{form}), net magnetic moments (in μ_B) per unit cell and band gap (E_{gap}) of surface defected GeNWs.

GeNW	E_{Gen}^{SDB} per SDB (eV)	E_{form} (eV/Ge atoms)	Net magnetic moment (μ_B)	States[b]	E_{gap} (eV)	
					Spin-up	Spin-down
1a	0.72	0.21	0.99	FM	1.49	0.88
1b	0.92	0.22	1.00	FM	1.62	0.97
1c	0.91	0.22	1.00	FM	1.70	0.97
2a	0.72	0.23	1.83	wFM	1.31	0.90
2b	0.28	0.20	0.00	AFM	1.44	1.44
2c	0.72	0.23	1.50	wFM	0.00	0.00
2d	0.69	0.23	0.00	AFM	0.08	0.08
2e	0.92	0.24	2.00	FM	1.58	0.86
2f	-0.04	0.18	0.00	NM	2.00	
2g	0.92	0.24	0.49	wFM	0.00	0.00
4a	0.70	0.27	2.48	wFM	0.00	0.00
4b	0.70	0.27	0.88	wFM	0.00	0.00
8	0.02	0.19	0.00	NM	1.76	

[a] Defect generation energies of SDB defects indicate the energy cost to create SDBs by removing surface H atom(s). [b] FM, AFM, wFM and NM indicate ferromagnetic, anti-ferromagnetic, weak ferromagnetic and non-magnetic, respectively.

In addition, GeNW **8** is the most stable octuple SDB defected GeNWs we have studied (see Table 5.6 and Appendix B). This is because **8** undergoes surface reconstruction and all corner Ge atoms form Ge−Ge bonds similar to **2f** (see Figure 5.10), indicating that

removing all corner H3 atoms results in the most stable structure for octuple SDB defected GeNWs. Although there are differences in the formation energy of various surface defected GeNWs, we note that the differences are small and thus it is still possible to obtain the meta-stable GeNWs structures.

5.2.3 SDBs Induced Magnetic Dipole Moments

The calculated net magnetic moments of surface defected GeNWs per unit cell are listed in Table 5.6. Single SDB defected GeNWs have one unpaired electron per unit cell and the calculated net magnetic moment is 1.00 μ_B per unit cell. Based on the calculated net magnetic moments, double, quadruple and octuple SDB defected GeNWs can be divided into three groups: (1) GeNWs with zero magnetic moments (**2b**, **2d**, **2f** and **8**); (2) GeNWs with net magnetic moments equal to the number of SDBs (**2e)**, and (3) GeNWs with net magnetic moments significantly lower than the number of SDBs (**2a**, **2c**, **2g**, **4a**, **4b**).

For group (1), when two unpaired electrons occurs on the same Ge atom (e.g. **2b**), both of the electrons are in the singlet state resulting in zero magnetic moment and thus anti-ferromagnetic (AFM), please see Figure 5.11. When the two unpaired electrons are on adjacent corner Ge atoms (e.g. **2f** and **8**), GeNWs undergone surface reconstructions leading to Ge−Ge bond formation leading to no unpaired electrons and hence they are non-magnetic (NM) and hence have zero magnetic moment.

In contrast, for group (2), surface defected GeNWs with net magnetic moments equal to the number of SDBs are ferromagnetic (FM) (see Figure 5.10). However, the surface defected GeNWs can be either FM or AFM depending on the positions and the number of SDB defects. Finally, to understand the phenomena of group (3), surface defected GeNWs with net magnetic moments lesser than the number of SDBs (**2a**, **2c**, **2g**, **4a**, **4b**), we calculate the band structures of the GeNWs for discussion below.

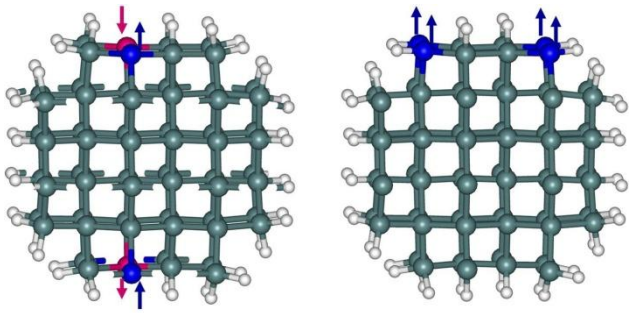

Figure 5.11 Spin configurations in surface defected GeNWs. The blue and pink color spheres label the spin-up and spin-down orientations, respectively.

5.2.4 SDBs Dependent Spin Configurations

The spin-up and spin-down electronic band structures of surface defected GeNWs are presented in Figure 5.12. The presence of SDB defects generates new bands in the band structures of the surface defected GeNWs, which is termed as defect levels. The spin-up ($\varepsilon_{DB,\uparrow}$) and spin-down ($\varepsilon_{DB,\downarrow}$) defect levels are represented by dotted line in Figure 5.12. The spin-polarized band structures of the surface defected GeNWs show that the defect levels split into spin-up ($\varepsilon_{DB,\uparrow}$) and spin-down ($\varepsilon_{DB,\downarrow}$) states (see Figure 5.12). All the single SDB defected GeNWs are semiconducting with different spin-up and spin-down band gaps (see Table 5.6). The spin-up ($\varepsilon_{DB,\uparrow}$) defect levels in **1a**, **1b** and **1c** lie 0.30, 0.25 and 0.27 eV above the valence band maximum (VBM), respectively. While the spin-down ($\varepsilon_{DB,\downarrow}$) defect levels in **1a**, **1b** and **1c** lie 0.88, 0.97 and 0.97 eV above the VBM, respectively. The exchange splitting, defined as the energy gap between the spin-up ($\varepsilon_{DB,\uparrow}$) maximum and spin-down ($\varepsilon_{DB,\downarrow}$) minimum, in **1a**, **1b** and **1c** are calculated to be 0.31, 0.54 and 0.62 eV, respectively. The large exchange splitting indicates that the single SDB defected GeNWs have distinctly different spin-up and spin-down band structures. It is evident here that the

electronic structures of single SDB defected GeNWs depend strongly on the locations (H1, H2 and H3) of the surface defects.

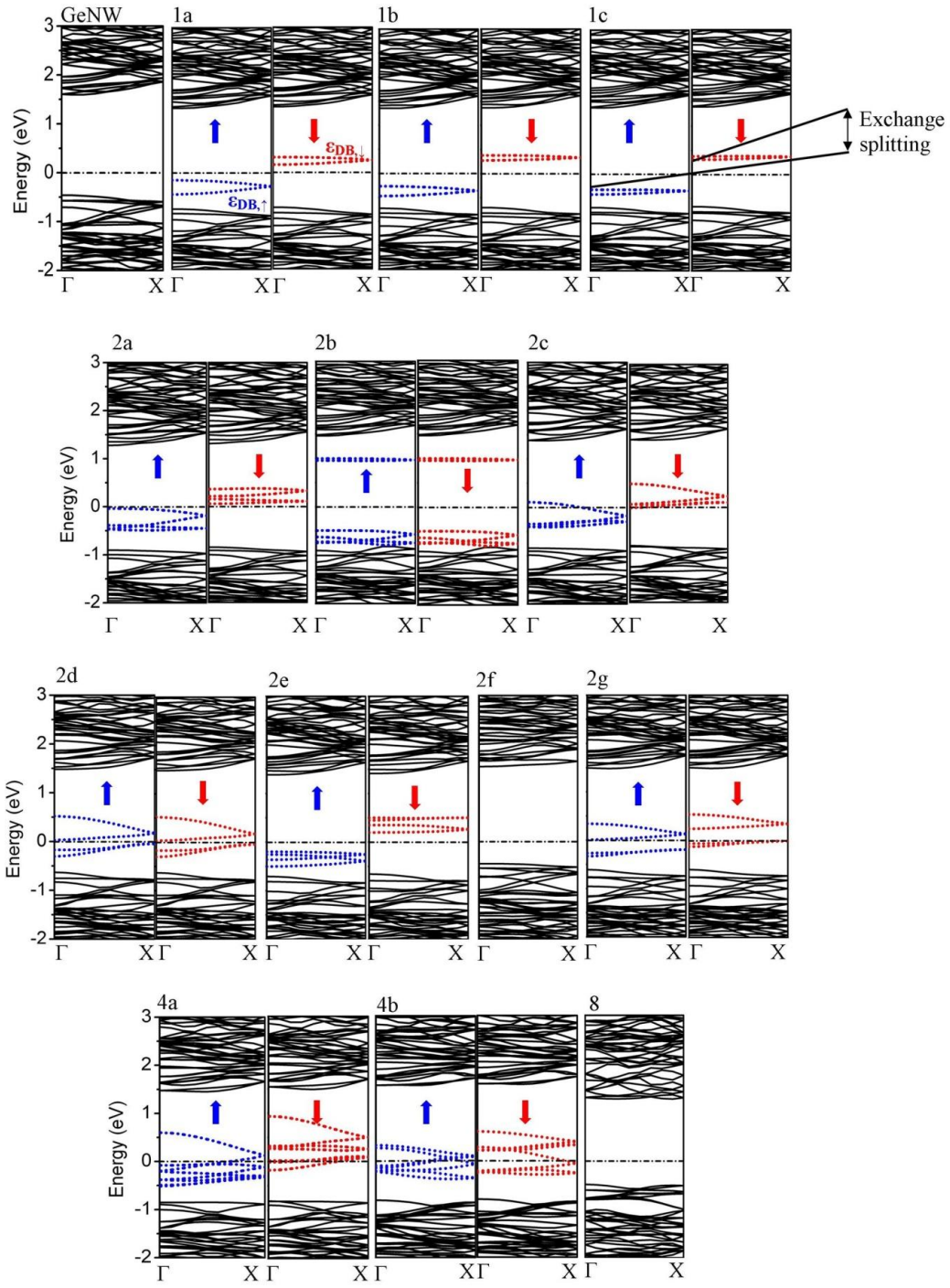

Figure 5.12 The spin-up and spin-down band structures of the surface defected GeNWs with single, double, quadruple and octuple SDB defects. The perfect GeNW is also shown at the top left corner for reference. Blue and red arrows indicate the spin-up and spin-down configurations. The dot-dashed line denotes the Fermi level.

The double or multiple SDB defected GeNWs show various band structure characteristics. For instance, the non-magnetic GeNWs **2f** and **8** have band structures similar to the perfect ⟨100⟩ H-GeNW (2.05 eV (*223*)) with band gaps of 2.00 eV and 1.79 eV, respectively (see Figure 5.12). Depending on the positions and number of SDB defects, surface defected GeNWs are either semiconductors or metals (see Table 5.6). Our results show that metallic and semiconducting GeNWs with spin-up and spin-down band structures coincide, are anti-ferromagnetic (i.e. spin alignments are in opposite directions) with zero magnetic moments. It is because the band structures of these GeNWs display equal spin-up and spin-down configurations. The majority of the studied surface defected GeNWs with anti-ferromagnetic configurations are semiconducting with the same spin-up and spin-down band gaps.

In contrast, surface defected GeNWs with different spin-up and spin-down band structures are ferromagnetic. All the ferromagnetic GeNWs with net magnetic moment equal to the number of SDBs are semiconducting with distinct spin-up and spin-down band gaps (see Table 5.6), while ferromagnetic GeNWs with no exchange splitting are metallic. For example, the exchange splitting in **2c** is zero and it has a net magnetic moment of 1.50 μ_B. While for **2a**, its exchange splitting and magnetic moment are 0.10 eV and 1.83 μ_B, respectively. The surface defected GeNW **2e** which exhibits a large exchange splitting has net magnetic moments of 2.00 μ_B. The large exchange splitting of **2e** suggests that the spin-up and spin down configurations are significantly different from each other and well separated. Thus, surface defected GeNWs with large exchange splitting have large magnetic moments and they are semiconducting in nature. The band structures of **2c**, **2g**, **4a**, **4b** show that the spin-down ($\varepsilon_{DB,\downarrow}$) defect levels are partially filled. This indicates that the electrons are shifted from spin-up to spin-down configuration. As a result, there is a reduction of the net magnetic moments of **2c**, **2g**, **4a**, **4b** and thus, they become metallic.

We also calculate the percentage of spin-polarization (*P*) of density-of-state (DOS) for **2a**, **2c**, **2g**, **4a** and **4b** (see Figure 5.13) to understand their reduced net magnetic moments. *P* is calculated according to the equation, (*240*) –

$$P = [G_{\uparrow}(E_F) - G_{\downarrow}(E_F)]/[G_{\uparrow}(E_F) + G_{\downarrow}(E_F)] \times 100\,, \qquad (5.4)$$

where $G_{\uparrow}(E_F)$ and $G_{\downarrow}(E_F)$ are the density-of-state of the majority and minority spins at the Fermi level (E_F), respectively. The calculated spin-polarization of GeNWs **2c**, **2g**, **4a**, **4b** are shown in Figure 5.13. The spin-up and spin-down bands of **2a** are semiconducting in nature. The $G_{\uparrow}(E_F)$ and $G_{\downarrow}(E_F)$ at the Fermi level of **2a** are non-zero. But the spin-up and spin-down bands are much closer to each other as suggested by a small exchange splitting of 0.01 eV leading to possible spin-contamination. Thus, the slight decrease of net magnetic moments of **2a** (1.83 μ_B) is likely caused by spin-contamination. However, **2c**, **2g**, **4a**, **4b** have spin-polarization of 12.10, 3.66, 92.86 and -65.79% which suggests that the spin-up and spin-down densities are different from each other. The positive spin-polarization indicates that the spin-up density is greater than spin-down density and vice versa. The calculated spin-polarization indicates that the spins are not confined but mixed. As a result, it significantly reduces the net magnetic moments in **2c**, **2g**, **4a**, **4b**.

2c can be considered as quasi half-metallic as there is no exchange splitting, indicating that both the spin-up and spin-down bands are metallic (i.e. the SDB defect levels intersect with the Fermi level). The spin-down ($\varepsilon_{DB,\downarrow}$) defect level in **2c** is only 0.01 eV below the Fermi level which suggests that the shift of spin-down ($\varepsilon_{DB,\downarrow}$) defect level above the Fermi level can lead to a complete half-metallic GeNW. As strain can alter electronic structures, we apply axial strain up to ±5% on **2c** to investigate its potential application as half-metallic material.

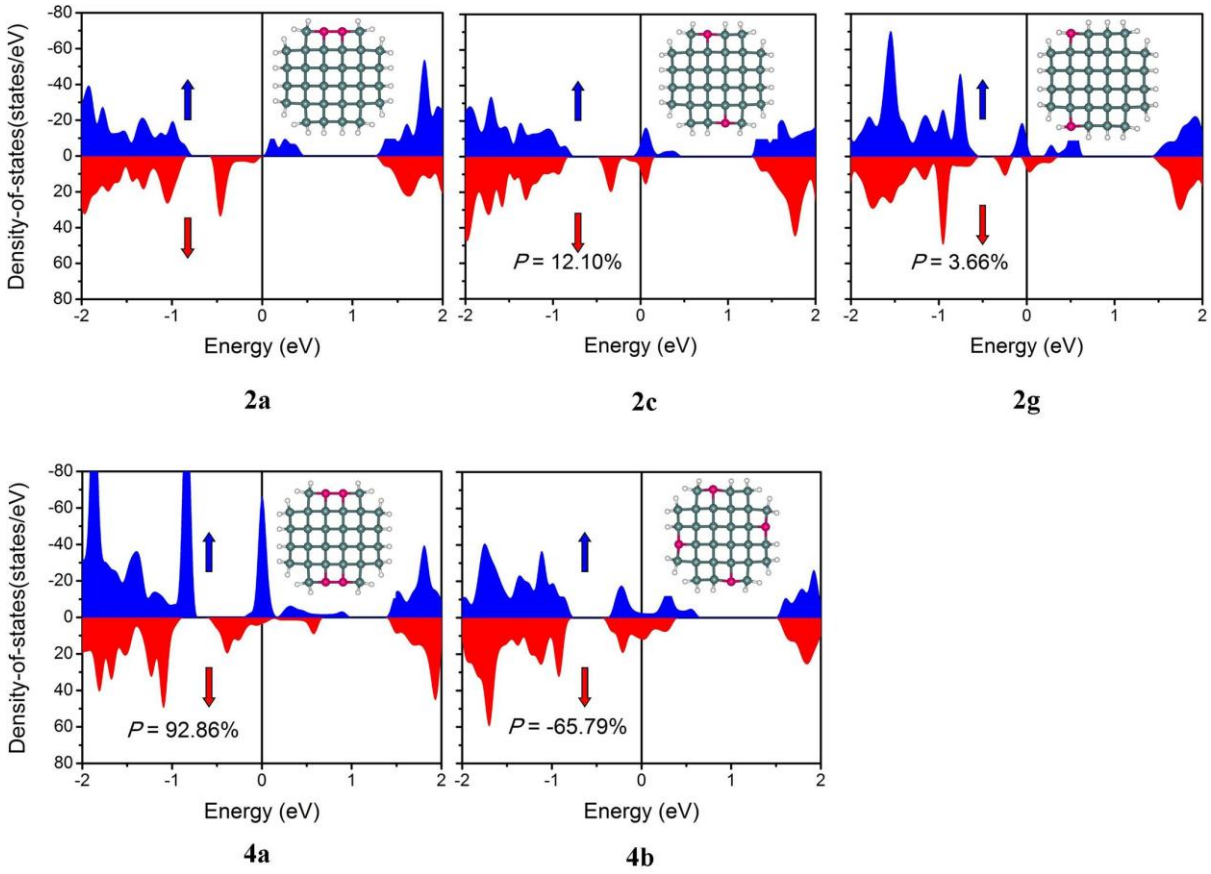

Figure 5.13 Density-of-states (DOS) of surface defected GeNWs **2a**, **2c**, **2g**, **4a** and **4d**. Blue and red areas represent spin-up and spin down densities, respectively. The spin-polarization (*P*) is shown.

5.2.5 Strain Effects Induced Half-Metallic GeNWs

The spin-up ($\varepsilon_{DB,\uparrow}$) defect level in **2c** is 107.5 meV above the Fermi level which indicates that the ($\varepsilon_{DB,\uparrow}$) defect level intersects with the Fermi level and the spin-up state is metallic. Whereas, the spin-down ($\varepsilon_{DB,\downarrow}$) defect level is just only -12.3 meV (negative value means that the spin-down ($\varepsilon_{DB,\downarrow}$) defect level is below the Fermi level), which indicates that the spin-down ($\varepsilon_{DB,\downarrow}$) defect level cuts across the Fermi level and the spin-down defect level is also metallic. We apply the axial strain to manipulate the band structures of **2c**. The applied axial strain is calculated according to the ratio expression: $(L-L_0)/L_0$, where L is the length

of strained GeNW along the *z*-axis and L_0 is the equilibrium lattice constant of the GeNW. The equilibrium lattice constant of the GeNWs are obtained by fully relaxing the geometry of GeNWs. By convention, the compressive strain is negative and tensile strain is positive. We apply both the compressive and tensile strains on **2c** along the *z*-direction with an increment of ±2.5%.

The strain-induced band structures of **2c** with different applied strains are shown in Figure 5.14.

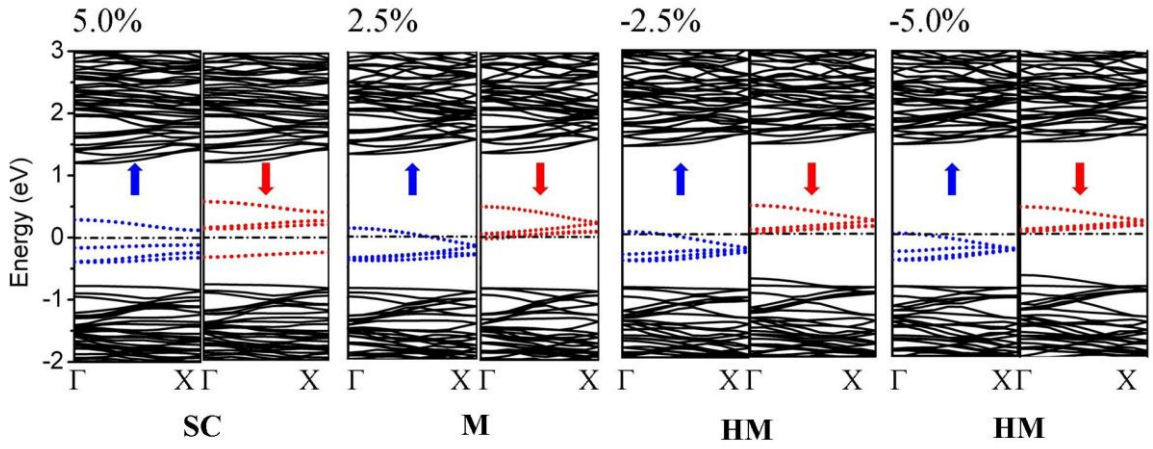

Figure 5.14 The strain-induced band structures of surface defected GeNW **2c**. **SC**, **M** and **HM** stand for semiconducting, metallic and half-metallic, respectively.

The application of 2.5% compressive strain changes the spin-down ($\varepsilon_{DB,\downarrow}$) defect level to 16.7 meV with respect to the Fermi level (see Table 5.7), which indicates that the spin-down ($\varepsilon_{DB,\downarrow}$) defect level does not intersect with the Fermi level and becomes semiconducting. Whereas the 2.5% compressive strain reduces the spin-up ($\varepsilon_{DB,\uparrow}$) defect level with respect to the Fermi level but retains the metallic properties. Further increase of compressive strain to 5.0% has little effect on the spin-up ($\varepsilon_{DB,\uparrow}$) and spin-down ($\varepsilon_{DB,\downarrow}$) levels. As a result, compressive strain retains the metallic nature of the spin-up state, while

changes the nature of the spin-down state to semiconducting. Consequently, surface defected GeNW **2c** becomes half-metallic.

Table 5.7 Calculated spin-up ($\varepsilon_{DB,\uparrow}$) and spin-down ($\varepsilon_{DB,\downarrow}$) defect levels with respect to the Fermi level (FL) in GeNW **2c** with and without applied strain.

Strain (%)[a]	$\varepsilon_{DB,\uparrow}$ [b] **(meV) with respect to FL**	$\varepsilon_{DB,\downarrow}$ [c] **(meV) with respect to FL**	**Net magnetic moment (μ_B)**	**Nature**[d]
5.0	-162.7	136.9	0.98	SC
2.5	136.0	-22.7	1.22	M
0.0	107.5	-12.3	1.50	M
-2.5	49.4	16.7	1.68	HM
-5.0	42.2	16.0	1.78	HM

[a] Positive and negative values indicate the tensile and compressive strain, respectively. [b] Positive $\varepsilon_{DB,\uparrow}$ indicates that the defect level cuts cross the Fermi level (FL). [c] Negative $\varepsilon_{DB,\downarrow}$ indicates that the defect level cuts cross the FL. [d] SC, M and HM indicate semiconducting, metallic and half-metallic, respectively.

In contrast, the tensile strain has completely different effect on the band structure of **2c**. With 2.5% tensile strain, the spin-down ($\varepsilon_{DB,\downarrow}$) defect level with respect to the Fermi level becomes negative (-22.7 meV) which indicates that the spin-down ($\varepsilon_{DB,\downarrow}$) defect level intersects with the Fermi level and remains metallic. As a result, with 2.5% tensile strain, both the spin-up and spin-down states are metallic. Moreover, with applying 5.0% tensile strain, the spin-up ($\varepsilon_{DB,\uparrow}$) defect level changes to -162.7 meV while the spin-down ($\varepsilon_{DB,\downarrow}$) defect level to 139.9 meV, which denotes that both the spin-up and spin-down states are

semiconducting. In addition, our results also demonstrate that the mechanical strain can change the net magnetic moments of **2c** (see Table 5.7). The compressive strain increases the magnetic moment of **2c** whereas the tensile strain decreases it. From the strain analysis we find that the GeNW **2c** with a net magnetic moment greater than 1.50 μ_B has half-metallic nature. Thus, we investigate how the net magnetic moments affect the half-metallicity of **2c**.

We vary the net magnetic moments/unit cell from 0.00 to 2.00 μ_B with the steps of 0.25 μ_B. The net magnetic moments of **2c** are held fixed while we fully relax the structures. The relative energy of **2c** is plotted as a function of net magnetic moments/unit cell as shown in Figure 5.15. The optimized magnetic moments of **2c** is 1.50 μ_B (see Table 5.6), but when the net magnetic moments/unit cell of **2c** are fixed at 1.75 and 2.00 μ_B, our results show that **2c** with 1.75 and 2.00 μ_B are only 4.87 and 5.44 meV lower in energy as compared to **2c**, respectively.

The corresponding electronic band structures of **2c** with different net magnetic moments are calculated and their spin-up ($\varepsilon_{DB,\uparrow}$) and spin-down ($\varepsilon_{DB,\downarrow}$) defect levels with respect to the Fermi level are listed in Table 5.8. We show that the spin-up and spin-down band structures of **2c** with net magnetic moments from 0.00 to 1.50 μ_B are metallic. When the magnetic moment of **2c** is fixed at 1.75 μ_B, the spin-down band structure becomes semiconducting while the spin-up band structure remains as metallic and thus leads to a half-metallic GeNW. Here, we show that **2c** has a very clear half-metallicity when the net magnetic moment/unit cell is fixed at 2.00 μ_B. Similarly, when we fix the net magnetic moments of **2a**, **2g**, **4a** and **4b** equal to the number of SDBs, they also show the half-metallic properties (see Figure 5.16). This analysis support the possibility to half-metallicity in surface defected GeNWs by manipulation of applied strain. In summary, applied compressive strain increases the net magnetic moments of the surface defected GeNWs that have the net magnetic moments significantly less than the number of SDBs. It thus forces the electron to

reside on one spin and result in half-metallic GeNWs. In conclusion, our results show that proper manipulation of strains on surface defected GeNWs can create half-metallic GeNWs.

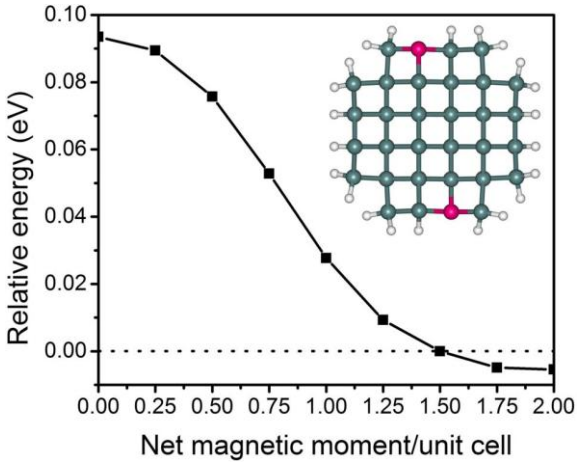

Figure 5.15 Relative energy as a function of net magnetic moment/unit cell for GeNW **2c**.

Table 5.8 Calculated spin-up ($\varepsilon_{DB,\uparrow}$) and spin-down ($\varepsilon_{DB,\downarrow}$) defect levels with respect to the Fermi level (FL) of GeNW **2c** with different fixed magnetic moments.

Fixed Net magnetic moment (μ_B)	**$\varepsilon_{DB,\uparrow}$ (meV) with respect to FL**	**$\varepsilon_{DB,\downarrow}$ (meV) with respect to FL**	**Nature**
0.00	418.5	-82.7	M
0.25	370.3	-58.1	M
0.50	322.1	-35.7	M
0.75	269.8	-12.8	M
1.00	215.2	-48.8	M
1.25	156.6	-32.2	M
1.50	107.5	-12.3	M
1.75	65.0	19.4	HM
2.00	393.8	436.5	HM

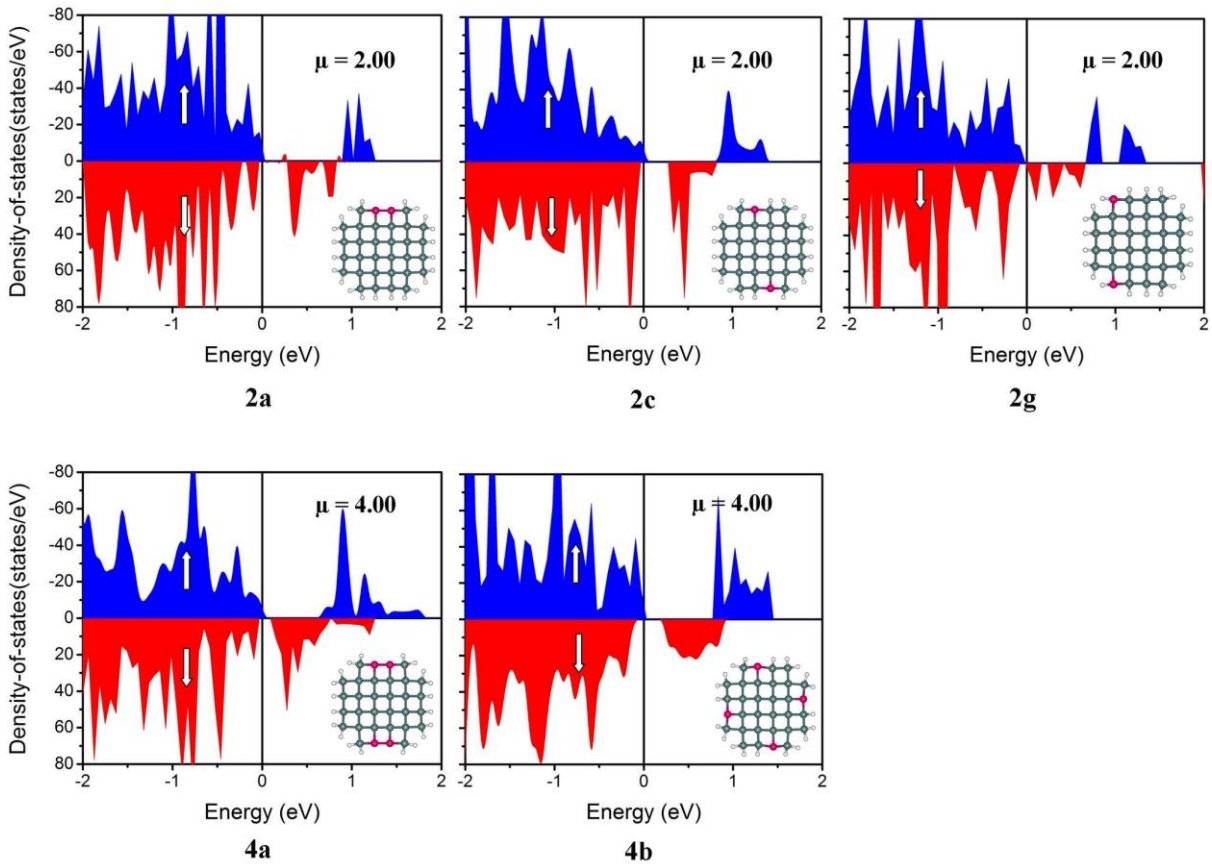

Figure 5.16 The density-of-states (DOS) of the surface defected GeNWs **2a**, **2c**, **2g**, **4a** and **4d** with fixed net magnetic moments that is equal to the number of SDBs.

In summary, we have used DFT calculations to investigate single, double, quadruple and octuple SDB defected GeNWs. We show that single SDB defected GeNWs remain semiconducting as its perfect form. Moreover, we find that defect location on the surface is a critical factor affecting the electronic and magnetic properties of the surface defected GeNWs. The double or multiple SDB defected GeNWs are either semiconducting or metallic, depending on the defect locations. We reveal that the surface defected GeNWs can be classified into three classes: (1) GeNWs with zero magnetic moment are either metallic or semiconducting; (2) GeNWs with net magnetic moments equal to the number of SDBs are semiconducting with distinct spin-up and spin-down configurations; (3) GeNWs with net magnetic moments significantly lower than the number of SDBs. We demonstrate that half-

metallic GeNWs can be obtained via applying mechanical strains. In conclusion, our current predictions suggest that half-metallic GeNWs can be obtained from engineering their surface defects and structures without the presence of impurity dopants.

Chapter 6

Interactions of Molecules/ Radicals with Single-Walled Carbon Nanotubes

In this chapter we investigate the interactions of molecules and radicals with various single-walled carbon nanotubes (SWNTs). The aim of this study is to obtain the fundamental understanding about the differential binding properties of molecules/ radicals on SWNTs and hence the mechanism of their separations. Because the separation of semiconducting SWNTs from metallic SWNTs are essential for the applications of semiconducting SWNTs in FETs

and also for other applications of NTs as mentioned in Chapter 3. The periodic model of SWNTs is used for our current study. The model of one chiral, armchair and zigzag SWNTs is shown in Figure 6.1.

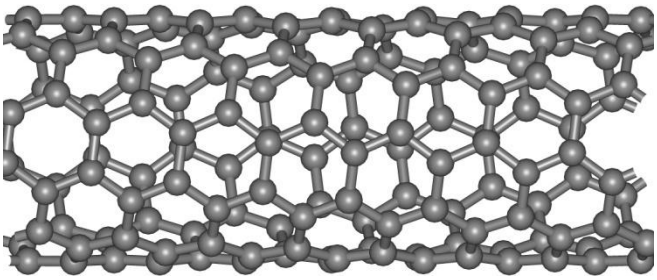

Chiral SWNT (6,4)

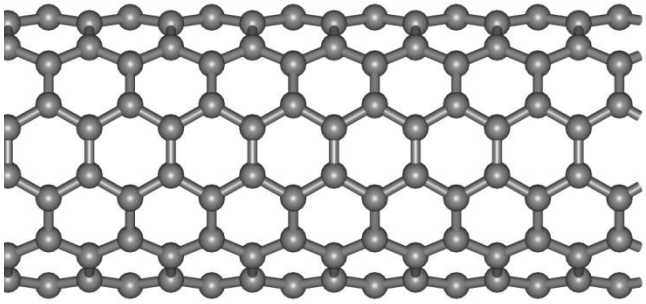

Armchair SWNT (6,6)

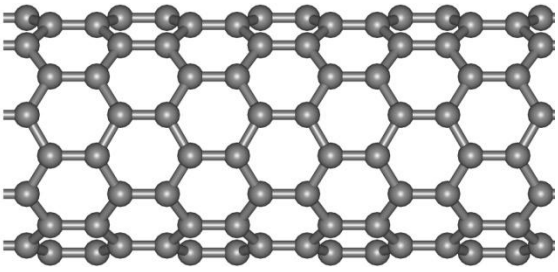

Zigzag SWNT (9,0)

Figure 6.1 The structure of chiral, armchair and zigzag SWNTs.

6.1 Anthraquinone Adsorption on SWNTs

We apply density functional calculations to model the interaction of 2-ethylanthraquinone (EAQ) (see Figure 6.2) with various semiconducting and metallic nanotube species present. The structures of all the SWNTs are optimized and then the

interactions of EAQ with SWNTs are studied. The binding energy of EAQ with the SWNT is calculated as follows –

$$E_{BE} = E_{species/SWNT} - (E_{species} + E_{SWNT}), \qquad (6.1)$$

where E_{BE} is the binding energy, $E_{species/SWNT}$ is the total energy of the surface species (i.e., molecules/radicals) and SWNT complex, $E_{species}$ is the total energy of surface species and E_{SWNT} is the total energy of SWNT. The negative value of E_{BE} indicates favorable interaction. The calculated binding energies of EAQ with SWNTs are listed in Table 6.1.

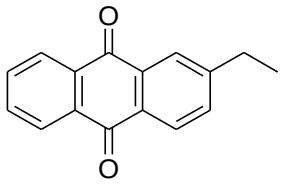

Figure 6.2 Structures of 2-ethylanthraquinone (EAQ).

Table 6.1 Binding energies (in eV) of adsorbants with various SWNT. [Reprinted with permission from ref. (*243*). Copyright 2010, American Chemical Society]

			Binding energy (eV)	
	Type[a]	**Diameter (Å)**	**EAQ**	**·OH**
SWNT (8,2)	m	7.27	~ 0.00	-1.77
SWNT (7,4)	m	7.63	~ 0.00	-1.52
SWNT (10,1)	m	8.34	~ 0.00	-1.54
SWNT (6,4)	sc	6.92	~ 0.00	-1.40
SWNT (6,5)	sc	7.56	~ 0.00	-1.24
SWNT (7,5)	sc	8.27	~ 0.00	-1.26
SWNT (8,4)	sc	8.37	~ 0.00	-1.27

[a] m – metallic, sc – semiconducting

We find that the EAQ molecule does not bind to the semiconducting or metallic SWNTs with essentially zero binding energy (see Table 6.1). The result is consistent with the report by Woods et al. (*244*) that benzene is only physisorbed on SWNT (8,0) with equilibrium distance of ~ 3.15 Å above the SWNT. We find that ·OH radical interacts with all the metallic and semiconducting species with binding energies between -1.77eV and -1.24eV, forming single bond between C and O with bond distance of ~ 1.47 Å (see Table 6.1 and Figure 6.3).

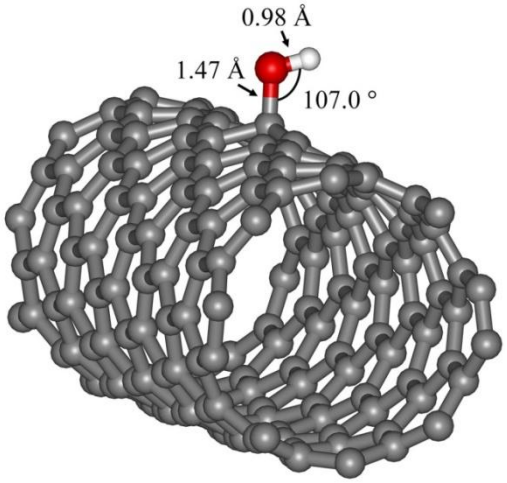

Figure 6.3 Optimized geometry of ·OH radical adsorption on metallic SWNT (8,2). Grey spheres – C; red sphere – O; white sphere – H. [Reprinted with permission from ref. (*243*). Copyright 2010, American Chemical Society]

We also find that the binding of ·OH radical with metallic nanotubes is stronger than with semiconducting tubes of similar diameter. For example, SWNT (7,4) binds more strongly by -0.28eV than SWNT (6,5) and these two tubes which have about the same diameter (~7.6Å) are metallic and semiconducting, respectively. Moreover, the smaller diameter tubes (both semiconducting and metallic) have stronger interaction with the ·OH radical than larger diameter nanotubes.

The treatment of EAQ with SWNTs and centrifugation of the sample yielded the supernatant SWNT which is rich with large diameter semiconducting SWNTs indicating that the EAQ prefers metallic and small diameters semiconducting SWNTs (*243*). Since, the EAQ under UV can forms radicals (*245*), based on our theoretical study of ·OH radical adsorption with SWNTs, we conclude that the radicals generated from EAQ is the active species responsible for the enrichment of semiconducting SWNTs.

6.2 Bromine Adsorption on SWNTs

We study the interaction of Br· radical with chiral SWNTs, *i.e.* (6,4), (7,4), (7,5), (8,2), (8,4), (8,6) and (9,3) and zigzag SWNTs (9,0) and (10,0) and armchair SWNTs (6,6) and (7,7). We consider the adsorption of Br· radical at top site (shown in Figure 6.4). The binding energy of Br radical with the SWNT is calculated according to eqn (6.1). The calculated binding energy of Br· radical with SWNTs is listed in Table 6.2. The optimized diameter of SWNTs and the distances between Br atom and nearest C atom are also listed in Table 6.2.

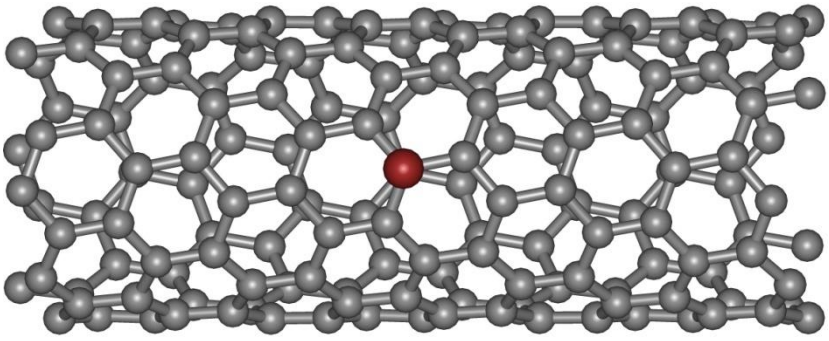

Figure 6.4 Top-model of the optimized Br and SWNT (8,4) complex. Grey spheres – C; brown sphere – Br.

Table 6.2 Binding energies (in eV) of Br· radical with various SWNTs.

				Binding energy (eV)
	Type	**Diameter (Å)**	***d* (C-Br in Å)**	**Br·**
SWNT (6,4)	sc (chiral)	6.92	2.73	-0.69
SWNT (7,5)	sc (chiral)	8.27	3.17	-0.67
SWNT (8,4)	sc (chiral)	8.37	3.16	-0.68
SWNT (8,6)	sc (chiral)	9.61	3.21	-0.71
SWNT (8,2)	m (chiral)	7.27	2.61	-0.99
SWNT (7,4)	m (chiral)	7.63	2.87	-0.86
SWNT (9,3)	m (chiral)	8.54	2.73	-0.96
SWNT (10,0)	sc (zigzag)	7.91	2.76	-0.70
SWNT (9,0)	m (zigzag)	7.15	2.45	-1.11
SWNT (6,6)	m (armchair)	8.14	2.82	-0.56
SWNT (7,7)	m (armchair)	9.57	3.26	-0.52

All the calculated binding energies are negative which shows that the interaction between Br· and SWNTs are favorable. The calculated C-Br distances vary from 2.45-3.21 Å which suggests that the interactions between Br· radical and all the SWNTs are in between chemisorption and physisorption, because the sum of the covalent and the van der Waals radii of C and Br are 1.91 and 3.55 Å, respectively. We have investigated the interactions of Br· radical with three different classes of SWNTs, i.e., chiral, zigzag and armchair SWNTs. Among the chiral SWNTs, metallic SWNTs have stronger interaction with Br· radical as compared to semiconducting SWNTs. In case of zigzag SWNTs, Br· radical has stronger interaction with metallic SWNT as compared to semiconducting. Thus, our results show that Br· radical has stronger interaction with metallic for both chiral and zigzag. The armchair

SWNTs are special class of SWNTs in terms of electronic properties as compared to chiral and zigzag SWNTs, because the entire armchair SWNTs are metallic in nature. Our interaction study shows that the binding energies of armchair SWNTs depend on the diameter of tubes. We find that the binding energy of Br· with armchair SWNT (6,6) and (7,7) is lower as compared to chiral and zigzag SWNTs under investigations.

The lower binding energy of Br· with SWNT (6,6) and (7,7) may be explained in the following way: though SWNT (6,6) and (7,7) are metallic SWNT, but belong to different class (armchair). The interactions of surface species with SWNTs not only depend on metallic or semiconducting SWNTs but also depend on different class of SWNTs, i.e., armchair, zigzag and chiral, which can be supported by the current theoretical work and the theoretical work of N. Park et al. (*186*) and B. B. Shirvani (*185*). N. Park et al. (*186*), study the interactions of Br with zigzag SWNTs (8,0), (9,0), (10,0), (17,0) and (18,0) using DFT with in a local density approximation (LDA) with energy cut-off of 50 Ry. The binding energy of Br with metallic SWNT (9,0) and (18,0) is -1.33 and -1.45 eV, respectively. The binding energy of Br with semiconducting SWNT (8,0), (10,0) and (17,0) is -1.16, -1.26 and -1.40 eV, respectively. Their results also show that Br prefers to bind to metallic SWNT compared to semiconducting and the binding affinity increases with increase SWNT's diameter. B. B. Shirvani et al. (*185*), studied the NH_3 adsorption on zigzag SWNT (5,0), (8,0) and armchair SWNT (5,5) and (6,6) at the level of B3LYP/6-31G*. Calculated binding energy of NH_3 with (5,0), (8,0), (5,5) and (6,6) is -112, -50, -11, -3 meV respectively. Their results show that NH_3 has more binding affinity towards zigzag SWNTs as compared to armchair CNTs. The binding affinity also decreases with the increase in diameter of SWNTs.

Chen et al. (*246*) described the enrichment of semiconducting SWNTs by treating the SWNT sample with bromine. The addition of dilute bromine solution to SWNTs sample forms the charge transfer complex between Br and SWNTs. The centrifugation of bromine

treated SWNT sample yielded the supernatant and sediment samples. The adsorption spectrum of supernatant sample showed that the sample is rich with semiconducting species. This indicated that the Br preferentially binds with metallic SWNTs and forms charge transfer complex and sediments from the SWNT sample as a result the supernatant become rich in semiconducting species. Our calculations also show that the Br prefers metallic SWNTs for both chiral and zigzag SWNTs and the interaction between Br and SWNTs are in between chemisorption and physisorption.

Chapter 7

Summary

To sustain the trend of scaling beyond current transistors, the most important materials being considered are semiconducting nanowires and carbon nanotubes. Semiconducting germanium nanowires (GeNWs) have attracted recent interest of researcher for unique properties of Ge at nanoscale level as compared to Si. They are proposed for various applications e.g., in spintronics for alternative of carbon nanotubes, as a candidate for UV dosimetry, alternative for the existing graphite anode in Li ion batteries, photoresistors,

photodetector in visible range, terapixel infrared photodetection systems, memory devices. However, the existing problems like surface oxidation and observed electric hysteresis in GeNW FETs, limits their use in electronic devices. Since, the large electric hysteresis in any devices is undesirable, because it makes the performance of devices unpredictable. Thus, the removal of electrical hysteresis in GeNWs is essential for better stability and performance of GeNWs devices. GeNW surfaces are highly susceptible to oxidation and corrosion when they are exposed to oxygen and water and forms Ge dioxide (GeO_2). As a result, the interface between Ge and its oxide has high surface states which will affect the performance of electronic devices. The formed GeO_2 strongly adsorbs water molecules and shows electrical hysteresis in GeNW FETs. The hysteresis is removed when the GeNW FETs is placed back to vacuum after short exposure. Long exposure of GeNW FETs to ambient air exhibits large electrical hysteresis which still exists after placing GeNW FETs back to vacuum. It was proposed that the observed electrical hysteresis may be due to presence of the high surface state and presence of adsorbed water molecule on the oxidized GeNWs surfaces. In this thesis using density functional theory (DFT) calculations, we investigated the electronic properties of water adsorbed GeNWs to investigate the cause of experimentally observed electrical hysteresis by calculating band gap, effective mass of electrons. In addition, we investigated the surface defects induced electronic and magnetic properties of GeNWs. We also investigated the interactions of different molecules/ radicals with single-walled carbon nanotubes (SWNTs) to obtain the fundamental understanding about the binding properties of molecules/ radicals and the mechanism of separation of SWNTs which are essential for their various applications.

Before study the GeNWs, the structures, stabilities, nature of bonding and hyperconjugations of germaallenes, building block of GeNWs, were investigated as the starting point to understand the bonding and electronic structures of GeNWs using DFT

B3LYP, MP2 and CCSD methods. Germaallenes are heavier group 14 analogues of allene which have attracted much attention of experimental and theoretical chemists due to their different bonding, structures and reactivities from allene. We used two monogermaallenes (1-germaallene and 2-germaallene), two digermaallenes (1,3-digermaallene and 1,2-digermaallene) and trigermaallene for our study. We found that germaallenes, except 1,3-digermaallene, have different electronic structure and bonding from classic allene. 2-germaallene and 1,2-digermaallene molecules each have one bent and one cyclic isomers. The bent and cyclic isomers of 2-germaallene have C_2 and C_{2v} symmetry, respectively. Both the isomers of 1,2-digermaallene have C_S symmetry. The cyclic structures of 2-germaallene and 1,2-digermaallene molecules are more stable as compared to their bent structure. In contrast, the cyclic isomer (C_{2v}) of trigermaallene is higher in potential energy than its strongly bent C_s structure. The natural population analysis showed that the *p*-character increases in the valence orbital of central Ge atom and the *s*-character also becomes more in orbitals composing of the π-bond. For trigermaallene, there is a partial overlapping from two *p*-orbitals on terminal Ge atoms and the central Ge atom does not adopt an orbital hybridization.

The NBO second-order perturbation analysis indicated that there is π-σ hyperconjugation interactions within germaallene and the strength of π-σ hyperconjugation followed the order: 1-germaallene (38.58 kcal/mol) > 1,3-digermaallene (28.60 kcal/mol) > 2-germaallene (17.00 kcal/mol) > 1,2-digermaallene (12.07 kcal/mol). However, the stabilities of the monogermaallene and digermaallene isomers followed the sequence as following: 1-germaallene (0.00 kcal/mol) > 2-germaallene (11.91 kcal/mol) and 1,2-digermaallene (0.00 kcal/mol) > 1,3-digermaallene (31.18 kcal/mol, at B3LYP/6-311+G(d,p) level. We compared the contributions of the -C=C-, -Ge=C- and -Ge=Ge- double bonds to stability using two reactions which represent the different parts after germaallene are broken

up into two units of hetero- and mononuclear analogue of ethane. The relative bond energies are close to the corresponding total relative stabilities (11.91 and 31.18 kcal/mol) in monogermaallene and digermaallene groups. Thus, we come to conclusion that the stability of germaallene is determined primarily by the stability of the bonds that compose them. The stability sequence of bond energies in digermaallene group (1,2-digermaallene > 1,3-digermaallene) is contrary to that of the hyperconjugation. As expected, it reflects that stabilization by hyperconjugation is not the main factor that determines the compound's total stability.

We have systemically applied DFT calculations to evaluate the possible cause of electrical hysteresis observed experimentally in GeNW based electronic devices. We first rationalized how the OH passivated GeNW (OH-GeNW) is formed, from which we proposed the formation mechanism of OH-GeNWs. Then, we evaluated in details its electronic properties such as band gap, effective mass and density-of-state (DOS). Furthermore, by examining OH-GeNWs with various OH coverage percentages and different alignment of the OH groups on the GeNW surface, we come up with the possible causes to the origin of electrical hysteresis phenomenon observed in experiment. We used ⟨100⟩ GeO_2 surface model to study the adsorption behaviour of water on oxidized GeNW surfaces using molecular adsorption and dissociative chemisorption of water molecules on GeO_2 surface. We observed that the adsorption of molecular water on GeO_2 surface is exothermic with adsorption energy of -0.60 eV. After dissociation of water into OH· and H· radicals, the OH· radical is adsorbed on a surface Ge atom and the dissociated H· radical migrated and is bonded to a surface O with more favourable exothermic energy of -1.79 eV compared to molecular adsorption. Once the water molecule is dissociated, the reversible desorption of water molecule is a highly endothermic process. Based on our results, we proposed that the water molecule is initially physisorbed on the surface of GeNW which is a reversible

adsorption and over time, water molecule would dissociate into OH· and H· radicals leading to irreversible adsorption and formation of OH-GeNWs.

To design the OH-GeNW with high surface coverage of OH groups, we have investigated the preferential adsorption sites of the OH on GeNWs surfaces by replacing the surface H atoms with the OH groups. Based on this study we designed the OH-GeNWs with different surface coverage of OH. Then we investigated the stability of OH-GeNWs by calculating the formation energy. The calculated formation energy of both the ⟨100⟩ and ⟨110⟩ GeNWs become more negative with increasing in the OH coverage percentage indicating that the formation of OH-GeNWs with higher surface coverage percentage is more favourable. The reason can be attributed to the stronger Ge-OH bond strength compared to Ge-H bond strength. Moreover, for the ⟨100⟩ and ⟨110⟩ GeNWs, the formation energies of both of them show a linear relationship with OH coverage percentage.

The calculated band gap of GeNWs showed that the higher the percentage of OH passivation, the smaller the band gap for the GeNW. Band gaps of ⟨100⟩ OH-GeNWs with various OH coverage percentages ranged from 2.02 to 1.05 eV while for the ⟨110⟩ OH-GeNWs, 1.13 to 0.52 eV. The band gap reduction may be explained by the increase of *s*- and *p*-occupancy of the highest occupied molecular orbital (HOMO) and the lowest unoccupied molecular orbital (LUMO) with the increase of surface OH coverage percentage. The calculated density-of-states showed that the reduction of band gap for the ⟨100⟩ GeNW with OH passivation is due to generation of the new electronic states near Fermi level, while the OH group has less effect on the electronic states near Fermi level in ⟨110⟩ GeNW. Since, the electrical conductivity of any materials is inversely proportional to effective mass of the electrons, we calculated the effective mass of electrons of OH-GeNWs from the band structures and investigated the effect of OH surface coverage, orientation of OH group and surface state (charge traps) on effective mass of electrons. We observed that with mono-

substitution of OH, the effective mass of ⟨100⟩ GeNW increases rapidly due to changing tendency of nature of band gap from indirect to direct. Once, the nature of band gap become direct, the effective mass of ⟨100⟩ GeNW decreases with the increase in OH coverage percentage. In contrast, the effective electron mass in the ⟨110⟩ OH-GeNWs increases with the increase in the OH coverage percentage on the nanowire surfaces. Our results also showed that the different orientations of the OH group and also the presence of surface state affect the effective mass of GeNWs. As smaller effective electron mass implies larger charge carrier mobility, thus, either increase or decrease of the charge carrier mobility in GeNWs will be observed with increasing OH passivation depending on the growth directions, with different alignments of OH group and in presence of surface states. Since the electrical conductivity is inversely proportional to effective mass of the electrons, the increase or decrease in effective electron mass will increase or decrease the electrical conductivity in the GeNWs. In conclusion, from our theoretical calculations, we attributed the causes of electrical hysteresis observed in GeNWs to (a) different amount of water being adsorbed, (b) alignments of the OH groups on the GeNWs surfaces; and (c) presence of trap state defects on the surface of the OH-GeNWs.

To investigate the surface defect induced electronic and magnetic properties of hydrogen passivated GeNWs, we have created the surface dangling bond (SDB) by removing the surface hydrogen atoms. To determine the electronic and magnetic properties, spin-polarizations are included in the calculations. Firstly we calculated the energy cost to create SDBs defects in GeNWs. We showed that the defects induced magnetic and electronic properties of GeNWs highly depend on the amount and the location of defects. Single SDB defected GeNWs remain semiconducting as its non-defected form while double or multiple SDB defects result either semiconducting or metallic. Based on the calculated net magnetic moments, double, quadruple and octuple SDB defected GeNWs can be divided into three

groups: (a) GeNWs with zero magnetic moments, (b) GeNWs with net magnetic moments equal to the number of SDBs, and (c) GeNWs with net magnetic moments significantly lower than the number of SDBs.

The band structure calculations showed that the SDB defects split the band structures into the spin-up and spin-down configurations. The majority of the studied surface defected GeNWs with anti-ferromagnetic configurations are semiconducting with the same spin-up and spin-down band gaps. In contrast, surface defected GeNWs with different spin-up and spin-down band structures are ferromagnetic. All the ferromagnetic GeNWs with net magnetic moment equal to the number of SDBs are semiconducting with distinct spin-up and spin-down band gaps. The GeNWs which undergo surface reconstruction via formation of Ge-Ge bonds have no free electron and become non-magnetic and have similar band structures like H-GeNWs. The GeNWs in which the magnetic moment is less than the number of SDBs are either metallic or semiconducting. However, the spin-up and spin-down band structures of these GeNWs are different. The calculated spin-polarization indicates that the spins are not confined but mixed. As a result, it significantly reduces the net magnetic moments in group (c). We also examined the effect of applying axial strain on GeNW with SDB defects and from which, we determine the possible half-metallic GeNW. Our results predicted that half-metallic GeNWs can be obtained from engineering their surface defects and structures without the presence of impurity dopants.

To study the interactions of molecules/radicals with single-walled carbon nanotubes (SWNTs) we have used chiral, zigzag and armchair SWNTs. We found that the 2-ethylantraquinone (EAQ) molecule does not bind to the semiconducting or metallic SWNTs with essentially zero binding energy. However, the OH· binds strongly with SWNTs and preferred the metallic SWNTs. We also found that the binding affinity of the OH· decreases with the increase in the diameter of tubes. Based on this study we concluded that the active

species responsible for the enrichment of semiconducting SWNTs are the radicals from EAQ. The interactions study of Br· radical with SWNTs showed that the interactions between Br· radical and all the SWNTs are in between chemisorption and physisorption. Our results showed that Br· radical has stronger interaction with metallic for both chiral and zigzag. The armchair SWNTs is special class of SWNTs which have only metallic nature. The binding affinities of Br· radical towards armchair SWNTs are less than the ones towards chiral and zigzag SWNTs and the binding affinities decrease with the increase in the diameter of tubes.

In conclusion, we achieved the following objectives set out at the beginning of this thesis –

(a) We revealed the structures and nature of bondings in germaallenes and also their stabilities and hyperconjugations.

(b) We revealed the formation mechanism of OH passivated GeNWs (OH-GeNWs) and contributed to understand the cause of experimentally observed electrical hysteresis in GeNW devices.

(c) We addressed the manipulation of electronic and magnetic properties of GeNWs by creating surface defects and predicted the half-metallic GeNWs.

(d) We contributed to understand the separation mechanism of metallic SWNTs from semiconducting SWNTs.

REFERENCES

1. Lu, W.; Lieber, C. M., Semiconductor nanowires. *J. Phys. D: Appl. Phys.* 2006, 39, R387–R406.
2. Hayden, O.; Agarwal, R.; Lu, W., Semiconductor nanowire devices. *Nanotoday* 2008, 3, 12-22.
3. Tans, S. J.; Verschueren, A. R. M.; Dekker, C., Room-temperature transistor based on a single carbon nanotube. *Nature* 1998, 393, 49-52.
4. Collins, P. C.; Arnold, M. S.; Avouris, P., Engineering carbon nanotubes and nanotube circuits using electrical breakdown. *Science* 2001, 292, 706-709.
5. Baughman, R. H.; Zakhidov, A. A.; de Heer, W. A., Carbon nanotubes - the route toward applications. *Science* 2002, 297, 787-792.
6. Morales, A. M.; Lieber, C. M., A Laser Ablation Method for the Synthesis of Crystalline Semiconductor Nanowires. *Science* 1998, 279, 208-211.

7. Park, S. K.; Hong, Y. K.; Lee, Y. B.; Bae, S. W.; Joo, J., Surface modification of Ni and Co metal nanowires through MeV high energy ion irradiation *Curr. Appl. Phys.* 2008, 9, 847-851.

8. Gu, Q.; Jin, H.; Dai, K., Fabrication of nickel and gold nanowires by controlled electrodeposition on deoxyribonucleic acid molecules. *Phys. D: Appl. Phys.* 2009, 42, 015303.

9. Jackson, H. E.; Perera, S.; Fickenscher, M. A.; Smith, L. M.; Yarrison-Rice, J. M.; Joyce, H. J.; Gao, Q.; Tan, H. H.; Jagadish, C.; Zhang, X.; Zou, J., Optical properties of single InP and GaAs nanowire heterostructures. *IEEE Lasers and Electro-Optics Society* 2008, 427 - 428

10. Lai, Y.-S.; Wang, J.-L.; Liou, S.-C.; Tu, C.-H., Size and density control of silicon oxide nanowires by rapid thermal annealing and their growth mechanism. *Appl. Phys. A* 2008, 94, 357-363.

11. Pipinys, P.; Sereika, R., Comment on 'Conductivity of single Mo6S9−xIx molecular nanowire bundles'. *Nanotechnology* 2007, 18, 508001.

12. Çakr, D.; Durgun, E.; Gülseren, O.; Ciraci, S., First principles study of electronic and mechanical properties of molybdenum selenide type nanowires. *Phys. Rev. B* 2006, 74, 235433.

13. Seeger, K., *Semiconductor Physics: An Introduction*. 9 ed.; Springer: New York, 2004.

14. Arantes, J. T.; Fazzio, A., Theoretical investigations of Ge nanowires grown along the [110] and [111] directions. *Nanotechnology* 2007, 18, 295706.

15. Yu, B.; Sun, X. H.; Calebotta, G. A.; Dholakia, G. R.; Meyyappan, M., One-dimensional germanium nanowires for future electronics. *J. Clust. Sc.* 2006, 17, 579-597.

16. Polyakov, B.; Daly, B.; Prikulis, J.; Lisauskas, V.; Vengalis, B.; Morris, M. A.; Holmes, J. D.; Erts, D., High-density arrays of germanium nanowire photoresistors. *Adv. Mater.* 2006, 18, 1812–1816.

17. Sze, S. M., *Physics of semiconductor devices*. Wiley-Interscience: 2007.

18. Harrison, W. A., *Electronic structure and the properties of solids: the physics of the chemical bond* Dover Publications: New York 1989.

19. Streetman, B. G., *Solid State electronic Devices*. 6th ed ed.; Pearson/Prentice Hall: New Jersey, 2006.

20. Mathur, S.; Shen, H.; Sivakov, V.; Werner, U., Germanium nanowires and core-shell nanostructures by chemical vapor deposition of [Ge(C5H5)(2)]. *Chem. Mater.* 2004, 16, 2449-2456.

21. Schricker, A. D.; Joshi, S. V.; Hanrath, T.; Banerjee, S. K.; Korgel, B. A., Temperature dependence of the field effect mobility of solution-grown germanium nanowires. *J. Phys. Chem. B* 2006, 110, 6816-6823.

22. Sutter, E.; Sutter, P., Au-induced encapsulation of Ge nanowires in protective C shells. *Adv. Mater.* 2006, 18, 2583–2588.

23. Hanrath, T.; Korgel, B. A., A comprehensive study of electron energy losses in Ge nanowires. *Nano Lett.* 2004, 4, 1455-1461.

24. Wu, Y. Y.; Yang, P. D., Germanium nanowire growth via simple vapor transport. *Chem.Mater.* 2000, 12, 605-607.

25. Gerung, H.; Boyle, T. J.; Tribby, L. J.; Bunge, S. D.; Brinker, C. J.; Han, S. M., Solution synthesis of germanium nanowires using a Ge^{2+} alkoxide precursor. *J.Am.Chem. Soc.* 2006, 128, 5244-5250.

26. Patibandla, S.; Pramanik, S.; Bandyopadhyaya, S.; Tepper, G. C., Spin relaxation in a germanium nanowire. *J. Appl. Phys.* 2006, 100, 044303.

27. Chan, C. K.; Zhang, X. F.; Cui, Y., High Capacity Li Ion Battery Anodes Using Ge Nanowires. *Nano Lett.* 2008, 8, 307-309.

28. Polyakov, B.; Daly, B.; Prikulis, J.; Lisauskas, V.; Vengalis, B.; Morris, M. A.; Holmes, J. D.; Erts, D., High-density arrays of germanium nanowire photoresistors. *Adv. Mater.* 2006, 18, 1812–1816.

29. Ahn, Y. H.; Park, J., Efficient visible light detection using individual germanium nanowire field effect transistors. *Appl. Phys. Lett.* 2007, 91, 162102.

30. Nguyen, P.; Ng, H. T.; Meyyappan, M., Growth of individual vertical germanium nanowires. *Adv. Mater.* 2005, 17, 549-553.

31. Hanrath, T.; Korgel, B. A., Chemical surface passivation of Ge nanowires. *J. Am. Chem. Soc.* 2004, 126, 15466-15472.

32. Hanrath, T.; Korgel, B. A., Nucleation and growth of germanium nanowires seeded by organic monolayer-coated gold nanocrystals. *J. Am. Chem. Soc.* 2002, 124, 1424-1429.

33. Wang, D.; Chang, Y.-L.; Liu, Z.; Dai, H., Oxidation Resistant Germanium Nanowires: Bulk Synthesis, Long Chain Alkanethiol Functionalization, and Langmuir-Blodgett Assembly. *J. Am. Chem. Soc.* 2005, 127, 11871-11875.

34. Hanrath, T.; Korgel, B. A., Supercritical fluid-liquid-solid (SFLS) synthesis of Si and Ge nanowires seeded by colloidal metal nanocrystals. *Adv. Mater.* 2003, 15, 437-440.

35. Wang, D. W.; Wang, Q.; Javey, A.; Tu, R.; Dai, H. J.; Kim, H.; McIntyre, P. C.; Krishnamohan, T.; Saraswat, K. C., Germanium nanowire field-effect transistors with SiO_2 and high-kappa HfO_2 gate dielectrics. *Appl. Phys. Lett.* 2003, 83, 2432-2434.

36. Tuan, H. Y.; Lee, D. C.; Hanrath, T.; Korgel, B. A., Germanium nanowire synthesis: An example of solid-phase seeded growth with nickel nanocrystals. *Chem. Mater.* 2005, 17, 5705-5711.

37. Hanrath, T.; Korgel, B. A., Influence of surface states on electron transport through intrinsic Ge nanowires. *J. Phys. Chem. B* 2005, 109, 5518-5524.

38. Wang, D.; Chang, Y.-L.; Wang, Q.; Cao, J.; Farmer, D. B.; Gordon, R. G.; Dai, H., Surface Chemistry and Electrical Properties of Germanium Nanowires. *J. Am. Chem. Soc.* 2004, 126, 11602-11611.

39. Wang, D. W., Synthesis and properties of germanium nanowires. *Pure Appl. Chem.* 2007, 79, 55-65.

40. Wang, D.; Dai, H., Germanium nanowires: from synthesis, surface chemistry, and assembly to devices. *Appl. Phys. A* 2006, 85, 217-225.

41. Wang, D. W.; Chang, Y. L.; Wang, Q.; Cao, J.; Farmer, D. B.; Gordon, R. G.; Dai, H. J., Surface chemistry and electrical properties of germanium nanowires. *J. Am. Chem. Soc.* 2004, 126, 11602-11611.

42. Ebbesen, T. W., Carbon nanotubes. Annu. *Rev. Mater Sci*. 1994, 24, 235-266.

43. Guo, T.; Nikolaev, P.; Thess, A.; Colbert, D. T.; Smalley, R. E., Self-Assembly of Tubular Fullerenes, *J. Phys. Chem. B* 1995, 99, 10694-10697.

44. Groning, O.; Kuttel, O. M.; Emmenegger, C.; Groning, P.; Schlapbach, L., Field emission properties of carbon nanotubes , *J. Vac. Sci. Technol*. B 2000, 18, 665-678.

45. Endo, M.; Takeuchi, K.; Igarashi, S.; Kobori, K.; Shiraishi, M.; Kroto, H. W., The production and structure of pyrolytic carbon nanotubes (PCNTs), *J. Phys. Chem.* Solids, 1993, 54, 1841-1848.

46. Hsu, W. K.; Hare, J. P.; Terrones, M.; Kroto, H. W.; Walton, D. R. M.; Harris, P. J. F., Condensed-phase nanotubes, *Nature* 1995, 377, 687.

47. Hsu, W. K.; Terrones, M.; Hare, J. P.; Terrones, H.; Kroto, H. W.; Walton, D. R. M., Electrolytic formation of carbon nanostructures, *Chem. Phys. Lett.* 1996, 262, 161-166.

48. Iijima, S., Helical microtubules of graphitic carbon, *Nature* 1991, 354, 56-58.

49. Iijima, S.; Ichihashi, T., Single-shell carbon nanotubes of 1-nm diameter, *Nature* 1993, 363, 603-605.

50. Bethune, D. S.; Kiang, C. H.; Vries, M. S. d.; Gorman, G.; Savoy, R.; Vazquez, J.; Beyers, R., Cobalt-catalysed growth of carbon nanotubes with single-atomic-layer walls, *Nature* 1993, 363, 605-607.

51. Krupke, R.; Hennrich, F.; von Lohneysen, H.; Kappes, M. M., Separation of metallic from semiconducting single-walled carbon nanotubes. *Science* 2003, 301, 344-347.

52. Krupke, R.; Hennrich, F.; Weber, H. B.; Kappes, M. M.; von Lohneysen, H., Simultaneous deposition of metallic bundles of single-walled carbon nanotubes using ac-dielectrophoresis. *Nano Lett.* 2003, 3, 1019-1023.

53. Krupke, R.; Linden, S.; Rapp, M.; Hennrich, F., Thin films of metallic carbon nanotubes prepared by dielectrophoresis. *Adv. Mater.* 2006, 18, 1468.

54. Maeda, Y.; Kimura, S.; Kanda, M.; Hirashima, Y.; Hasegawa, T.; Wakahara, T.; Lian, Y. F.; Nakahodo, T.; Tsuchiya, T.; Akasaka, T.; Lu, J.; Zhang, X. W.; Gao, Z. X.; Yu, Y. P.; Nagase, S.; Kazaoui, S.; Minami, N.; Shimizu, T.; Tokumoto, H.; Saito, R., Large-scale separation of metallic and semiconducting single-walled carbon nanotubes. *J. Am. Chem. Soc.* 2005, 127, 10287-10290.

55. Maeda, Y.; Kanda, M.; Hashimoto, M.; Hasegawa, T.; Kimura, S.; Lian, Y. F.; Wakahara, T.; Akasaka, T.; Kazaoui, S.; Minami, N.; Okazaki, T.; Hayamizu, Y.; Hata, K.; Lu, J.; Nagase, S., Dispersion and separation of small-diameter single-walled carbon nanotubes. *J. Am. Chem. Soc.* 2006, 128, 12239-12242.

56. Hersam, M. C., Progress towards monodisperse single-walled carbon nanotubes. *Nat. Nanotechnol.* 2008, 3, 387-394.

57. Tanaka, T.; Jin, H.; Miyata, Y.; Fujii, S.; Suga, H.; Naitoh, Y.; Minari, T.; Miyadera, T.; Tsukagoshi, K.; Kataura, H., Simple and Scalable Gel-Based Separation of Metallic and Semiconducting Carbon Nanotubes. *Nano Lett.* 2009, 9, 1497-1500.

58. Miyata, Y.; Maniwa, Y.; Kataura, H., Selective oxidation of semiconducting single-wall carbon nanotubes by hydrogen peroxide. *J. Phys. Chem. B* 2006, 110, 25-29.

59. Zheng, M.; Diner, B. A., Solution Redox Chemistry of Carbon Nanotubes. *J. Am. Chem. Soc.* 2004, 126, 15490-15494.

60. Zheng, M.; Jagota, A.; Semke, E. D.; Diner, B. A.; McLean, R. S.; Lustig, S. R.; Richardson, R. E.; Tassi, N. G., DNA-assisted dispersion and separation of carbon nanotubes. *Nat. Mater.* 2003, 2, 338-342.

61. Li, H. P.; Zhou, B.; Lin, Y.; Gu, L. R.; Wang, W.; Fernando, K. A. S.; Kumar, S.; Allard, L. F.; Sun, Y. P., Selective interactions of porphyrins with semiconducting single-walled carbon nanotubes. *J. Am. Chem. Soc.* 2004, 126, 1014-1015.

62. Wang, W.; Fernando, K. A. S.; Lin, Y.; Meziani, M. J.; Veca, L. M.; Cao, L.; Zhang, P.; Kimani, M. M.; Sun, Y. P., Metallic single-walled carbon nanotubes for conductive nanocomposites. *J. Am. Chem. Soc.* 2008, 130, 1415-1419.

63. Lee, C. W.; Han, X. D.; Chen, F. M.; Wei, J.; Chen, Y.; Chan-Park, M. B.; Li, L. J., Solution-Processable Carbon Nanotubes for Semiconducting Thin-Film Transistor Devices. *Adv. Mater.* 2009, 22, 1278.

64. Kanungo, M.; Lu, H.; Malliaras, G. G.; Blanchet, G. B., Suppression of Metallic Conductivity of Single-Walled Carbon Nanotubes by Cycloaddition Reactions. *Science* 2009, 323, 234-237.

65. Strano, M. S.; Dyke, C. A.; Usrey, M. L.; Barone, P. W.; Allen, M. J.; Shan, H. W.; Kittrell, C.; Hauge, R. H.; Tour, J. M.; Smalley, R. E., Electronic structure control of single-walled carbon nanotube functionalization. *Science* 2003, 301, 1519-1522.

66. Peng, X. B.; Komatsu, N.; Kimura, T.; Osuka, A., Improved optical enrichment of SWNTs through extraction with chiral nanotweezers of 2,6-pyridylene-bridged diporphyrins. *J. Am. Chem. Soc.* 2007, 129, 15947-15953.

67. MØller, C.; Plesset, M. S., Note on an Approximation Treatment for Many-Electron Systems, *Phys. Rev.* 1934, 46, 618-622.

68. Pople, J. A.; Binkley, J. S.; Seeger, R., Closed shell 2nd order Moller-Plesset and MP2 gradient, *Int. J. Quantum Chem.* 1976, 10, 1.

69. Cizek, J., *Adv. Chem. Phys.* 1969, 14, 35.

70. Purvis, G. D.; Bartlett, R. J., A full coupled-cluster singles and doubles model: The inclusion of disconnected triples, *J. Chem. Phys.* 1982, 76, 1910-1918.

71. Scuseria, G. E.; Janssen, C. L.; Schaefer III, H. F., An efficient reformulation of the closed-shell coupled cluster single and double excitation (CCSD) equations, *J. Chem. Phys.* 1988, 89, 7382-7387.

72. Scuseria, G. E.; Schaefer III, H. F., Is coupled cluster singles and doubles (CCSD) more computationally intensive than quadratic configuration interaction (QCISD)? *J. Chem. Phys.* 1989, 90, 3700-3703.

73. Hohenberg, P.; Kohn, W., Inhomogeneous electron gas. *Phys. Rev. B* 1964, 136, 864-871.

74. Kohn, W.; Sham, L. J., Self-consistent equations including exchange and correlation effects. *Phys. Rev. A* 1965, 140, 1133-1138.

75. Levine, I. N., *Quantum Chemistry*. 4th ed.; Prentice Hall: New Jersey, 2000.

76. Koch, W.; Holthausen, M. C., *A Chemist's Guide to Density Functional Theory*. Wiley-VCH: New York, 2002.

77. Young, D. C., *Computational Chemistry: A Practical Guide for Applying Techniques to Real-World Problems*. John Wiley & Sons, Inc: New York, 2001.

78. Feller, D., An ab initio study of the magnetic hyperfine properties of $F_2^-(^2\Sigma_u^+)$ *J. Chem. Phys.* 1990, 93, 579-589.

79. Becke, A. D., Density-functional thermochemistry. III. The role of exact exchange, *J. Chem. Phys.* 1993, 98, 5648-5652.

80. Lee, C.; Yang, W.; Parr, R. G., Development of the Colle-Salvetti correlation-energy formula into a functional of the electron density, *Phys. Rev. B* 1988, 37, 785-789.

81. Frisch, M. J. e. a., *Gaussian 03, Revision B.05; Gaussian, Inc., Pittsburgh PA* 2003 (*see Appendix A for full citation*).

82. Glendening, E. D.; Reed, A. E.; Carpenter, J. E.; Weinhold, F., *NBO Version 3.1*.

83. Perdew, J. P.; Burke, K.; Ernzerhof, M., Generalized Gradient Approximation Made Simple. *Phys. Rev. Lett.* 1996, 77, 3865-3868.

84. Kresse, G.; Furthmuller, J., Efficient iterative schemes for ab initio total-energy calculations using a plane-wave basis set. *Phys. Rev. B* 1996, 54, 11169-11186.

85. Kresse, G.; Furthmüller, J., Efficiency of ab initio total-energy calculations for metals and semiconductors using a plane-wave basis set. *J. Comp. Mat. Sci.* 1996, 6, 15-50.

86. Kresse, G.; Hafner, J., Ab initio molecular dynamics for open-shell transition metals. *Phys. Rev. B* 1993, 48, 13115-13118.

87. Blochl, P. E., Projector augmented-wave method. *Phys. Rev. B* 1994, 50, 17953.

88. Kresse, G.; Joubert, D., From ultrasoft pseudopotentials to the projector augmented-wave method. *Phy. Rev. B* 1999, 59, 1758-1775.

89. Monkhorst, H. J.; Pack, J. D., Special points for Brillouin-zone integrations, *Phy. Rev. B* 1976, 13, 5188-5192.

90. Chattopadhyay, D.; Rakshit, P. C., *Electronics (fundamentals And Applications)*. New Age International: New Delhi, 2006.

91. Logan, P.; Peng, X., Strain-modulated electronic properties of Ge nanowires: A first-principles study. *Phys. Rev. B* 2009, 80, 115322.

92. Harrison, W. A., *Elementary Electronic structure*. Revised Edition ed.; World Scientific Publishing Co. Pte. Ltd.: London, 2004.

93. Heath, J. R.; LeGoues, F. K., A liquid solution synthesis of single crystal germanium quantum wires. *Chem. Phys. Lett.* 1993, 208, 263-268.

94. Lew, K. K.; Pan, L.; Dickey, E. C.; Redwing, J. M., Vapor-liquid-solid growth of silicon-germanium nanowires. *Adv. Mater.* 2003, 15, 2073-2076.

95. Dailey, J. W.; Taraci, J.; Clement, T.; Smith, D. J.; Drucker, J.; Picraux, S. T., Vapor-liquid-solid growth of germanium nanostructures on silicon. *J. Appl. Phys.* 2004, 96, 7556-7567.

96. Greytak, A. B.; Lauhon, L. J.; Gudiksen, M. S.; Lieber, C. M., Growth and transport properties of complementary germanium nanowire field-effect transistors. *Appl. Phys. Lett.* 2004, 84, 4176-4178.

97. Redwing, J. M.; Lew, K. K.; Bogart, T. E.; Pan, L.; Dickey, E. C.; Carim, A. H.; Wang, Y. F.; Cabassi, M. A.; Mayer, T. S. In *Synthesis and properties of Si and SiGe/Si nanowires*, Conference on Quantum Dots, Nanoparticles, and Nanoclusters, San Jose, CA, Huffaker, D. L.; Bhattacharya, P., Eds. San Jose, CA, 2004; pp 52-59.

98. Lew, K. K.; Pan, L.; Dickey, E. C.; Redwing, J. M., Effect of growth conditions on the composition and structure of $Si_{1-x}Ge_x$ nanowires grown by vapor-liquid-solid growth. *J. Mater. Res.* 2006, 21, 2876-2881.

99. Kodambaka, S.; Tersoff, J.; Reuter, M. C.; Ross, F. M., Germanium nanowire growth below the eutectic temperature. *Science* 2007, 316, 729-732.

100. Sun, X. H.; Calebotta, G.; Yu, B.; Selvaduray, G.; Meyyappan, M., Synthesis of germanium nanowires on insulator catalyzed by indium or antimony. *J. Vac. Sc. Technol. B* 2007, 25, 415-420.

101. Lauhon, L. J.; Gudiksen, M. S.; Wang, C. L.; Lieber, C. M., Epitaxial core-shell and core-multishell nanowire heterostructures. *Nature* 2002, 420, 57-61.

102. Adhikari, H.; Marshall, A. F.; Chidsey, C. E. D.; McIntyre, P. C., Germanium nanowire epitaxy: Shape and orientation control. *Nano Lett.* 2006, 6, 318-323.

103. Tutuc, E.; Appenzeller, J.; Reuter, M. C.; Guha, S., Realization of a linear germanium nanowire p-n junction. *Nano Lett.* 2006, 6, 2070-2074.

104. Adhikari, H.; Marshall, A. F.; Goldthorpe, I. A.; Chidsey, C. E. D.; McIntyre, P. C., Metastability of Au-Ge liquid nanocatalysts: Ge vapor-liquid-solid nanowire growth far below the bulk eutectic temperature. *Acs Nano* 2007, 1, 415-422.

105. Zhang, L.; Tu, R.; Dai, H. J., Parallel core-shell metal-dielectric-semiconductor germanium nanowires for high-current surround-gate field-effect transistors. *Nano Lett.* 2006, 6, 2785-2789.

106. Kim, Y.; Song, M. S.; Kim, Y. D.; Jung, J. H.; Gao, Q.; Tan, H. H.; Jagadish, C., Epitaxial germanium nanowires on GaAs grown by chemical vapor deposition. *J. Korean Phys. Soc.* 2007, 51, 120-124.

107. Chen, X.; Kim, M. H.; Zhang, X.; Larson, C.; Yu, D.; Wodtke, A. M.; Moskovits, M., Oriented growth of Ge nanowires with diameters below the Bohr radius. *J. Phys. Chem. C* 2008, 112, 13797-13800.

108. Hanrath, T.; Korgel, B. A. In *Quantum confinement effects in germanium nanowires studied by electron energy loss spectroscopy (EELS)*, Conference on Physical Chemistry of Interfaces and Nanomaterials III, Denver, CO, Aug 03-06; Hartland, G. V.; Zhu, X. Y., Eds. Denver, CO, 2004; pp 40-47.

109. Yoo, B.; Dodabalapur, A.; Lee, D. C.; Hanrath, T.; Korgel, B. A., Germanium nanowire transistors with ethylene glycol treated poly(3,4-ethylenedioxythiophene): poly(styrene sulfonate) contacts. *Appl. Phys. Lett.* 2007, 90, 072106.

110. Mathur, S.; Shen, H.; Werner, U. In *Low temperature gas phase synthesis of germanium nanowires*, Symposium on Quantum Dots, Nanoparticles and Nanowires held at the 2003 MRS Fall Meeting, Boston, MA, Dec 01-05; GuyotSionnest, P.; Mattoussi, H.; Wang, Z. L., Eds. Boston, MA, 2003; pp 377-382.

111. Jagannathan, H.; Deal, M.; Nishi, Y.; Kim, H. C.; Freer, E. M.; Sundstrom, L.; Topuria, T.; Rice, P. M., Templated germanium nanowire synthesis using oriented mesoporous organosilicate thin films. *J. Vac. Sc. Technol. B* 2006, 24, 2220-2224.

112. Wang, F. D.; Dong, A. G.; Sun, J. W.; Tang, R.; Yu, H.; Buhro, W. E., Solution-liquid-solid growth of semiconductor nanowires. *Inorg. Chem.* 2006, 45, 7511-7521.

113. Huang, Q.; Deligianni, H.; Romankiw, L. T., Anisotropic growth of nanostructures in germanium electroplating. *Electrochem.Solid State Letters* 2007, 10, D121-D123.

114. Muller, T.; Heining, K. H.; Schmidt, B., Formation of Ge nanowires in oxidized silicon V-grooves by ion beam synthesis. *Nuclear Instruments and Methods in Physics Research B* 2001, 468, 175-177.

115. Wang, D.; Dai, H., Low-Temperature Synthesis of Single-Crystal Germanium Nanowires by Chemical Vapor Deposition. *Angew. Chem. Int. Ed.* 2002, 41, 4783.

116. Wang, D. W.; Tu, R.; Zhang, L.; Dai, H. J., Deterministic one-to-one synthesis of germanium nanowires and individual gold nanoseed patterning for aligned arrays. *Angew. Chem. Int. Ed.* 2005, 44, 2925-2929.

117. Fang, C.; Foll, H.; Carstensen, J., Long Germanium Nanowires Prepared by Electrochemical Etching. *Nano Lett.* 2007, 6, 1578.

118. Lensch-Falk, J. L.; Hemesath, E. R.; Lopez, F. J.; Lauhon, L. J., Vapor-Solid-Solid Synthesis of Ge Nanowires from Vapor-Phase-Deposited Manganese Germanide Seeds. *J. Am. Chem. Soc.* 2007, 129, 10670.

119. Huang, Y.; Lin, J.; Zhang, J.; Ding, X. X.; Qi, S. R.; Tang, C. C., A novel method for preparing carbon-coated germanium nanowires. *Nanotechnology* 2005, 16, 1369–1371.

120. Adhikari, H.; McIntyre, P. C.; Sun, S. Y.; Pianetta, P.; Chidsey, C. E. D., Photoemission studies of passivation of germanium nanowires. *Appl. Phys. Lett.* 2005, 87, 263109.

121. Whang, S. J.; Lee, S. J.; Yang, W. F.; Cho, B. J.; Kwong, D. L., Study on the synthesis of high quality single crystalline $Si_{1-x}Ge_x$ nanowire and its transport properties. *Appl. Phys. Lett.* 2007, 91, 072105.

122. Goldthorpe, I. A.; Marshall, A. F.; McIntyre, P. C., Synthesis and Strain Relaxation of Ge-Core/Si-Shell Nanowire Arrays. *Nano Lett.* 2008, 8, 4081-4086.

123. Sun, X.; Calebotta, G.; Yu, B.; Selvaduray, G.; Meyyappan, M., Synthesis of germanium nanowires on insulator catalyzed by indium or antimony. *J. Vac. Sci. Technol. B* 2007, 25, 415-420.

124. Kazakova, O.; Kulkarni, J. S.; Holmes, J. D.; Demokritov, S. O., Room-temperature ferromagnetism in $Ge_{1-x}Mn_x$ nanowires. *Phys. Rev. B* 2005, 72, 094415.

125. Patibandla, S.; Pramanik, S.; Bandyopadhyaya, S.; Tepper, G. C., Spin relaxation in a germanium nanowire. *J. Appl. Phys.* 2006, 100, 044303.

126. Chan, C. K.; Zhang, X. F.; Cui, Y., High Capacity Li Ion Battery Anodes Using Ge Nanowires. *Nano Lett.* 2008, 8, 307-309.

127. Ryan, K. M.; Erts, D.; Olin, H.; Morris, M. A.; Holmes, J. D., Three dimensional architectures of ultra-high density semiconducting nanowires deposited on chip. *J. Am. Chem. Soc.* 2003, 125, 6284-6288.

128. Audoit, G.; Ni Mhuircheartaigh, T.; Lipson, S. M.; Morris, M. A.; Blau, W. J.; Holmes, J. D., Strain induced photoluminescence from silicon and germanium nanowire arrays. *J. Mater. Chem.* 2005, 15, 4809-4815.

129. Ziegler, K. J.; Polyakov, B.; Kulkarni, J. S.; Crowley, T. A.; Ryan, K. M.; Morris, M. A.; Erts, D.; Holmes, J. D., Conductive films of ordered nanowire arrays. *J. Mater. Chem.* 2004, 14, 585-589.

130. Erts, D.; Polyakov, B.; Dalyt, B.; Morris, M. A.; Ellingboe, S.; Boland, J.; Holmes, J. D., High density germanium nanowire assemblies: Contact challenges and electrical characterization. *J. Phys. Chem. B* 2006, 110, 820-826.

131. Ahn, Y. H.; Park, J., Efficient visible light detection using individual germanium nanowire field effect transistors. *Appl. Phys. Lett.* 2007, 91, 162102.

132. Nguyen, P.; Ng, H. T.; Meyyappan, M., Growth of individual vertical germanium nanowires. *Adv. Mater.* 2005, 17, 549-553.

133. Ziegler, K. J.; Lyons, D. M.; Holmes, J. D.; Erts, D.; Polyakov, B.; Olin, H.; Svensson, K.; Olsson, E., Bistable nanoelectromechanical devices. *Appl. Phys. Lett.* 2004, 84, 4074-4076.

134. Javey, A.; Nam, S.; Friedman, R. S.; Yan, H.; Lieber, C. M., Layer-by-layer assembly of nanowires for three-dimensional, multifunctional electronics. *Nano Lett.* 2007, 7, 773-777.

135. Toh, E. H.; Wang, G. H.; Zhu, M.; Shen, C.; Chan, L.; Lo, G. Q.; Tung, C. H.; Sylvester, D.; Heng, C. H.; Samudra, G.; Yeo, Y. C.; Ieee In *Impact Ionization Nanowire Transistor with Multiple-gates, Silicon-Germanium Impact Ionization*

Region, and sub-5 mV/decade subtheshold swing, IEEE International Electron Devices Meeting, Washington, DC, Dec 10-12; Washington, DC, 2007; pp 195-198.

136. Whang, S. J.; Lee, S. J.; Yang, W. F.; Cho, B. J.; Liew, Y. F.; Kwong, D. L. In *Synthesis and transistor performances of high quality single crystalline vapor-liquid-solid grown $Si_{1-x}Ge_x$ nanowire*, 7th IEEE Conference on Nanotechnology, Hong Kong, PEOPLES R CHINA, Aug 02-05; Hong Kong, PEOPLES R CHINA, 2007; pp 45-48.

137. Feng, J.; Thareja, G.; Kobayashi, M.; Chen, S.; Poon, A.; Bai, Y.; Griffin, P. B.; Wong, S. S.; Nishi, Y.; Plummer, J. D., High-performance gate-all-around GeOI p-MOSFETs fabricated by rapid melt growth using plasma nitridation and ALD Al2O3 gate dielectric and self-aligned NiGe contacts. *IEEE Electron Device Letters* 2008, 29, 805-807.

138. Tu, R.; Zhang, L.; Nishi, Y.; Dai, H. J., Measuring the capacitance of individual semiconductor nanowires for carrier mobility assessment. *Nano Lett.* 2007, 7, 1561-1565.

139. Yang, J. E.; Jin, C. B.; Kim, C. J.; Jo, M. H., Band-gap modulation in single-crystalline Si1-xGex nanowires. *Nano Lett.* 2006, 6, 2679-2684.

140. Muller, T.; Heinig, K.-H.; Schmidt, B., Formation of Ge nanowires in oxidized silicon V-grooves by ion beam synthesis. *Nuclear Instruments and Methods in Physics Research B* 2001, 175-177, 468-473.

141. Sunkara, M. K.; Mulpuri, R.; Ragade, R. In *Kinetic Monte-Carlo simulations of nanowire growth*, AIChE Annual Meeting, Conference Proceedings, 2005; p 11148.

142. Kagimura, R.; Nunes, R. W.; Chacham, H., Structures of Si and Ge nanowires in the subnanometer range. *Phys. Rev. Lett.* 2005, 95, 115502.

143. Arantes, J. T.; da Silva, A. J. R.; Fazzio, A., Structural, electronic, and magnetic properties of Mn-doped Ge nanowires by ab initio calculations. *Phys. Rev. B* 2007, 75, 115113.

144. Migas, D. B.; Borisenko, V. E., Structural, electronic, and optical properties of <001> -oriented SiGe nanowires. *Phys. Rev. B* 2007, 76, 035440.

145. Stekolnikov, A. A.; FurthmuÌˆller, J.; Bechstedt, F., Pt-induced nanowires on Ge(001): Ab initio study. *Phys. Rev. B* 2008, 78, 155434.

146. Liu, W. L.; Zhang, K. W.; Xiao, H. P.; Meng, L. J.; Li, J.; Stocks, G. M.; Zhong, J. X., Surface reconstruction and core distortion of silicon and germanium nanowires. *Nanotechnology* 2007, 18, 215703.

147. Kholod, A. N.; Shaposhnikov, V. L.; Sobolev, N.; Borisenko, V. E.; D'Avitaya, F. A.; Ossicini, S., Orientation effects in the electronic and optical properties of germanium quantum wires. *Phys. Rev. B* 2004, 70, 035317.

148. Beckman, S. P.; Han, J.; Chelikowsky, J. R., Quantum confinement effects in Ge [110] nanowires. *Phys. Rev. B* 2006, 74, 165314.

149. Harris, C.; O'Reilly, E. P., Nature of the band gap of silicon and germanium nanowires. *Physica E* 2006, 32, 341-345.

150. Jing, M. W.; Ni, M.; Song, W.; Lu, J.; Gao, Z. X.; Lai, L.; Mei, W. N.; Yu, D. P.; Ye, H. Q.; Wang, L., Anisotropic and passivation-dependent quantum confinement effects in germanium nanowires: A comparison with silicon nanowires. *J. Phys. Chem. B* 2006, 110, 18332-18337.

151. Musin, R. N.; Wang, X. Q., Quantum size effect in core-shell structured silicon-germanium nanowires. *Phys. Rev. B* 2006, 74, 165308.

152. Akman, N.; Durgun, E.; Cahangirov, S.; Ciraci, S., Confined states in multiple quantum well structures of Sin Gen nanowire superlattices. *Phys. Rev. B* 2007, 76, 245427.

153. Medaboina, D.; Gade, V.; Patil, S. K. R.; Khare, S. V., Effect of structure, surface passivation, and doping on the electronic properties of Ge nanowires: A first-principles study. *Phys. Rev. B* 2007, 76, 205327.

154. Bruno, M.; Palummo, M.; Ossicini, S.; Del Sole, R., First-principles optical properties of silicon and germanium nanowires. *Surf. Sci.* 2007, 601, 2707-2711.

155. Dames, C.; Chen, G., Theoretical phonon thermal conductivity of Si/Ge superlattice nanowires. *J. Appl. Phys.* 2004, 95, 682-693.

156. Yang, R. G.; Chen, G., Thermal conductivity modeling of periodic two-dimensional nanocomposites. *Phys. Rev. B* 2004, 69, 195316.

157. Yang, R. G.; Chen, G.; Dresselhaus, M. S., Thermal conductivity of simple and tubular nanowire composites in the longitudinal direction. *Phys. Rev. B* 2005, 72, 125418.

158. Decker, B.; Schelling, P. K.; Phillpot, S. R., Interfacial phonon scattering in semiconductor nanowires by molecular-dynamics simulation. *J. Appl. Phys.* 2006, 99.

159. Jalilian, R.; Sumanasekera, G. U.; Chandrasekharan, H.; Sunkara, M. K., Phonon confinement and laser heating effects in Germanium nanowires. *Phys. Rev. B* 2006, 74, 155421.

160. Lu, X.; Chu, J., Lattice thermal conductivity in a Si/Ge/Si heterostructure. *J. Appl. Phys.* 2007, 101, 114323.

161. Tian, W. X.; Yang, R. G., Thermal conductivity modeling of compacted nanowire composites. *J. Appl. Phys.* 2007, 101, 054320.

162. Wang, J.; Wang, J. S., Dimensional crossover of thermal conductance in nanowires. *Appl. Phys. Lett.* 2007, 90, 241908.

163. Jeng, M. S.; Yang, R. G.; Song, D.; Chen, G., Modeling the thermal conductivity and phonon transport in nanoparticle composites using Monte Carlo simulation. *J. Heat Transfer* 2008, 130, 042410.

164. Zhang, Y.; Xiao, Y., Lattice dynamics investigations of SiGe core-shell nanowires. *Eur. Phys. J. B* 2008, 63, 425-430.

165. Pang, Q.; Zhang, Y.; Zhang, J.-M.; Xu, K.-W., Mater. Chem. Phys. 2010, 124, 1113-1120.

166. Mingo, N.; Yang, L., Phonon transport in nanowires coated with an amorphous material: An atomistic Green's function approach. *Phys. Rev. B* 2003, 68, 245406.

167. O'Connell, M. J., *Carbon Nanotubes: Properties and Applications*. Taylor & Francis Group: 2006.

168. Mintmire, J. W.; Dunlap, B. I.; White, C. T., Are fullerene tubules metallic? . *Phys. Rev. Lett.* 1992, 68, 631.

169. Hong, S.; Myung, S., Nanotube Electronics: A flexible approach to mobility. *Nature Nanotech.* 2007, 2, 207-208.

170. Dai, H. J., Carbon Nanotubes: Synthesis, Integration, and Properties. *Acc. Chem. Res.* 2002, 35, 1035-1044.

171. Salalha, W.; Dror, Y.; Khalfin, R. L.; Cohen, Y.; Yarin, A. L.; Zussman, E., Single-Walled Carbon Nanotubes Embedded in Oriented Polymeric Nanofibers by Electrospinning. *Langmuir* 2004, 20, 9852-9855.

172. Hafner, J. H.; Cheung, C. L.; Oosterkamp, T. H.; Lieber, C. M., High-Yield Assembly of Individual Single-Walled Carbon Nanotube Tips for Scanning Probe Microscopies. *J. Phys. Chem. B* 2001, 105, 743-746.

173. Wang, Y.; Da, S.; Kim, M. J.; Kelly, K. F.; Guo, W.; Kittrell, C.; Hauge, R. H.; Smalley, R. E., Ultrathin "Bed-of-Nails" Membranes of Single-Wall Carbon Nanotubes. *J. Am. Chem. Soc*. 2004, 126, 9502-9503.

174. Martel, R.; Schmidt, T.; Shea, H. R.; Hertel, T.; Avouris, P., Single- and multi-wall carbon nanotube field-effect transistors. *Appl. Phys. Lett.* 1998, 73, 2447-2449.

175. Kocabas, C.; Kang, S. J.; Ozel, T.; Shim, M.; Rogers, J. A., Improved Synthesis of Aligned Arrays of Single-Walled Carbon Nanotubes and Their Implementation in Thin Film Type Transistors. *J. Phys. Chem. C* 2007, 111, 17879-17886.

176. Lee, C. H.; Kang, K. T.; Park, K. S.; Kim, M. S.; Kim, H. S.; Kim, H. G.; Fischer, J. E.; Johnson, A. T., The Nano-Memory Devices of a Single Wall and Peapod Structural Carbon Nanotube Field Effect Transistor. *Japanese J. Appl. Phys.* 2003, 42, 5392-5394.

177. Someya, T.; Small, J.; Kim, P.; Nuckolls, C.; Yardley, J. T., Alcohol Vapor Sensors Based on Single-Walled Carbon Nanotube Field Effect Transistors. *Nano Lett.* 2003, 3, 877-881.

178. Choi, W. B.; Chung, D. S.; Kang, J. H.; Kim, H. Y.; Jin, Y. W.; Han, I. T.; Lee, Y. H.; Jung, J. E.; Lee, N. S.; Park, G. S.; Kim, J. M., Fully sealed, high-brightness carbon-nanotube field-emission display. *Appl. Phys. Lett.* 1999, 75, 3129-3131.

179. Liu, T.; Sreekumar, T. V.; Kumar, S.; Hauge, R. H.; Smalley, R. E., SWNT/PAN composite film-based supercapacitors. *Carbon* 2003, 41, 2440-2442.

180. Aurelien Du, P.; Husnu Emrah, U.; Alokik, K.; Steve, M.; Manish, C., Conducting and transparent single-wall carbon nanotube electrodes for polymer-fullerene solar cells. *Appl. Phys. Lett.* 2005, 87, 203511.

181. Welsher, K.; Liu, Z.; Daranciang, D.; Dai, H. J., Selective Probing and Imaging of Cells with Single Walled Carbon Nanotubes as Near-Infrared Fluorescent Molecules. *Nano Lett.* 2008, 8, 586-590.

182. Singh, R.; Pantarotto, D.; McCarthy, D.; Chaloin, O.; Hoebeke, J.; Partidos, C. D.; Briand, J. P.; Bianco, A.; Kostarelos, K., Binding and Condensation of Plasmid DNA onto Functionalized Carbon Nanotubes: Toward the Construction of Nanotube-Based Gene Delivery Vectors. *J. Am. Chem. Soc.* 2005, 127, 4388-4396.

183. Azizi, K.; Hashemianzadeh, S. M.; Bahramifar, S., Density functional theory study of carbon monoxide adsorption on the inside and outside of the armchair single-walled carbon nanotubes. *Curr. Appl. Phys.* 2011, 11, 776-782.

184. Woods, L. M.; Bădescu, Ş. C.; Reinecke, T. L., Adsorption of simple benzene derivatives on carbon nanotubes. *Phys. Rev. B* 2007, 75, 155415.

185. Shirvani, B. B.; Beheshtian, J.; Esrafili, M. D.; Hadipour, N. L., DFT study of NH_3 adsorption on the (5,0), (8,0), (5,5) and (6,6) single-walled carbon nanotubes. Calculated binding energies, NMR and NQR parameters, *Physica B* 2010, 405, 1455-1460.

186. Park, N.; Miyamoto, Y.; Lee, K.; Choi, W. I.; Ihm, J.; Yu, J.; Han, S., Band gap sensitivity of bromine adsorption at carbon nanotubes, *Chem. Phys. Lett.* 2005, 403, 135-139.

187. Baei, M. T.; Sayyed-Alangi, S. Z.; Soltani, A.; Bahari, M.; Masoodi, A., Adsorption properties of OCN radical on (6,0), (8,0), and (10,0) zigzag single-walled carbon nanotubes: a density functional study. *Monatsh. Chem.* 2011, 142, 1-4.

188. Yagi, Y.; Briere, T. M.; Sluiter, M. H. F.; Kumar, V.; Farajian, A. A.; Kawazoe, Y., Stable geometries and magnetic properties of single-walled carbon nanotubes doped with 3d transition metals: A first-principles study, *Phys. Rev. B* 2004, 69, 075414.

189. Durgun, E.; Dag, S.; Bagci, V. M. K.; Gulseren, O.; Yildirim, T.; Ciraci, S., Systematic study of adsorption of single atoms on a carbon nanotube, *Phys. Rev. B* 2003, 67, 201401.

190. Chen, G.; Kawazoe, Y., Interaction between a single Pt atom and a carbon nanotube studied by density functional theory, *Phys. Rev. B* 2006, 73, 125410.

191. Gao, H.; Zhao, J., First-principles study of Ru atoms and clusters adsorbed outside and inside carbon nanotubes *J. Chem. Phys.* 2010, 132, 234704.

192. Inntam, C.; Limtrakul, J., Adsorption of M Species and M2 Dimers (M) Cu, Ag, and Au) on the Pristine and Defective Single-Walled Carbon Nanotubes: A Density Functional Theory Study. *J. Phys. Chem. C* 2010, 114, 21327-21337.

193. Wang, H.; Xu, J., Theoretical evidence for a two-step mechanism in the functionalization single-walled carbon nanotube by aryl diazonium salts: Comparing effect of different substituent group, *Chem. Phys. Lett.* 2009, 477, 176-178.

194. Miracle, G. E.; Ball, J. L.; Powell, D. R.; West, R., The First Stable 1-Silaallen. *J. Am. Chem. Soc.* 1993, 115, 11598-11599.

195. Trommer, M.; Miracle, G. E.; Eichler, B. E.; Powell, D. R.; West, R., Synthesis and Reactivity of Several Stable 1-Silaallenes. *Organometallics* 1997, 16, 5737-5747.

196. Ishida, S.; T, I.; Kabuto, C.; Kira, M., A stable silicon-based allene analogue with a formally sp-hybridized silicon atom. *Nature* 2003, 421, 725-727.

197. Iwamoto, T.; Abe, T.; Ishida, S.; Kabuto, C.; Kira, M., Reactions of trisilaallene and 2-germadisilaallene with various reagents. *J.Organomet. Chem.* 2007, 692, 263-270.

198. BartheIat, J.-C.; Trinquier, G.; Bertrand, G., Theoretical Investigations on Some C_2SiH_4 Isomers. *J. Am. Chem. Soc.* 1979, 101, 3785-3789.

199. Veszpremi, T.; Petrov, K.; Nguyen, C. T., From Silaallene to Cyclotrisilanylidene. *Organometallics* 2006, 25, 1480-1484.

200. Kosa, M.; Karni, M.; Apeloig, Y., Trisilaallene and the Relative Stability of Si_3H_4 Isomers. *J. Chem. Theory Comput.* 2006, 2, 956-964.

201. Eichler, B. E.; Powell, D. R.; West, R., Synthesis and Structure of a 1-Germapropadiene. *Organometallics* 1998, 17, 2147-2148.

202. Tokitoh, N.; Kishikawa, K.; Okazaki, R., Synthesis and Reactions of the First Stable 1-Germaallene. *Chem. Lett.* 1998, 811-812.

203. Kishikawa, K.; Tokitoh, N.; Okazaki, R., Synthesis And Reactions Of The First Stable 1-Germaallene 1,2-Telluride And Its Sulfur And Selenium Analogues. *Phosphorus, Sulfur, and Silicon and the Related Elements* 1998, 136-138, 505-508.

204. Tokitoh, N.; Kishikawa, K.; Okazaki, R., Synthesis and Reactions of a 1-Germaallene Kinetically Stabilized by 2,4,6-Tris[Bis(Trimethylsilyl)Methyl]Phenyl Group. *Phosphorus, Sulfur, and Silicon and the Related Elements* 1999, 150-151, 137-143.

205. Eichler, B. E.; Powell, D. R.; West, R., Reactivity of a 1-Germapropadiene. *Organometallics* 1999, 18, 540-545.

206. Iwamoto, T.; Masuda, H.; Kabuto, C.; Kira, M., Trigermaallene and 1,3-Digermasilaallene. *Organometallics* 2005, 24, 197-199.

207. Sigal, N.; Apeloig, Y., Theoretical Study of Heavier Group 14 Analogues of Allene. *Organometallics* 2002, 21, 5486-5493.

208. Kosa, M.; Karni, M.; Apeloig, Y., How to Design Linear Allenic-Type Trisilaallenes and Trigermaallenes. *J. Am. Chem. Soc.* 2004, 126, 10544-10545.

209. Iwamoto, T.; Abe, T.; Kabuto, C.; Kira, M., A missing allene of heavy Group 14 elements: 2-germadisilaallene. *Chem. Commun.* 2005, 5190-5192.

210. Hehre, W. J.; Radom, L.; Schleyer, P. v. R.; Pople, J. A., *Ab Initio Molecular Orbital Theory*. Wiley: New York, 1986.

211. Xi, H.-W.; Karni, M.; Y., A., Silabutadienes. Internal Rotations and π-Conjugation. A Density Functional Theory Study. *J. Phys. Chem. A* 2008, 112, 13066-13079.

212. Xi, H.-W.; Lim, K. H., Theoretical Study of Germabutadienic Internal Rotations and π-Conjugation. *Organmetallics* 2008, 27, 5748-5758.

213. Sk, M. A.; Xi, H.-W.; Lim, K. H., Structure, Bonding and Hyperconjugation of Germaallene: A Theoretical Study. *Organometallics* 2009, 28, 3678-3685.

214. Wiberg, K. B., Application of the pople-santry-segal CNDO method to the cyclopropylcarbinyl and cyclobutyl cation and to bicyclobutane. *Tetrahedron* 1968, 24, 1083-1096.

215. Trinquier, G.; Malrieu, J.-P., Nonclassical Distortions at Multiple Bonds. *J. Am. Chem. Soc.* 1987, 109, 5303-5315.

216. Malrieu, J.-P.; Trinquier, G., Trans Bending at Double Bonds. Occurrence and Extent. *J. Am. Chem. Soc.* 1989, 111, 5916-5921.

217. Trinquier, G.; Malrieu, J.-P., Trans Bendkrg at Double Bonds. Scrutiny of Various Rationales through Valence-Bond Analysis. *J. Phys. Chem. A* 1990, 94, 6184-6196.

218. Trinquier, G., Double Bonds and Bridged Structures in the Heavier Analogues of Ethylene. *J. Am. Chem. Soc.* 1990, 112, 2130-2131.

219. Fernández, I.; Frenking, G., Direct Estimate of the Strength of Conjugation and Hyperconjugation by the Energy Decomposition Analysis Method. *Chem. Eur. J.* 2006, 12, 3617-3629.

220. Cappel, D.; Tüllmann, S.; Krapp, A.; G., F., Direct Estimate of the Conjugative and Hyperconjugative Stabilization in Diynes, Dienes, and Related Compounds *Angew. Chem. Int. Ed.* 2005, 44, 3617-3620.

221. Weinhold, F.; Landis, C. R., Valency and Bonding: A Natural Bond Orbital Donor-Acceptor Perspective. Cambridge University Press: 2005.

222. Jacobsen, H.; Ziegler, T., Nonclassical Double Bonds in Ethylene Analogues: Influence of Pauli Repulsion on Trans Bending and π-Bond Strength. A Density Functional Study. *J. Am. Chem. Soc.* 1994, 116, 3667-3679.

223. Sk, M. A.; Ng, M.-F.; Yang, S.-W.; Lim, K. H., Water induced electrical hysteresis in germanium nanowires: a theoretical study. *Phys. Chem. Chem. Phys.* 2011, 13, 11663–11670.

224. Wang, D.; Chang, Y.-L.; Liu, Z.; Dai, H., Oxidation Resistant Germanium Nanowires: Bulk Synthesis, Long Chain Alkanethiol Functionalization, and Langmuir-Blodgett Assembly. *J. Am. Chem. Soc.* 2005, 127, 11871-11875.

225. Adhikari, H.; McIntyre, P. C.; Sun, S. Y.; Pianetta, P.; Chidsey, C. E. D., Photoemission studies of passivation of germanium nanowires. *Appl. Phys. Lett.* 2005, 87, 263109.

226. Mingwei, J.; Ming, N.; Wei, S.; Jing, L.; Zhengxiang, G.; Lin, L.; Wai, N. M.; Dapeng, Y.; Hengqiang, Y.; Lu, W., Anisotropic and Passivation-Dependent Quantum Confinement Effects in Germanium Nanowires: A Comparison with Silicon Nanowires. *J. Phys. Chem. B* 2006, 110, 18332-18337.

227. Bescond, M.; Cavassilas, N.; Nehari, K.; Lannoo, M., Tight-binding calculations of Ge-nanowire bandstructures. *J. Comput. Electron.* 2007, 6, 341–344.

228. Arantes, J. T.; Fazzio, A., Theoretical investigations of Ge nanowires grown along the [110] and [111] directions. *Nanotechnology* 2007, 18, 295706.

229. Kholod, A. N.; Shaposhnikov, V. L.; Sobolev, N.; Borisenko, V. E.; D'Avitaya, F. A.; Ossicini, S., Orientation effects in the electronic and optical properties of germanium quantum wires. *Phys. Rev. B* 2004, 70, 035317.

230. Beckman, S. P.; Han, J.; Chelikowsky, J. R., Quantum confinement effects in Ge [110] nanowires. *Phys. Rev. B* 2006, 74, 165314.

231. Medaboina, D.; Gade, V.; Patil, S. K. R.; Khare, S. V., Effect of structure, surface passivation, and doping on the electronic properties of Ge nanowires: A first-principles study. *Phys. Rev. B* 2007, 76, 205327.

232. Harris, C.; O'Reilly, E. P., Nature of the band gap of silicon and germanium nanowires. *Physica E* 2006, 32, 341–345.

233. Nolan, M.; O'Callaghan, S.; Fagas, G.; Greer, J. C., Silicon Nanowire Band Gap Modification. *Nano Lett.* 2007, 7, 34-38.

234. Ng, M.-F.; Sim, L. Y.; Da, H.; Jin, H.; Lim, K. H.; Yang, S.-W., Modulation of the work function of silicon nanowire by chemical surface passivation: a DFT study. *Theor. Chem. Acc.* 2010, 127, 689–695.

235. Qadri, S. B.; Skelton, E. F.; Webb, A. W., High pressure studies of Ge using synchrotron radiation. *J. Appl. Phys.* 1983, 54, 3609-3611.

236. Aradi, B.; Ramos, L. E.; Deák, P.; Köhler, T.; Bechstedt, F.; Zhang, R. Q.; Frauenheim, T., Theoretical study of the chemical gap tuning in silicon nanowires. *Phys. Rev. B* 2007, 76,, 035305.

237. Hanrath, T.; Korgel, B. A., *J. Phys. Chem. B* 2005, 109, 5518-5524.

238. Kazakova, O.; Kulkarni, J. S.; Holmes, J. D.; Demokritov, S. O., Room-temperature ferromagnetism in $Ge_{1-x}Mn_x$ nanowires. *Phys. Rev. B* 2005, 72, 094415.

239. Pang, Q.; Zhang, Y.; Zhang, J.-M.; Xu, K.-W., Adsorption of Ge nanowire with 3d transition metals: A density-functional theory study. *Mater. Chem. Phys.* 2010, 124, 1113–1120.

240. Xu, Z.; Yan, Q.-B.; Zheng, Q.-R.; Su, G., Half-metallic silicon nanowires: Multiple surface dangling bonds and nonmagnetic doping. *Phys. Rev. B* 2009, 80, 081306.

241. Park, J.-S.; Ryu, B.; Moon, C.-Y.; Chang, K. J., Defects Responsible for the Hole Gas in Ge/Si Core-Shell Nanowires. *Nano Lett.* 2010, 10, 116-121.

242. Peelaers, H.; Partoens, B.; Peeters, F. M., Properties of B and P doped Ge nanowires. *Appl. Phys. Lett.* 2007, 90, 263103.

243. Dai, Z.; Yan, L.; Sk, M. A.; Feng, J.; Mariathomas, P. R. D.; Chen, Y.; Li, C. M.; Zhang, Q.; Li, L.-J.; Lim, K. H.; Chan-Park, M. B., Selective Small-Diameter Metallic Single-Walled Carbon Nanotube Removal by Mere Standing with Anthraquinone and Application to a Field-Effect Transistor. *J. Phys. Chem. C* 2010, 114, 21035–21041.

244. Woods, L. M.; Badescu, S. C.; Reinecke, T. L., Adsorption of simple benzene derivatives on carbon nanotubes, *Phys. Rev. B* 2007, 75, 155415.

245. Sangermano, M. a. V. C. J., *Visible and Long-Wavelength Cationic Photopolymerization, in Photoinitiated Polymerization*. American Chemical Society: Washington, DC., p 242.

246. Chen, Z.; Du, X.; Du, M.-H.; Rancken, C. D.; Cheng, H.-P.; Rinzler, A. G., Bulk Separative Enrichment in Metallic or Semiconducting Single-Walled Carbon Nanotubes. *Nano Lett.* 2003, 3, 1245-1249.

Appendix A

Supplementary Materials for Theoretical Studies on Germaallenes

A-1 The optimized Cartesian coordinates and total energies of the minima and cyclic isomers of germaallenes 3-10.

a. At the level of B3LYP/6-311+G(d,p).

1) $GeH_2=C=CH_2$, **3**

Stable minimum, *E*=-2155.505018 hartree, (including the zero-point-correction energy)

C	-0.126673	-1.057892	0.000000
C	0.169094	-2.330817	0.000000
Ge	0.000000	0.727014	0.000000
H	-0.427083	1.427329	1.289316
H	-0.427083	1.427329	-1.289316
H	-0.600466	-3.102613	0.000000
H	1.200105	-2.684245	0.000000

2) $CH_2=Ge=CH_2$, **4**

Stable minimum, *E*=-2155.485953 hartree, (including ZPE)

Ge	0.000000	0.000000	0.019846
C	0.000000	1.760323	-0.041752
C	0.000000	-1.760323	-0.041752
H	-0.632712	2.326327	0.626998
H	0.688143	2.279529	-0.694014
H	-0.688143	-2.279529	-0.694014
H	0.632712	-2.326327	0.626998

3) CH_2=Ge=CH_2, **5**

Cyclic isomer, *E*= -2155.542202 hartree, (including ZPE)

Ge	0.000000	0.000000	0.655619
C	0.000000	0.746116	-1.234607
C	0.000000	-0.746116	-1.234607
H	0.903558	1.266793	-1.541134
H	-0.903558	1.266793	-1.541134
H	0.903558	-1.266793	-1.541134
H	-0.903558	-1.266793	-1.541134

4) GeH_2=Ge=CH_2, **6**

Stable minimum, *E*= -4194.429881 hartree, (including ZPE)

Ge	0.000000	0.945818	0.000000
Ge	0.260734	-1.420000	0.000000
C	-1.241808	2.226918	0.000000
H	1.189400	-1.727134	1.217166
H	1.189400	-1.727134	-1.217166
H	-0.971476	3.277149	0.000000
H	-2.299948	1.989422	0.000000

5) GeH_2=Ge=CH_2, **7**

Cyclic isomer, *E*= -4194.447155 hartree, (including ZPE)

Ge	0.380486	-1.264033	0.000000
Ge	0.000000	1.196773	0.000000
C	-1.381215	-0.206444	0.000000
H	0.044608	2.036454	1.281851
H	0.044608	2.036454	-1.281851
H	-1.988745	-0.340950	0.895421
H	-1.988745	-0.340950	-0.895421

6) GeH_2=C=GeH_2, **8**

Stable minimum, *E*= -4194.380194 hartree, (including ZPE)

C	0.000000	0.000000	0.000000
Ge	0.000000	0.000000	1.754114
Ge	0.000000	0.000000	-1.754114
H	0.000000	1.285806	2.580128
H	0.000000	-1.285806	2.580128
H	1.285806	0.000000	-2.580128
H	-1.285806	0.000000	-2.580128

7) GeH_2=Ge=GeH_2, **9**

Cyclic isomer, *E*= -6233.380018 hartree, (including ZPE)

Ge	0.008355	1.341645	0.000000
Ge	0.008355	-0.587580	1.424236
Ge	0.008355	-0.587580	-1.424236
H	-1.019684	-0.662441	2.582362
H	0.618661	-2.001313	1.279096
H	-1.019684	-0.662441	-2.582362
H	0.618661	-2.001313	-1.279096

8) GeH_2=Ge=GeH_2, **10**

Cyclic isomer, *E*= -6233.370846 hartree, (including ZPE)

Ge	0.000000	0.000000	1.572341
Ge	0.000000	1.201935	-0.714947
Ge	0.000000	-1.201935	-0.714947
H	1.274226	1.947794	-1.139576
H	-1.274226	1.947794	-1.139576
H	1.274226	-1.947794	-1.139576
H	-1.274226	-1.947794	-1.139576

b. At the level of MP2/6-311+G(d,p).

1) $GeH_2=C=CH_2$, **3**

Stable minimum, *E*= -2153.624067 hartree, (including ZPE)

C	-0.111676	-1.051625	0.000000
C	0.123677	-2.353984	0.000000
Ge	0.000000	0.728566	0.000000
H	-0.261389	1.476578	1.297209
H	-0.261389	1.476578	-1.297209
H	-0.688200	-3.081899	0.000000
H	1.138971	-2.751707	0.000000

2) $CH_2=Ge=CH_2$, **4**

Stable minimum, *E*=-2153.608129 hartree, (including ZPE)

Ge	0.000000	0.000000	0.069871
C	0.000000	1.766072	-0.149080
C	0.000000	-1.766072	-0.149080
H	-0.552569	2.385678	0.548091
H	0.764502	2.219167	-0.771551
H	-0.764502	-2.219167	-0.771551
H	0.552569	-2.385678	0.548091

3) $CH_2=Ge=CH_2$, **5**

Cyclic isomer, *E*= -2153.663627 hartree, (including ZPE)

Ge	0.000000	0.000000	0.652216
C	0.000000	0.749232	-1.227290
C	0.000000	-0.749232	-1.227290
H	0.908049	1.264217	-1.535861
H	-0.908049	1.264217	-1.535861
H	0.908049	-1.264217	-1.535861
H	-0.908049	-1.264217	-1.535861

4) GeH_2=Ge=CH_2, **6**

Stable minimum, *E*= -4191.045634 hartree, (including ZPE)

Ge	0.000000	0.940024	0.000000
Ge	0.279547	-1.397660	0.000000
C	-1.302597	2.179453	0.000000
H	1.142976	-1.781302	1.227293
H	1.142976	-1.781302	-1.227293
H	-1.065509	3.240293	0.000000
H	-2.350352	1.889969	0.000000

5) GeH_2=Ge=CH_2, **7**

Cyclic isomer, *E*= -4191.1073432 hartree, (without ZPE correction)

Ge	0.376466	-1.268110	0.000000
Ge	0.000000	1.200737	0.000000
C	-1.373624	-0.202037	0.000000
H	0.077989	2.021258	1.286002
H	0.077989	2.021258	-1.286002
H	-1.980576	-0.337172	0.898643
H	-1.980576	-0.337172	-0.898643

6) GeH_2=C=GeH_2, **8**

Stable minimum, *E*= -4191.011148 hartree, (including ZPE)

C	0.000000	0.000000	0.000000
Ge	0.000000	0.000000	1.771500
Ge	0.000000	0.000000	-1.771500
H	0.000000	1.285132	2.593440
H	0.000000	-1.285132	2.593440
H	1.285132	0.000000	-2.593440
H	-1.285132	0.000000	-2.593440

7) GeH_2=Ge=GeH_2, **9**

Cyclic isomer, *E*= -6228.5310569 hartree, (without ZPE correction)

Ge	0.006454	1.351978	0.000000
Ge	0.006454	-0.593316	1.410231
Ge	0.006454	-0.593316	-1.410231
H	-0.939818	-0.649727	2.628560
H	0.630043	-1.995821	1.257311
H	-0.939818	-0.649727	-2.628560
H	0.630043	-1.995821	-1.257311

8) GeH_2=Ge=GeH_2, **10**

Cyclic isomer, *E*= -6228.5174029 hartree, (without ZPE correction)

Ge	0.000000	0.000000	1.577620
Ge	0.000000	1.202960	-0.719163
Ge	0.000000	-1.202960	-0.719163
H	1.280023	1.942311	-1.114344
H	-1.280023	1.942311	-1.114344
H	1.280023	-1.942311	-1.114344
H	-1.280023	-1.942311	-1.114344

c. At the level of CCSD/6-311+G(d,p).

1) GeH_2=C=CH_2, **3**

Stable minimum, *E*= -2153.7036712 hartree, (including ZPE)

C	-0.135952	-1.061639	0.000000
C	0 .161150	-2.350303	0.000000
Ge	0.000000	0.730402	0.000000
H	-0.365250	1.457089	1.292337
H	-0.365250	1.457089	-1.292337
H	-0.615179	-3.116296	0.000000
H	1.194488	-2.699076	0.000000

2) CH_2=Ge=CH_2, **4**

Stable minimum, *E*= -2153.6869145 hartree, (including ZPE)

Ge	0.000000	0.000000	0.116241
C	0.000000	1.753006	-0.240254
C	0.000000	-1.753006	-0.240254
H	-0.502271	2.428193	0.445317
H	0.790310	2.161834	-0.863650
H	-0.790310	-2.161834	-0.863650
H	0.502271	-2.428193	0.445317

3) CH_2=Ge=CH_2, **5**

Cyclic isomer, *E*= -2153.7495811 hartree, (including ZPE)

Ge	0.000000	0.000000	0.653658
C	0.000000	0.751551	-1.227806
C	0.000000	-0.751551	-1.227806
H	0.907501	1.263339	-1.545845
H	-0.907501	1.263339	-1.545845
H	0.907501	-1.263339	-1.545845
H	-0.907501	-1.263339	-1.545845

4) GeH_2=Ge=CH_2, **6**

Stable minimum, *E*= -4191.1260807 hartree, (including ZPE)

Ge	0.000000	0.963278	0.000000
Ge	0.297241	-1.404482	0.000000
C	-1.373753	2.122496	0.000000
H	1.173051	-1.796845	1.222804
H	1.173051	-1.796845	-1.222804
H	-1.209715	3.197205	0.000000
H	-2.405564	1.780042	0.000000

5) GeH_2=Ge=CH_2, **7**

Cyclic isomer, *E*= -4191.149121 hartree, (including ZPE)

Ge	0.377162	-1.273022	0.000000
Ge	0.000000	1.204403	0.000000
C	-1.375379	-0.201581	0.000000
H	0.075190	2.035466	1.285181
H	0.075190	2.035466	-1.285181
H	-1.983650	-0.332817	0.898684
H	-1.983650	-0.332817	-0.898684

6) GeH_2=C=GeH_2, **8**

Stable minimum, *E*= -4191.0787926 hartree, (including ZPE)

C	0.000000	0.000000	0.000000
Ge	0.000000	0.000000	1.768560
Ge	0.000000	0.000000	-1.768560
H	0.000000	1.288801	2.590188
H	0.000000	-1.288801	2.590188
H	1.288801	0.000000	-2.590188
H	-1.288801	0.000000	-2.590188

7) GeH_2=Ge=GeH_2, **9**

Cyclic isomer, *E*= -6228.5736828 hartree, (including ZPE)

Ge	0.006252	1.362015	0.000000
Ge	0.006252	-0.597711	1.402685
Ge	0.006252	-0.597711	-1.402685
H	-1.007277	-0.697070	2.565915
H	0.707163	-1.968434	1.286442
H	-1.007277	-0.697070	-2.565915
H	0.707163	-1.968434	-1.286442

8) GeH_2=Ge=GeH_2, **10**

Cyclic isomer, *E*= -6228.5681516 hartree, (including ZPE)

Ge	0.000000	0.000000	1.581789
Ge	0.000000	1.208394	-0.720355
Ge	0.000000	-1.208394	-0.720355
H	1.279433	1.951671	-1.128627
H	-1.279433	1.951671	-1.128627
H	1.279433	-1.951671	-1.128627
H	-1.279433	-1.951671	-1.128627

A-2 TS of germaallenes (3-10) at the B3LYP/6-311+G(d,p) level and the total energies (including the zero-point-correction energy)

1) CH_2=Ge=CH_2, *TS*

E= -2155.463315 hartree, (including ZPE)

Ge	0.003941	-0.481832	0.008790
C	1.364096	0.877675	0.014500
C	-1.369936	0.849868	-0.021208
H	2.409425	0.629052	-0.174009
H	1.149316	1.933941	-0.148260
H	-1.258159	1.835690	0.432118
H	-2.391667	0.654695	-0.350892

2) GeH_2=Ge=CH_2, *TS*

E= -4194.425132 hartree, (including ZPE)

Ge	-1.030990	-0.458944	0.003121
Ge	1.355197	0.107148	-0.040205
C	-1.743811	1.247870	0.010873
H	2.288142	-1.060136	0.412601
H	1.884963	1.307973	0.808153
H	-2.704655	1.441863	0.486433
H	-1.380212	2.080574	-0.585758

3) GeH_2=Ge=GeH_2, *TS*

E= -6233.370986 hartree, (including ZPE)

Ge	0.739993	-1.190124	-0.007321
Ge	-1.558777	-0.039742	0.008855
Ge	0.673949	1.226395	-0.008253
H	1.087162	-2.075643	-1.214418
H	1.329088	-1.743794	1.298709
H	1.012839	2.146984	-1.190835
H	1.205633	1.783524	1.321547

A-3 Full reference for Gaussian 03 program: Gaussian 03, Revision B.05, M. J. Frisch, G. W. Trucks, H. B. Schlegel, G. E. Scuseria, M. A. Robb, J. R. Cheeseman, J. A. Montgomery, Jr., T. Vreven, K. N. Kudin, J. C. Burant, J. M. Millam, S. S. Iyengar, J. Tomasi, V. Barone, B. Mennucci, M. Cossi, G. Scalmani, N. Rega, G. A. Petersson, H. Nakatsuji, M. Hada, M. Ehara, K. Toyota, R. Fukuda, J. Hasegawa, M. Ishida, T. Nakajima, Y. Honda, O. Kitao, H. Nakai, M. Klene, X. Li, J. E. Knox, H. P. Hratchian, J. B. Cross, C. Adamo, J. Jaramillo, R. Gomperts, R. E. Stratmann, O. Yazyev, A. J. Austin, R. Cammi, C. Pomelli, J. W. Ochterski, P. Y. Ayala, K. Morokuma, G. A. Voth, P. Salvador, J. J. Dannenberg, V. G. Zakrzewski, S. Dapprich, A. D. Daniels, M. C. Strain, O. Farkas, D. K. Malick, A. D. Rabuck, K.

Raghavachari, J. B. Foresman, J. V. Ortiz, Q. Cui, A. G. Baboul, S. Clifford, J. Cioslowski, B. B. Stefanov, G. Liu, A. Liashenko, P. Piskorz, I. Komaromi, R. L. Martin, D. J. Fox, T. Keith, M. A. Al-Laham, C. Y. Peng, A. Nanayakkara, M. Challacombe, P. M. W. Gill, B. Johnson, W. Chen, M. W. Wong, C. Gonzalez, and J. A. Pople, Gaussian, Inc., Pittsburgh PA, 2003.

A-4 NPA analysis

$\pi_{Ge=C}$ bond of 1-germaallene **3**:

$$\pi_{Ge=C} = 0.687(s^{0.08}p)_{Ge} + 0.727(s^{0.02}p)_{C} \quad (1)$$

$\pi_{C=Ge}$ bond of 2-germaallene **4**:

$$\pi_{C=Ge} = 0.834(s^{0.01}p)_{C} + 0.552(s^{0.01}p)_{Ge} \quad (2)$$

$\pi_{Ge1=Ge2}$ bond of 1,2-digermaallene **6**:

$$\pi_{Ge1=Ge2} = 0.641(s^{0.22}p)_{Ge1} + 0.768(s^{0.21}p)_{Ge2} \quad (3)$$

σ_{Ge-C} and $\pi_{Ge=C}$ bonds of 1,3-digermaallene **8**:

$$\sigma_{Ge-C} = 0.559(sp^{1.58})_{Ge} + 0.829(sp)_{C} \quad (4)$$

$$\pi_{Ge=C} = 0.582\ p_{Ge} + 0.813\ p_{C} \quad (5)$$

$\sigma_{Ge1-Ge2}$ bond of trigermaallene **9**:

$$\sigma_{Ge1-Ge2} = 0.594\ (s^{0.06}p)_{Ge1} + 0.805\ (sp^{1.62})_{Ge2} \quad (6)$$

A-5 Tables

Table S1. Calculated geometric parameters at the B3LYP, MP2 and CCSD level with a variety of basis sets for 1-germaallene **3**, 2-germaallene **4** and its cyclic isomer **5**[a, b].

$H_2Ge=C_1=C_2H_2$	Methods	$r(GeC_1)$	$r(C_1C_2)$	$r(GeC_2)$	$r(H_1H_3)$	$r(H_2H_4)$	$\alpha(GeC_1C_2)$[c]	$d(H_1GeC_2H_3)$	$d(H_1GeC_2H_4)$	$\Sigma\theta$[d]
	B3LYP/6-31G(d)	1.781	1.308	3.064	4.684	4.653	165.4	72.8	-107.2	347.1
	B3LYP/6-31G(d,p)	1.781	1.307	3.066	4.674	4.649	166.3	73.5	-106.5	348.2
	B3LYP/6-311G(d,p)	1.789	1.306	3.061	4.711	4.606	162.9	73.2	-106.8	346.8
Minimum	B3LYP/6-311+G(d,p)	1.789	1.307	3.063	4.713	4.606	162.9	73.3	-106.7	346.9
(3, *Cs*)	B3LYP/6-311+G(2df,p)	1.787	1.302	3.056	4.708	4.601	162.9	73.4	-106.6	347.2
	B3LYP/LanL2dz	1.795	1.327	3.098	4.736	4.671	165.7	73.3	-106.7	347.8
	MP2/6-311+G(d,p)	1.784	1.323	3.085	4.759	4.639	166.2	79.9	-100.1	354.6
	CCSD/6-311+G(d,p)	1.797	1.322	3.085	4.759	4.623	162.7	75.8	-104.2	349.9
$H_2C_1=Ge=C_2H_2$	Methods	$r(C_1Ge)$	$r(GeC_2)$	$r(C_1C_2)$	$r(H_1H_3)$	$r(H_2H_4)$	$\alpha(C_1GeC_2)$[c]	$d(H_1C_1C_2H_3)$	$d(H_1C_1C_2H_4)$	$\Sigma\theta$[d]
	B3LYP/6-31G(d)	1.778	1.778	3.471	4.751	4.751	155.0	91.8	-72.5	355.2
	B3LYP/6-31G(d,p)	1.774	1.774	3.476	4.749	4.749	156.8	91.5	-73.5	355.7
	B3LYP/6-311G(d,p)	1.760	1.760	3.518	4.788	4.788	176.0	90.1	-86.8	359.8
Minimum	B3LYP/6-311+G(d,p)	1.761	1.761	3.521	4.792	4.792	176.0	90.1	-86.8	359.8
(4, C_2)	B3LYP/6-311+G(2df,p)	1.759	1.759	3.515	4.787	4.787	176.0	90.1	-86.8	359.8
	B3LYP/LanL2dz	1.775	1.775	3.548	4.837	4.837	176.0	90.0	-88.4	359.9
	MP2/6-311+G(d,p)	1.780	1.780	3.532	4.795	4.795	165.9	90.8	-76.8	357.5
	CCSD/6-311+G(d,p)	1.789	1.789	3.506	4.782	4.782	157.0	92.0	-72.5	355.5
	B3LYP/6-31G(d)	2.014	2.014	1.495	2.538	2.538	43.6	0.00	-142.1	344.8
	B3LYP/6-31G(d,p)	2.013	2.013	1.495	2.539	2.539	43.6	0.0	-142.5	344.6
	B3LYP/6-311G(d,p)	2.032	2.032	1.491	2.531	2.531	43.1	0.0	-142.5	344.5
Cyclic isomer	B3LYP/6-311+G(d,p)	2.032	2.032	1.492	2.534	2.534	43.1	0.0	-142.5	344.4
(5, C_{2v})	B3LYP/6-311+G(2df,p)	2.025	2.025	1.490	2.530	2.530	43.2	0.0	-142.3	344.6
	B3LYP/LanL2dz	2.050	2.05	1.516	2.549	2.549	43.4	0.0	-140.2	345.8
	MP2/6-311+G(d,p)	2.023	2.023	1.498	2.528	2.528	43.5	0.0	-142.5	345.1
	CCSD/6-311+G(d,p)	2.026	2.026	1.503	2.527	2.527	43.5	0.0	-141.4	345.7

[a] For notations see Figure 4.1. Bond distances (*r*) are in Å, bond angles (*a*) and dihedral angles (*d*) are in degrees. The C-H and Ge-H bond length values are omitted. The values of C-H bond length are from 1.080Å to 1.093Å and the values of Ge-H bond length are from 1.520Å to 1.538Å. [b] The B3LYP/6-311+G(d,p) Ge=Ge, Ge=C, C=C bond lengths of digermene, germene and ethene molecules are 2.305, 1.779 and 1.329 Å, respectively; and the B3LYP/6-311+G(d,p) Ge-Ge, Ge-C, C-C bond lengths of digermane, germane and ethane molecules are 2.444, 1.969 and 1.531 Å, respectively. [c] α is the bond angle of 1-germaallene **3** and 2-germaallene **4** bend at their central atom, for definition see Figure 4.3. [d] The sum of bond angles

around the terminal Ge_1 or C_1 atoms, which measures the degree of pyramidalization at the terminal atom, for definition see Figure 4.3.

Table S2. Calculated geometric parameters at the B3LYP, MP2 and CCSD methods with a variety of basis sets for 1,2-digermaallene **6** and its cyclic isomer **7**, and 1,3-digermaallene **8**[a].

$H_2Ge_2=Ge_1=CH_2$	Methods	$r(Ge_2Ge_1)$	$r(Ge_1C)$	$r(Ge_2C)$	$r(H_1H_3)$	$r(H_2H_4)$	$\alpha(Ge_2Ge_1C)$[b]	$d(H_1Ge_2CH_3)$	$d(H_1Ge_2CH_4)$	$\Sigma\theta$[c]
Minimum (6, C_s)	B3LYP/6-31G(d)	2.325	1.773	3.993	5.409	5.298	153.8	54.9	-125.1	304.8
	B3LYP/6-31G(d,p)	2.320	1.771	3.893	5.419	5.288	153.2	55.8	-124.2	307.5
	B3LYP/6-311G(d,p)	2.380	1.783	3.946	5.580	5.247	142.4	58.5	-121.5	312.5
	B3LYP/6-311+G(d,p)	2.380	1.784	3.944	5.585	5.241	142.2	58.6	-121.4	312.6
	B3LYP/6-311+G(2df,p)	2.367	1.782	3.925	5.585	5.229	141.7	59.4	-120.6	314.5
	B3LYP/LanL2dz	2.427	1.795	3.958	5.691	5.273	138.8	60.0	-120.0	315.6
	MP2/6-311+G(d,p)	2.354	1.798	3.911	5.621	5.214	140.4	62.7	-117.3	321.2
	CCSD/6-311+G(d,p)	2.386	1.797	3.903	5.667	5.205	137.3	63.0	-117.0	321.2
Cyclic isomer (7, C_s)	B3LYP/6-31G(d)	2.459	2.038	1.952	3.148	3.148	50.4	-3.0	135.8	358.3
	B3LYP/6-31G(d,p)	2.457	2.035	1.954	3.138	3.138	50.5	-2.8	136.1	358.4
	B3LYP/6-311G(d,p)	2.491	2.055	1.969	3.150	3.150	50.2	-2.8	135.7	358.4
	B3LYP/6-311+G(d,p)	2.490	2.055	1.969	3.152	3.152	50.2	-2.8	135.8	358.4
	B3LYP/6-311+G(2df,p)	2.478	2.047	1.965	3.149	3.149	50.4	-2.9	135.9	358.4
	B3LYP/LanL2dz	2.557	2.069	1.975	3.165	3.165	49.2	-0.9	134.3	358.5
	MP2/6-311+G(d,p)	2.497	2.049	1.963	3.154	3.154	50.0	-1.3	137.4	357.8
	CCSD/6-311+G(d,p)	2.506	2.054	1.967	3.162	3.162	49.9	-1.4	136.8	357.9
$H_2Ge_1=C=Ge_2H_2$	Methods	$r(Ge_1C)$	$r(CGe_2)$	$r(Ge_1Ge_2)$	$r(H_1H_3)$	$r(H_2H_4)$	$\alpha(Ge_1CGe_2)$[b]	$d(H_1Ge_1Ge_2H_3)$	$d(H_1Ge_1Ge_2H_4)$	$\Sigma\theta$[c]
Minimum (8, D_{2d})	B3LYP/6-31G(d)	1.745	1.745	3.490	5.467	5.467	180.0	90.0	-90.0	360.0
	B3LYP/6-31G(d,p)	1.746	1.746	3.493	5.449	5.449	180.0	90.0	-90.0	360.0
	B3LYP/6-311G(d,p)	1.754	1.754	3.508	5.472	5.472	180.0	90.0	-90.0	360.0
	B3LYP/6-311+G(d,p)	1.754	1.754	3.508	5.471	5.471	180.0	90.0	-90.0	360.0
	B3LYP/6-311+G(2df,p)	1.751	1.751	3.502	5.468	5.468	180.0	90.0	-90.0	360.0
	B3LYP/LanL2dz	1.760	1.760	3.520	5.510	5.510	180.0	90.0	-90.0	360.0
	MP2/6-311+G(d,p)	1.772	1.772	3.543	5.496	5.496	180.0	90.0	-90.0	360.0
	CCSD/6-311+G(d,p)	1.769	1.769	3.537	5.492	5.492	180.0	90.0	-90.0	360.0

[a] For notations see Figure 4.1. Bond distances (r) are in Å, bond angles (a) and dihedral angles (d) are in degrees. The C-H and Ge-H bond length values are omitted. The values of C-H bond length are from 1.084Å to 1.095Å and the values of Ge-H length are from 1.526Å to 1.575Å. [b] α is the bond angle of 1,2-digermaallene **6** and its cyclic isomer **7** and 1,3-digermaallene **8** bend at their central atom, for definition see Figure 4.3. [c] The sum of bond angles around the terminal Ge_1 atom, for definition see Figure 4.3.

Table S3. Calculated geometric parameters at the B3LYP, MP2 and CCSD level with a variety of basis sets for trigermaallene **9** and its cyclic isomer **10**[a].

$H_2Ge_2=Ge_1=Ge_3H_2$	Methods	$r(Ge_2Ge_1)$	$r(Ge_1Ge_3)$	$r(Ge_2Ge_3)$	$r(H_1H_3)$	$r(H_2H_4)$	$\alpha(Ge_2Ge_1Ge_3)$[b]	$d(H_1Ge_2Ge_3H_3)$	$d(H_1Ge_2Ge_3H_4)$	$\Sigma\theta$[c]
Minimum (9, *Cs*)	B3LYP/6-31G(d)	2.365	2.365	2.761	5.116	2.547	71.4	0.0	-109.7	359.1
	B3LYP/6-31G(d,p)	2.367	2.367	2.745	4.977	2.559	70.9	0.0	-110.8	359.0
	B3LYP/6-311G(d,p)	2.398	2.398	2.848	5.165	2.560	72.9	0.0	-109.2	358.4
	B3LYP/6-311+G(d,p)	2.398	2.398	2.848	5.165	2.558	72.9	0.0	-109.2	358.4
	B3LYP/6-311+G(2df,p)	2.388	2.388	2.827	5.140	2.552	72.6	0.0	-109.5	358.5
	B3LYP/LanL2dz	2.462	2.462	3.074	5.693	2.654	77.3	0.0	-108.1	358.4
	MP2/6-311+G(d,p)	2.403	2.403	2.820	5.257	2.515	71.9	0.0	-110.6	359.2
	CCSD/6-311+G(d,p)	2.410	2.410	2.805	5.132	2.573	71.2	0.0	-111.5	359.3
Cyclic isomer (10, C_{2v})	B3LYP/6-31G(d)	2.549	2.549	2.363	3.869	3.869	55.2	0.0	-143.9	347.8
	B3LYP/6-31G(d,p)	2.545	2.545	2.362	3.839	3.839	55.3	0.0	-144.5	348.0
	B3LYP/6-311G(d,p)	2.584	2.584	2.404	3.894	3.894	55.4	0.0	-143.1	348.2
	B3LYP/6-311+G(d,p)	2.584	2.584	2.404	3.896	3.896	55.4	0.0	-143.1	348.2
	B3LYP/6-311+G(2df,p)	2.572	2.572	2.395	3.885	3.885	55.5	0.0	-143.2	348.2
	B3LYP/LanL2dz	2.666	2.666	2.447	3.929	3.929	54.6	0.0	-142.3	348.6
	MP2/6-311+G(d,p)	2.592	2.592	2.406	3.885	3.885	55.3	0.0	-145.7	347.4
	CCSD/6-311+G(d,p)	2.600	2.600	2.417	3.903	3.903	55.4	0.0	-144.6	347.8

[a] For notations see Figure 4.1. Bond distances (*r*) are in Å, bond angles (*a*) and dihedral angles (*d*) are in degrees. The Ge-H bond length values are omitted. The values of Ge-H bond length are from 1.535Å to 1.559Å. [b] α is the bond angle of trigermaallene at its central Ge_1 atom, for definition see Figure 4.3. [c] The sum of bond angles around the terminal Ge_2 (Ge_3) atom, for definition see Figure 4.3.

Appendix B

Supplementary Materials for Theoretical Studies on Germanium Nanowires

B-1 Water Induced Electrical Hysteresis in Germanium Nanowires

B-1-1 Tables

Table S1. The optimized average bond lengths[a] (R) of ⟨100⟩ OH-GeNWs with different OH coverage percentage on the NW surface.

P_{SC}[b]	R_{Ge-Ge} (Surface)	R_{Ge-Ge} (Core)	R_{Ge-H}	R_{Ge-O}	R_{O-H}
0.00	2.47	2.49	1.57-1.58		
4.17	2.46-2.49	2.49-2.51	1.57-1.58	1.87-1.88	0.94
8.33	2.46-2.48	2.49-2.50	1.57-1.58	1.87	0.95
16.67	2.46-2.49	2.49-2.50	1.57-1.58	1.86-1.88	0.94
33.33	2.47	2.49	1.57	1.86	0.95
66.67	2.51-2.52	2.55	1.58	1.86	0.95
83.33	2.49-2.58	2.50-2.55	1.58	1.82-1.88	0.95-0.96
100.00	2.46	2.52		1.83-1.89	0.95-0.96

[a] The R values at Å, [b] P_{SC} is the surface OH coverage percentage.

Table S2. The optimized average bond length (R[a]) of ⟨110⟩ OH-GeNWs with different OH coverage percentage on the NW surface.

P_{SC}[b]	R_{Ge-Ge} (Surface)	R_{Ge-Ge} (Core)	R_{Ge-H}	R_{Ge-O}	R_{O-H}
0.00	2.47-2.50	2.50-2.52	1.58		
5.67	2.47-2.50	2.50-2.51	1.57-1.58	1.86-1.87	0.94
11.11	2.47-2.51	2.50-2.52	1.57-1.58	1.86-1.87	0.94
22.22	2.46-2.53	2.50-2.54	1.57-1.58	1.86-1.90	0.94-0.95
33.33	2.46-2.52	2.49-2.53	1.57-1.58	1.85-1.88	0.94-0.95
66.67	2.44-2.57	2.49-2.54	1.57-1.59	1.85-1.90	0.94-0.95
77.78	2.44-2.57	2.49-2.54	1.57-1.59	1.84-1.89	0.94-0.95
100.00	2.50-2.63	2.50-2.52		1.83-1.92	0.94-0.97

[a] The R values at Å, [b] P_{SC} is the surface OH coverage percentage.

Table S3. Positional effect of OH group on the stability and band gap of ⟨100⟩ GeNW.

Systems	**RE (eV)**	**E_{gap} (eV)**
GeNW-1	0.00	2.02 *i*
GeNW-2	0.06	1.98 *d*
GeNW-3	0.14	2.01 *i*

Table S4. Positional effect of OH group on the stability and band gap of ⟨110⟩ GeNW.

Systems	**RE (eV)**	**E_{gap} (eV)**
GeNW-1	0.14	1.17 *d*
GeNW-2	0.14	1.16 *d*
GeNW-3	0.02	1.11 *d*
GeNW-4	0.00	1.13 *d*
GeNW-5	0.03	1.13 *d*
GeNW-6	0.03	1.13 *d*
GeNW-7	0.02	1.13 *d*
GeNW-8	0.14	1.17 *d*
GeNW-9	0.13	1.16 *d*

Table S5. Results of regression analysis of E_{form} with OH coverage percentage.

Systems	**Equations**	***n***	r^2	***p***
⟨100⟩ OH-GeNW	E_{form} = - 0.024(±0.000) P_{SC} + 0.203(±0.025)	8	0.998	<0.0001
⟨110⟩ OH-GeNW	E_{form} = - 0.018(±0.000) P_{SC} + 0.160 (±0.005)	8	0.999	<0.0001

Table S6. Effective mass of electrons in ⟨100⟩ and ⟨110⟩ OH-GeNWs.

⟨100⟩ OH-GeNW		⟨110⟩ OH-GeNW	
P_{SC}[a]	m^*_e	P_{SC}[a]	m^*_e
0.00	1.560	0.00	0.193
4.17	4.590	5.67	0.198
8.33	2.910	11.11	0.199
16.67	1.260	22.22	0.204
33.33	0.940	33.33	0.233
66.67	0.823	66.67	0.228
83.33	0.821	77.78	0.292
100.00	0.794	100.00	0.294

[a] P_{SC} is the surface OH coverage percentage.

B-1-2 Figure

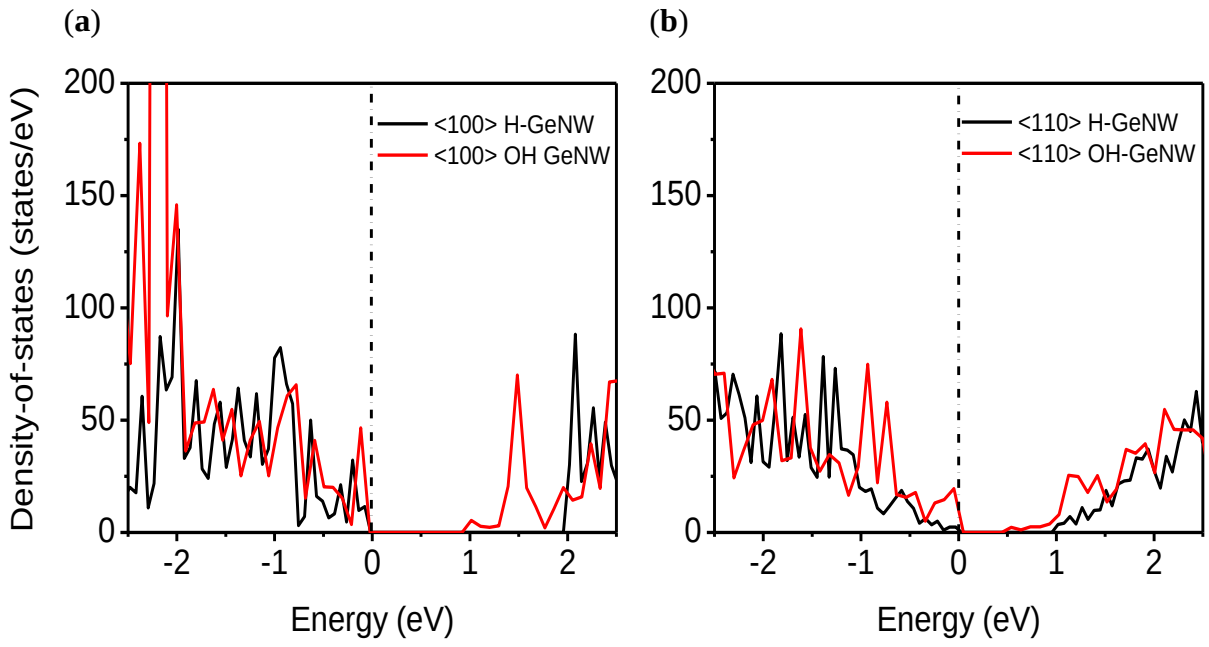

Figure S1. Density of state (DOS) of (a) ⟨100⟩ GeNW and OH-GeNW and (b) ⟨110⟩ GeNW and OH-GeNW, red line is for 100.0% OH-GeNW, black is for GeNW, dash-dot line is the Fermi level. The Fermi level is set to zero.

B-2 Stress Induced Half-Metallicity in Surface Defected Germanium Nanowires

B-2-1 Tables

Table S7. Calculated defect generation energies of SDB defects per SDB (E_{Gen}^{SDB}), and formation energy (E_{form}), net magnetic moments (in μ_B) per unit cell and band gap (E_{gap}) of surface defected GeNWs.

GeNW	E_{Gen}^{SDB} per SDB (eV)	E_{form} (eV/Ge atoms)	Net magnetic moment (μ_B)	E_{gap}	
				Spin-up	Spin-down
2h	0.72	0.23	1.96	1.47	0.81
2i	0.62	0.23	0.00	0.29	0.29
2j	0.70	0.23	0.00	0.13	0.13
2k	0.92	0.24	2.00	1.60	0.85
2l	0.92	0.24	2.00	1.58	0.91
2m	0.92	0.24	2.00	1.54	0.88
2n	0.76	0.23	0.00	0.68	0.68
2o	-0.04	0.18	0.00	2.01	
2p	0.91	0.24	2.00	1.64	0.91
2q	0.90	0.24	2.00	1.70	0.97
2r	0.91	0.24	2.00	1.60	0.88
4c	0.91	0.30	0.00	0.11	0.11
4d	0.92	0.30	3.95	1.64	0.68
4e	0.79	0.28	0.00	0.59	0.59
8a	0.56	0.33	0.00	0.00	0.00
8b	0.40	0.29	0.00	0.42	0.42

Table S8. Total energies of optimized surface defected GeNWs and their magnetic states.

GeNW	Total Energies (eV) [a]	States [b]
1a	-429.654281	FM [-429.654344] [c]
1b	-429.259966	FM [-429.260053]
1c	-429.284768	FM [-429.284742]
2a	-421.448723	wFM [-421.448702]
2b	-423.205380	AFM [-423.205351]
2c	-421.437060	wFM [-421.437048]
2d	-421.556915	AFM [-421.556840]
2e	-420.658462	FM [-420.658491]
2f	-424.495316	NM
2g	-420.670591	wFM [-420.670592]
2h	-421.451182	FM [-421.451221]
2i	-421.867790	AFM [-421.867788]
2j	-421.547371	AFM [-421.605684]
2k	-420.660695	FM [-420.660785]
2l	-420.666614	FM [-420.666601]
2m	-420.657327	FM [-420.657253]
2n	-421.288757	AFM [-421.288678]
2o	-424.497828	NM
2p	-420.713047	FM [-420.713073]
2q	-420.721885	FM [-420.721858]
2r	-420.703455	FM [-420.703466]
4a	-405.263527	wFM [-405.263504]
4b	-405.215841	wFM [-405.215876]

4c	-403.522028	AFM [-403.522042]
4d	-403.448965	FM [-403.449126]
4e	-404.723499	AFM [-404.723498]
8	-383.464713	NM
8a	-374.755651	AFM [-374.756788]
8b	-377.332074	AFM [-377.332003]

[a] The total energies of optimized surface defected GeNWs. [b] The FM, wFM, AFM and NM indicate the ferromagnetic, weak ferromagnetic, anti-ferromagnetic and non-magnetic respectively. [c] The value in the parentheses are the total energies of FM or AFM surface defected GeNWs.

B-2-2 Figures

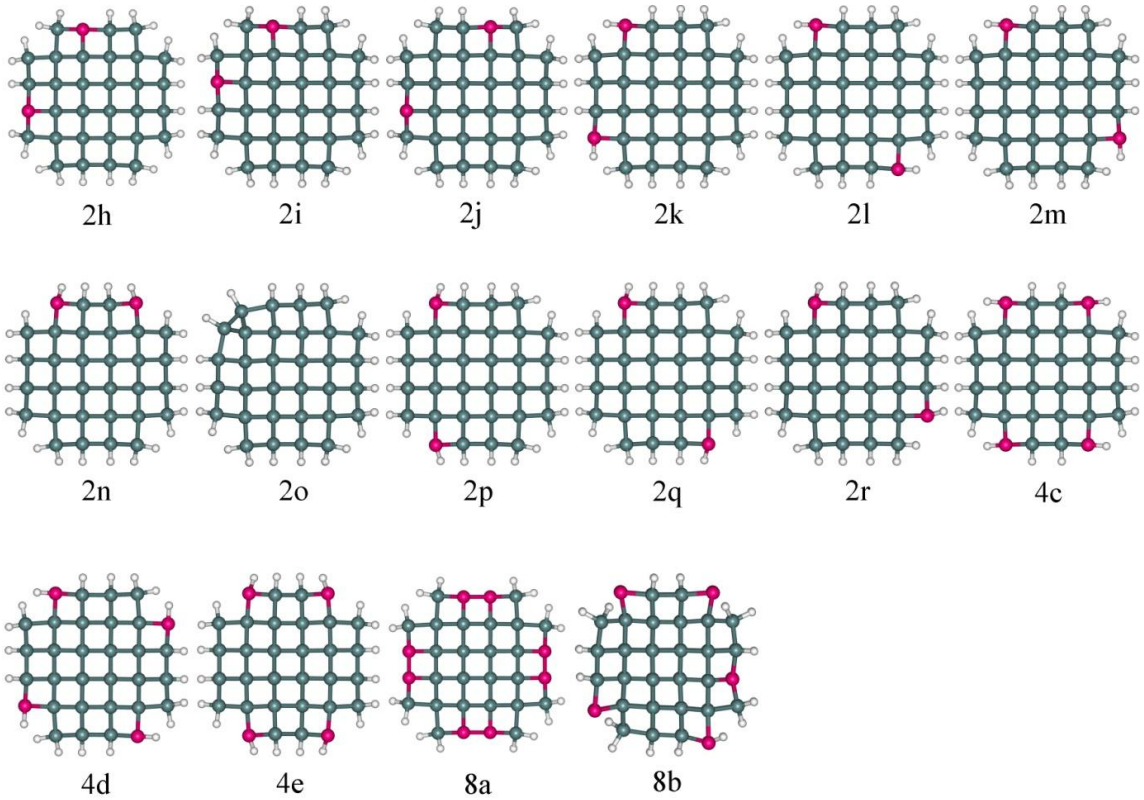

Figure S2. The optimized structures of surface defected GeNWs. Green sphere – Ge, pink sphere – Ge with SDB and white sphere – H.

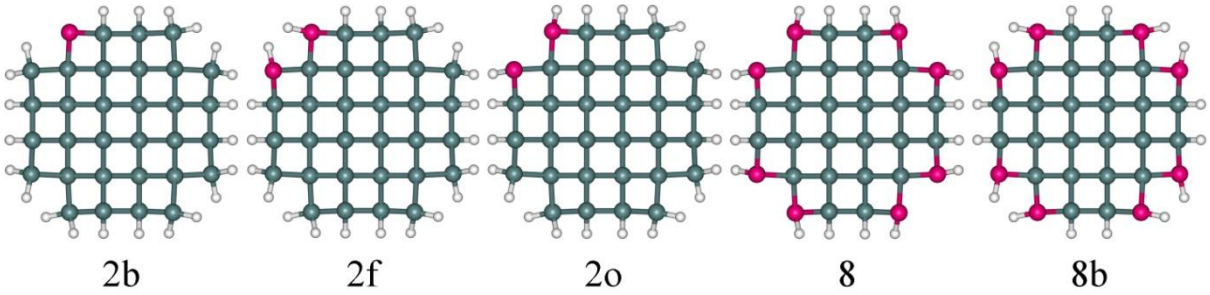

Figure S3. The initial structures of GeNWs undergo surface reconstruction.

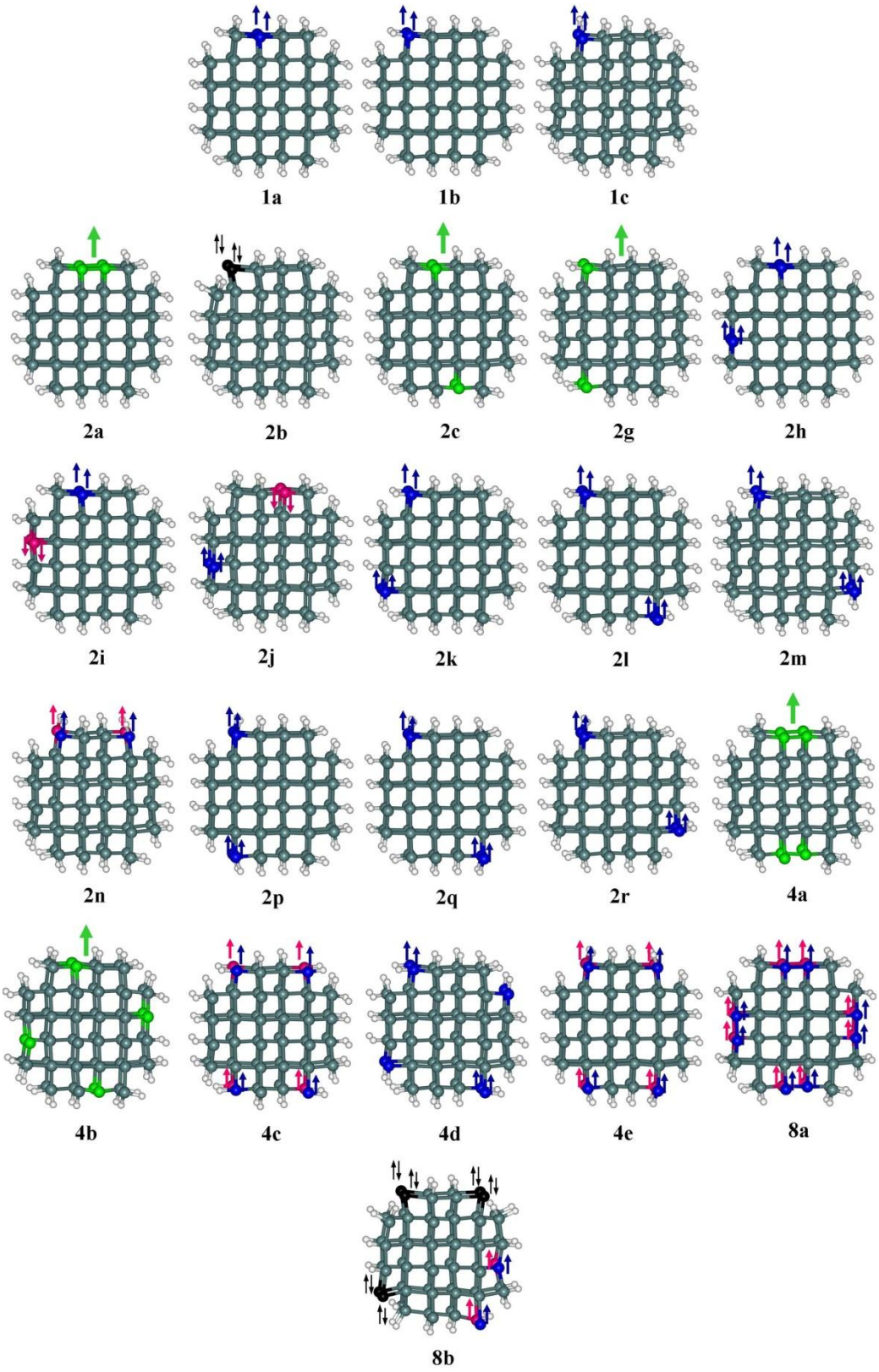

Figure S4. The electron configurations in surface defected GeNWs. The blue and pink spheres indicate the spin-up and spin-down, respectively. The black sphere indicates the singlet-state. The blue sphere indicates the weak ferromagnetic.

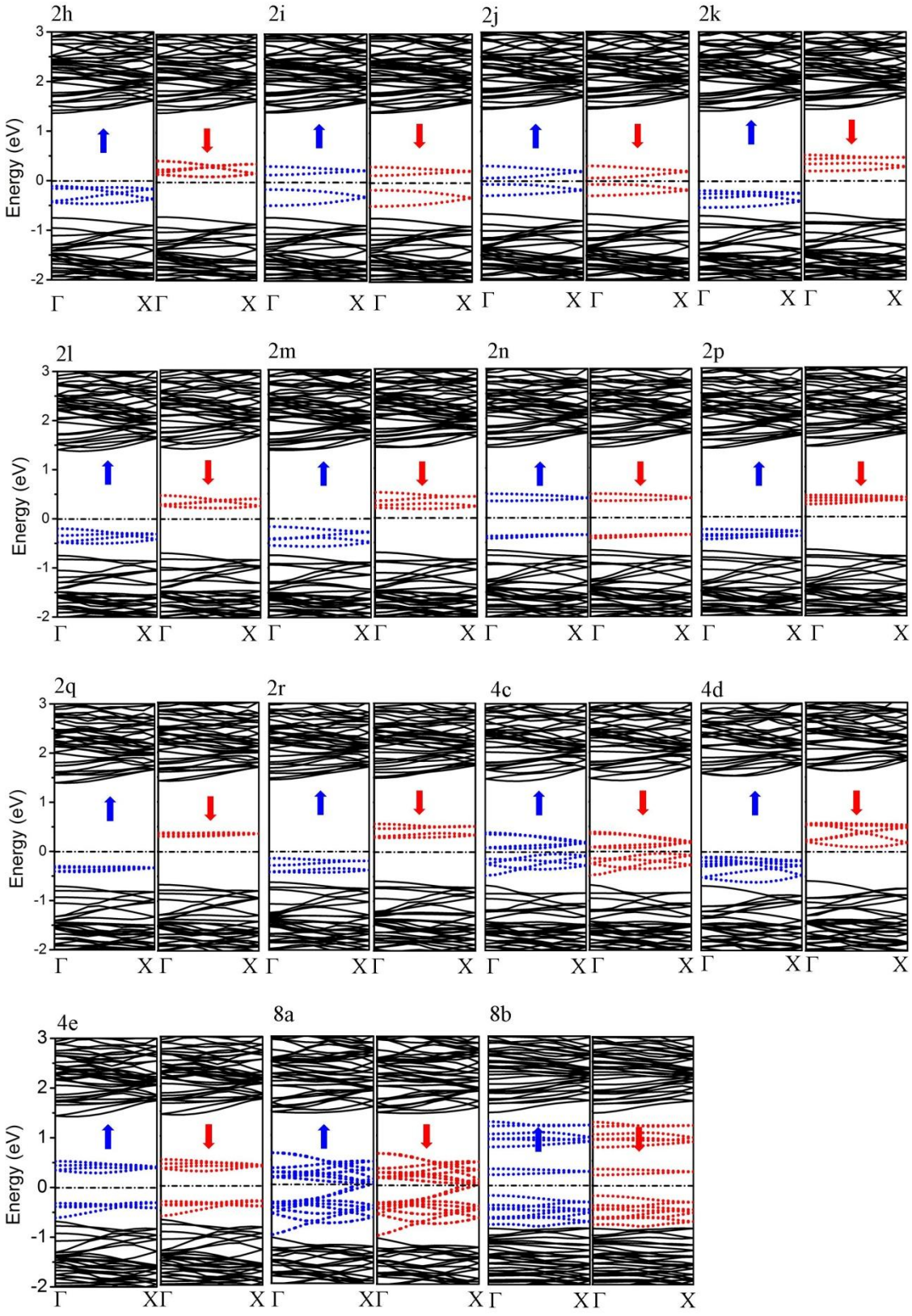

Figure S5. Band structures of surface defected GeNWs. The band structure of **2o** is same with **2f** and not shown here.

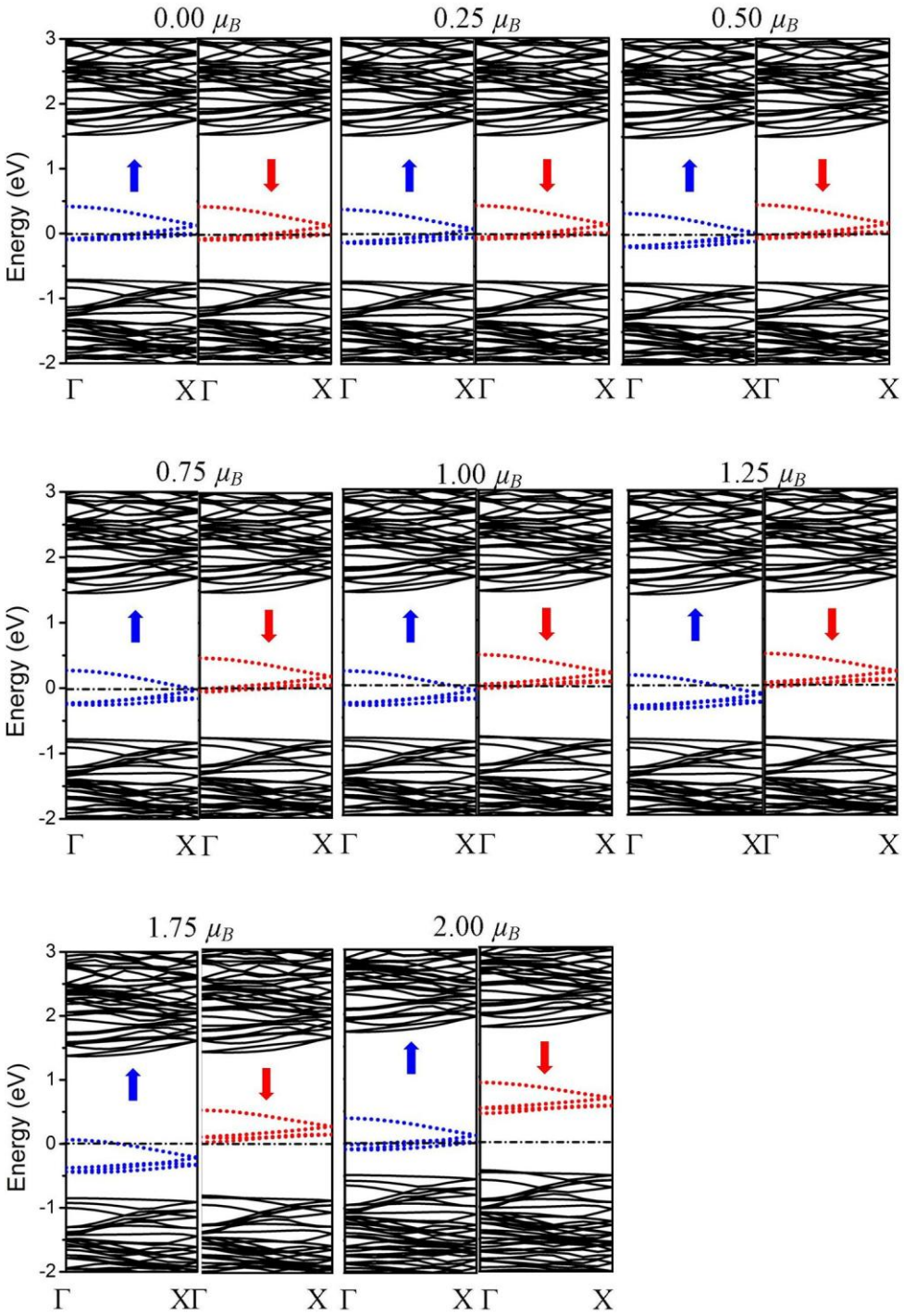

Figure S6. The band structures of **2c** with different magnetic moments. The net magnetic moments are shown on top.

List of Publications

Journal Publications

(1) **M. A. Sk**, M.-F Ng, S.-W Yang and K. H. Lim. Stress Induced Half-Metallicity in Surface Defected Germanium Nanowire. Physical Chemistry Chemical Physics **2012**, *14*, 1166-1174.

(2) **M. A. Sk**, M.-F Ng, S.-W Yang and K. H. Lim. Water Induced Electrical Hysteresis in Germanium Nanowire: A Theoretical Study. Physical Chemistry Chemical Physics **2011**, *13*, 11663–11670.

(3) D. V. Wellia, Q.-C. Xu, **M. A. Sk**, K. H. Lim, T. M. Lim, T. T. Y. Tan. Experimental and theoretical studies of Fe-doped TiO2 films prepared by peroxo sol-gel method, Applied Catalysis A: General, **2011**, *401*, 98-105.

(4) J. Feng, **M. A. Sk**, L. Y. Yan, C. M. Li, Z. Judeh, Y. Chen, L.-J Li, K. H. Lim and M. B. Chan-Park. Sorting of Single-Walled Carbon Nanotubes Based on Metallicity by Selective Precipitation with Polyvinylpyrrolidone. Journal of Physical Chemistry C **2011**, *115*, 5199-5206.

(5) Z. Dai, L. Yan, **M. A. Sk**, J. Feng, P. R. D. Mariathomas, Y. Chen, C. M. Li, Q. Zhang, L.-J Li, K. H. Lim and M. B. Chan-Park. Selective Small-Diameter Metallic Single-Walled Carbon Nanotubes Removal by Mere Standing with Anthraquinone and Application to Field-Effect Transistor, Journal of Physical Chemistry C **2010**, *114*, 21035-20141.

(6) Q.-C. Xu, D. V. Wellia, **M. A. Sk**, K. H. Lim, J. S. C. Loo, D. W. Liao, R. Amal and T. T. Y. Tan. Transparent Visible Light Activated C-N-F-Codoped TiO 2 Films for Self-Cleaning Applications, Journal of Photochemistry and Photobiology A: Chemistry, **2010**, *210*, 181-187.

(7) **M. A. Sk**, H.-W. Xi, and K. H. Lim. Structure, Bonding and Hyperconjugation of Germaallene: A Theoretical Study. Organometallics **2009**, *28*, 3678-3685.

Conference Proceedings

(1) **M. A. Sk** and K. H. Lim, Designing of Half-metallic Germanium Nanowires - A DFT Study, 18th Regional Symposium on Chemical Engineering, Ho Chi Minh City, Vietnam, Oct. 2011.

(2) **M. A. Sk**, M.-F Ng, S.-W Yang and K. H. Lim, Evaluations of Electronic and Magnetic Properties of Germanium Nanowires: Effects of Water Adsorption, Chemical Passivations and Surface Defects, Nanotechnology and Printed Electronics International Symposium 2011 (NanoPrint 2011), Singapore, Jul. 2011.

(3) **M. A. Sk**, M.-F Ng and K. H. Lim, Effect of Surface Defect on the Electronic Properties of Germanium Nanowires: A Possible Half-Metallic Property, 17th Regional Symposium on Chemical Engineering (RSCE2010) & The 20th Thailand Chemical Engineering and Applied Chemistry Conference (TIChE2010), Thailand, Bangkok, Nov 2010.

(4) **M. A. Sk**, M.-F Ng and K. H. Lim, The Effect of Surface Chemical Passivation on Electronic Properties of Germanium Nanowire, 13th Asia Pacific Confederation of Chemical Engineering Congress, Taipei, Taiwan, Oct. 2010.

(5) **M. A. Sk**, M.-F Ng and K. H. Lim, Growth Orientation Dependent Elastic Properties of Ge Nanowires: A DFT Study, International Symposium on Exploring the Frontiers of Chemical and Biomedical Engineering, NTU, Singapore, May 2010.

(6) **M. A. Sk**, H. Da, M.-F Ng and K. H. Lim, Structural and Electronic Properties of OH-Passivated Germanium Nanowires, 16th Regional Symposium on Chemical Engineering, Manila, Philippines, Dec. 2009.